ABSTRACT

TERAHERTZ RESPONSE OF MICROFLUIDIC-JETTED FABRICATED 3D FLEXIBLE METAMATERIALS

by
Yew Li Hor

Conventional materials exhibit some restrictions on their electromagnetic properties. Especially in terahertz region, for example, materials that exhibit magnetic response are far less common in nature than materials that exhibit electric response. However, materials can be designed, namely artificial man-made metamaterials that exhibit electromagnetic properties that are not found in natural materials by adjusting, for example, the dielectric, magnetic or structural parameters of the constituent elements.

This dissertation demonstrates the use of new fabrication techniques to construct metamaterials in THz range via a material deposition system. The metamaterials are fabricated by stacking alternative layers with conventional designs such as single ring-split ring resonators (SRR) and microstrips to form a 3D metamaterial structure. Conductive nano-particle Ag, Cu and semiconductor polymer fluids are used as structural mediums. The metamaterials are fabricated on polyimide substrate. Their flexible nature will be advantageous in future device innovations. In order to obtain electromagnetic resonance in the terahertz range, the dimensions of the single ring-SRR and microstrips are first approximated by analytical methods and then confirmed by numerical simulation. The fabricated metamaterials are then characterized in transmission mode using Time-domain THz Spectroscopy (THz-TDS) in the 0.1 to 2 THz range.

TERAHERTZ RESPONSE OF MICROFLUIDIC-JETTED FABRICATED 3D FLEXIBLE METAMATERIALS

by
Yew Li Hor

A Dissertation
Submitted to the Faculty of
New Jersey Institute of Technology and
Rutgers, The State University of New Jersey-Newark
in Partial Fulfillment of the Requirements for the Degree of
Doctor of Philosophy in Applied Physics

Federated Physics Department

January 2009

APPROVAL PAGE

TERAHERTZ RESPONSE OF MICROFLUIDIC-JETTED FABRICATED 3D FLEXIBLE METAMATERIALS

Yew Li Hor

12/9/08

Dr. John F. Federici, Dissertation Advisor — Date
Distinguished Professor of Applied Physics, NJIT

12/4/08

Dr. Robert B. Barat, Committee Member — Date
Professor of Chemical Engineering, NJIT

12/4/08

Dr. Dale E. Gary, Committee Member — Date
Professor of Applied Physics, NJIT

12/4/08

Dr. Andrei Sirenko, Committee Member — Date
Associate Professor of Applied Physics, NJIT

11/25/08

Dr. Francisco Miguel Vargas Luna, Committee Member — Date
Professor of Physics Institute, Universidad de Guanajuato

BIOGRAPHICAL SKETCH

Author: Yew Li Hor

Degree: Doctor of Philosophy

Undergraduate and Graduate Education:

- Doctor of Philosophy in Applied Physics,
  New Jersey Institute of Technology, Newark, NJ, 2009

- Master of Science in Physics,
  Western Illinois University, Macomb, IL, 2002

- Bachelor of Science in Microelectronics and Physics,
  Campbell University, Buies Creek, NC, 1999

Major: Applied Physics

Presentations and Publications:

Yew Li Hor, Hee C. Lim, John F. Federici;
"Terahertz response of microfluidic-jetted fabricated 3D multilayer metamaterials," manuscript preparation.

Yew Li Hor, Hee C. Lim, John F. Federici;
"Terahertz response of microfluidic-jetted fabricated 3D multilayer metamaterials," *33rd International Conference on Infrared and Millimeter Waves, 16th International Conference on Terahertz Electronics, (IRMMW-THz 2008), Caltech,* Pasadena, California, Sept 15, 2008.

Hee C. Lim, Yew Fong Hor, Yew Li. Hor, James L. Zunino III, John F. Federici;
"Poly (3, 4-ethylenedioxythiophene) - poly (4-styrenesulfonate) for humidity sensing using ink-jet printing technique on flexible polyimide substrate," *Sensors & Transducers Journal*, Under review.

Alexander M Sinyukov, Zhiwei Liu, Yew Li Hor, Ke Su, Robert B Barat, Dale E. Gary, Zoi-Heleni Michalopoulou, Ivan Zorych, John F Federici1, David Zimdars;
"Rapid Phase Modulation of THz Radiation for High Speed THz Imaging and Spectroscopy," *Optics Letters,* Vol. 33, Issue 14, pp. 1593-1595, 2008.

Yew Li Hor, John F. Federici, Robert L. Wample;
"Non-destructive evaluation of cork enclosures using terahertz/ millimeter wave spectroscopy and imaging," *Applied Optics,* Vol. 47, Issue 1, pp. 72-78, 2008.

Yew Li Hor, Hee C. Lim, John F. Federici, Eric Moore, Joseph W. Bozzelli;
"Terahertz study of trichloroanisole by time-domain spectroscopy," *Chemical Physics,* Vol. 353, Issue 1-3, pp. 185-188, 2008.

Oren Sternberg, Kenneth P. Stewart, Yew Li Hor, A. Bandyopadhyay, John F. Federici, Marc Bornefeld, Yves-L. Mathis, D. Sliwinski, Karl D. Moller, Haim Grebel;
"Square-shaped metal screens in the infrared to terahertz spectral region: Resonance frequency, band gap, and bandpass filter characteristics," *Journal of Applied Physics,* Vol. 104 Issue 2, pp. 023103-023103, 2008.

Yew Li Hor, Hee C. Lim, John F. Federici;
"Fabrication of metamaterials in THz region using ink-jet technique and characterization using THz-TDS," *2008 International Symposium on Spectra Sensing Research (ISSSR),* Steven Institute of Technology, Hoboken, New Jersey; June 23, 2008.

Yew Li Hor, Hee C. Lim, John F. Federici;
"Fabrication of metamaterials in THz region using ink-jet technique," *NJIT Physics Dept. Poster Session,* Newark, New Jersey; Apr 9, 2008.

Yew Li Hor, Hee C. Lim, John F. Federici;
"Fabrication of metamaterials in THz region using ink jet system and characterization using THz-TDS," *American Physical Society (APS) Annual meeting,* New Orleans, Louisiana; March 12, 2008.

Yew Li Hor, Hee C. Lim, John F. Federici, Eric Moore, Joseph W. Bozzelli;
"Terahertz study of trichloroanisole and its compounds by time-domain spectroscopy," *Optical Society of America (OSA) 91st Annual meeting, Frontier in Optics,* St Jose, California; Sept 15, 2007.

Yew Li Hor, Qiwen Zhan;
"Calibration of an electro-optical variable circular retarder with application in nulling microellipsometer," *Proc.SPIE Smart Structure,* San Diego, California; March 2004.

Yew Li Hor, Qiwen Zhan;
"Electro-optical nulling microellepsometer," *Great Lakes Photonics Symposium,* Cleveland, Ohio; June 2004.

ACKNOWLEDGMENT

I would like to express my appreciation to my research supervisor, Prof. John F. Federici, who providing valuable and countless resources, insight, and intuition. Special thanks are given to Dissertation Committee members Prof. Dale E. Gary, Prof. Robert B. Barat, Prof. Andrei Sirenko and Prof. Francisco Miguel Vargas Luna for participating in my committee.

I gratefully acknowledge the help of Prof. Hee C. Lim and Dr. Yew F. Hor in the Flexible Electronic Device and Sensor Laboratory for their support and knowledge transfer.

I would like to thank everyone for constructive comments and helpful advice, which reinforced my dissertation project and encouraged me to work harder. Finally, I would like to thank my father and mother, brothers and sisters, nieces and nephews, and also close collaborators and friends.

TABLE OF CONTENTS

TABLE OF CONTENTS
(Continued)

Chapter **Page**

TABLE OF CONTENTS
(Continued)

Chapter **Page**

TABLE OF CONTENTS
(Continued)

Chapter **Page**

TABLE OF CONTENTS
(Continued)

Chapter **Page**

LIST OF TABLES

LIST OF FIGURES

LIST OF FIGURES
(Continued)

LIST OF FIGURES
(Continued)

LIST OF FIGURES
(Continued)

LIST OF FIGURES
(Continued)

LIST OF FIGURES
(Continued)

CHAPTER 1

INTRODUCTION

1.1 Objective

The objective of this dissertation is to design and fabricate flexible metamaterials in three dimensions that exhibit response in the terahertz range utilizing novel microfluidic-jetted fabrication techniques. Nanogold, liquid polyimide and semiconductor polymer microfluidic inks are used for fabrication on various flexible substrates. In my thesis proposal, the magnetic ink and carbon nanotubes ink were proposed as deposited mediums. However, due to the difficulty of optimizing these fluids, the micron-size structures could not be fabricated. The fabrication samples are characterized in THz time domain spectroscopy (THz-TDS) in the transmission mode. The measured THz responses are verified with theoretical modeling utilizing commercial Excel add-in and FEMLAB software package.

1.2 The Future Material

Metamaterials (MTMs) are defined as artificial materials which achieved extraordinary electromagnetic properties that are not available in natural material. Although composite materials have been investigated for many years, MTMs really form a new field of science and engineering. If the demonstration of LHM (left-handed metamaterial) structure in 1999 by Pendry *et al.* is considered as the commencement of MTMs[1], this field is less then 10 years old in 2008. Due to their embryonic nature, MTMs have evolved rapidly in this few years. The science of MTMs, in particular LH MTMs, has

been well established theoretically, numerically, and experimentally in the literature. Theories and experiment have revealed the fascinating properties of this MTMs such as reverse Snell's law, reverses Doppler effect, reversal of Cherenkov radiation and inversion of critical angle and Brewster's angle, etc [2,3,4,5].

1.3 Size Does Matter

The dimension of the element has to be tuned to meet the effective medium condition so that it acts as a homogeneous medium to ensure that refractive phenomena will dominate over scattering or diffraction phenomenon when a wave propagates inside the metamaterials medium. Most of the experiments on MTMs have been performed at microwave frequencies due to the simplicity of fabrication as well as ease of complex transmission and reflection experiments. The first LHM proposed by Pendry *et al.* is in the microwave region and has a structure size above 1cm. The composite LHM medium consists of alternative layers of the split-ring resonators and metallic post printed on a PCB board[1].

There is a sustained effort in the community to push the operational frequency of MTMs toward the terahertz frequency region. Based on the effective medium theory, the effective structure size in terahertz region has to shrink down to micron size. Modern LHM has been introduced by Yen *et al.*[6] which was a 2-D layer of split rod and split ring resonator with element size of 50μm on quartz substrate. Other LHM exhibiting electro and magnetic response in terahertz region can be found in references[7,8,9]. These structures are fabricated using conventional or advanced clean-room MEMS technology.

1.4 Novel Technique

Nearly all of the MTMs that exist in terahertz region are single 2D layers fabricated on a rigid substrate due to the limitation of the conventional MEMs technique. In this thesis, a new fabrication technique, namely microfludic-jetted technique, for fabrication of miniature 3D structure of MTMs in terahertz region is demonstrated. This method has never been exploited yet until recently by the author. Using this novel technique, the fabricated structure, for the first time, is able to fabricate on a flexible substrate thus add the potential for future market application. Also, with this technique, miniature 3D THz MTM has been realized by the idea of stacking the structure layer by layer. The use of different fabrication materials such as nanogold, semiconductor ink even carbon nanotubes, also broadens the future application area.

This novel fabrication technique are being evaluated as precision deposition tools in a variety of manufacturing processes such as LCD (liquid crystal display)[10] and OLED (organic light emitter diode)[11]. Also, this technique offers an economic advantage in cases which the deposited material is expensive. Unlike the conventional lithography technique, the use of photoresist and active chemicals is not necessary. Thus, there is a comparative reduction in the fabrication cost and fabrication time. In addition, microfludic-jetted technique offers the advantage of non-contact deposition, therefore, minimizing contamination.

1.5 Negative Refraction Index ?

The index of refraction of MTMs is considered to be negative when the effective permittivity and permeability are simultaneously negative. As a consequence of their

double negative parameters, plane waves propagating in such metamaterials are characterized by antiparallel phase and group velocities and reversal of wave vector that follow a left-hand rule, thus giving rise to the name left-handed (meta)materials (LHM). This type of material has named by its inventor, Veselago as left-handed material (LHM)[12]. Experiment and simulation[13] have confirmed that the LHMs do indeed exhibit negative refraction. However, the experiment was done in the microwave region and the sample investigated was a bulk 3D prism slab. The question is whether the negative index of refraction property can be implemented at terahertz frequencies? Although THz-TDS has been proposed to be a technique for measuring the index of refraction of MTMs[14], but still, a negative index of refraction in terahertz region has not yet been observed. There is mainly due to the inability in fabricating the MTMs into a bulk 3D slab. So there is a need for alternative, advanced and simplified designs that can be easily fabricated and characterized.

1.6 Terahertz Time Domain Spectroscopy

In this thesis, THz-TDS in the 0.1 to 2 THz range is used to characterize the fabricated metamaterials. The 3D structure fabricated using the novel technique enables characterization to be performed in varying structure planes by tilting the material with respect to the incident terahertz beam. The potential of Terahertz (THz) spectroscopy and imaging for non-destructive evaluation of materials such as space shuttle foam[15], moisture content in grain,[16] wood,[17] pharmaceuticals,[18] liquids,[19] and explosives[20] is well documented. The key attribute of THz non-destructive evaluation is the ability of THz radiation to propagate through paper, plastic, and other non-metallic containers. In the

case of multilayer Left-handed material, the THz radiation only responds to the conductive structure but not the substrate. Furthermore, THz-TDS measurement offers more direct and simple way to obtain the frequency-dependent real and imaginary part of refractive index of the MTMs.

1.7 Finite Element Method

The popular and powerful simulation tool FEMLABs is use for simulation the response of THz wave propagated in the MTMs. The finite element method[21] is a numerical technique for obtaining approximate solutions to boundary value problems of mathematical physics. This method was first proposed in the 1940s and began to be used in the 1950s for aircraft design. Thereafter, the methods were developed and applied extensively to problems of structural analysis and increasingly to problems in other fields. Today, the finite element method has become recognized as a general method widely applicable to engineering and mathematical problems. Advantages of the finite element methods include; flexibility and accuracy in modeling due to the uses of unstructured meshes and isoparametric triangular elements; and, it is able to accurately perform wideband electromagnetic simulations.

1.8 Fill in the Gap

Terahertz, far-infrared, or sub-millimeter radiation, at frequencies from 100GHz to 30THz, is the electromagnetic spectrum sandwiched between the microwave region and infrared light. Technologies using the radiation from many regions of the electromagnetic spectrum are well developed. For example the use of radio waves, microwaves, mobile

phone and x-rays are now common nature in modern life. Several years ago, the terahertz region was often referred to the 'Terahertz gap' because of the lack of commercially available devices for this region. Gradually, the gap has been bridged with innovation devices. One very successful approach to overcoming these limitations was the development of THz-TDS, which uses femtosecond-pulse laser technology to generate and detect pulses of THz radiation. This terahertz radiation could be considered the 'final frontier' in understanding the electromagnetic spectrum.

The realization of artificial electric and magnetic materials in THz regime enables an important step in filling the gap between microwave and optical frequencies, where THz technologies suggested the potential applications in semiconductor, tomography imaging, label free genetic analysis, cellular level imaging, and biological sensing and so on. Metamaterial devices in THz range are still young compared to the gigahertz regime due to the difficulty in establishing the miniature of the effective structure lattice size. Even though a few metamaterials have been fabricated in the terahertz region as mention in Section 2.3, the resolution of the structure still needs to be improved.

CHAPTER 2

METAMATERIALS

2.1 Definition

A metamaterial is defined as an artificial created material which achieves an extraordinary electromagnetic property which is not available in natural material. Such metamaterials can consist of either artificial dielectric or artificial magnetic materials individually or combinations of both artificial materials. A metamaterial gains its properties from its structure rather than directly from its composition. The term was coined in a 2001 published paper by Rodger M. Walser of the University of Texas at Austin[22]. The definition was subsequently expanded by Valerie Browning and Stu Wolf of DARPA (Defense Advanced Research Projects Agency) in the context of the DARPA Metamaterials program that started also in 2001. They defined metamaterials as:

> *Metamaterials are a new class of ordered composites that exhibit exceptional properties not readily observed in nature. These properties arise from qualitatively new response functions that are: (1) not observed in the constituent materials and (2) result from the inclusion of artificially fabricated, extrinsic, low dimensional inhomogeneities.*

In recent years, scientific and technological interest in metamaterials has grown significantly. The extraordinary response functions of these metamaterials offer brilliant applications in technologies covering the frequency region from microwaves to visible range. Exotic properties for such metamaterials have been predicted; many experiments and theoretical simulation have confirmed the science of these metamaterials.

2.2 Categories of Metamaterials

The response of metamaterials to the presence of an electromagnetic field is determined by macroscopic parameters of permittivity ε and permeability μ of these materials. This allows for the classification of a medium as follows which are related to the refractive index n by

$$n = \pm\sqrt{\varepsilon_r \mu_r} \tag{2.1}$$

Where ε_r and μ_r are the relative permittivity and permeability related to the free space permittivity and permeability, ε_o and μ_o, respectively. In Equation (2.1), the four possible sign combination in the pair (ε, μ) are (+, +), (+, −), (−, +) and (−, −) as illustrated in the ε - μ diagram of material (Figure 2.1).

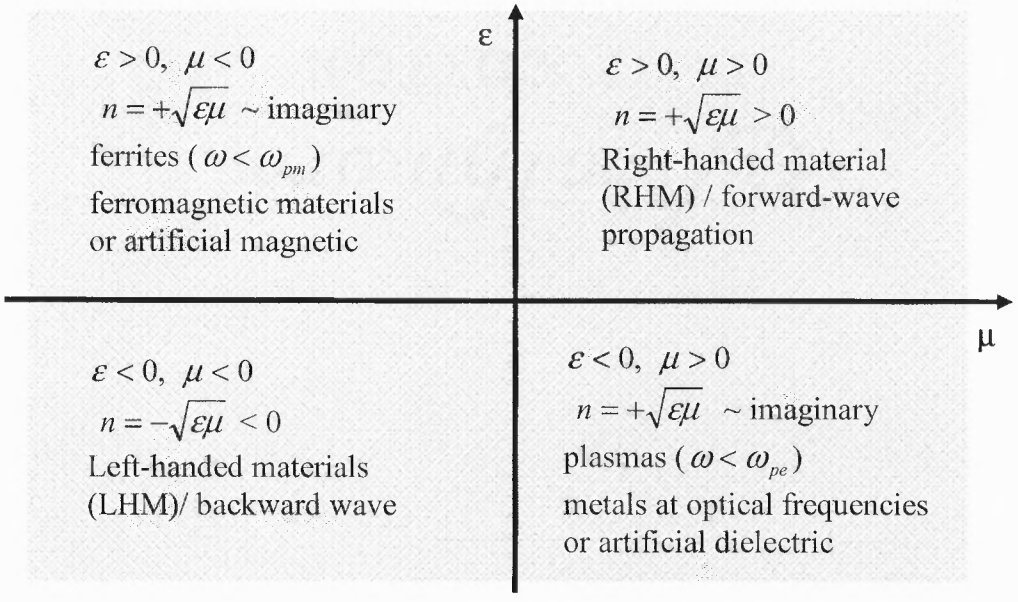

Figure 2.1 ε-μ material diagram.

A material with both permittivity and permeability greater then zero is designated as a double positive material. Most commonly occurring media or natural material falls under this designation. A material with permittivity less then zero and permeability

greater than zero is designated as an epsilon negative medium or artificial dielectric material. Many plasmas reveal this characteristic in certain frequency regimes. For example nobles metals, such as silver and gold, behave in this manner in the infrared and visible frequency region. A material with permittivity greater than zero and permeability less then zero is designated as a permeability negative medium or artificial magnetic materiel. Some gyrotropic materials exhibit this characteristic in certain frequency regimes. A material with simultaneously permittivity and permeability less than zero is designated as double negative medium. To date, this type of material has only been established with artificial constructs: a new class of materials. As a consequence of their double negative parameters, plane waves propagating in such metamaterials are characterized by antiparallel phase and group velocities and reversal of wave vector that follow a left-hand rule, thus giving rise to the name left-handed (meta)materials (LHM). Sometimes, LHM are also called as backward-wave media, negative-index materials, or even Veselago media in literature. In this thesis, the term LHM is used. LH structure has been by far the most popular of the metamaterials, due to their extraordinary property of negative refractive index.

2.2.1 Artificial Dielectric

As mentioned above, the artificial dielectric material is a material that exhibits both positive permeability and negative permittivity. The first artificial dielectric material was used in the design of low weight dielectrics lenses in microwave frequency. An example of an artificial negative permittivity material is the wire medium[23] (also call 'rod medium'), which is formed by regular lattice of conducting wires with small radii compared to the lattice periods, shown in Figure 2.2. This medium has plasma-like

frequency dependent permittivity which is negative below the plasma frequency. That is why it is often called "artificial plasma" since the ideal (collisionless) electron plasma is described by permittivity of the same form.

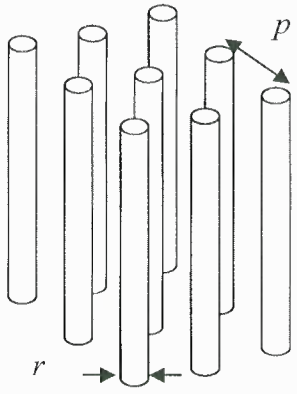

Figure 2.2 A common example of artificial dielectric structure namely wire medium or rod medium.

Other artificial dielectric materials, other than wire medium, have been invented (see Figure 2.3)[24]. The symmetric design has theoretically and experimentally been demonstrated to eliminate magneto-optical coupling effect and yield electrically resonant structures. Therefore, such symmetric elements can construct a purely electrical resonant response.

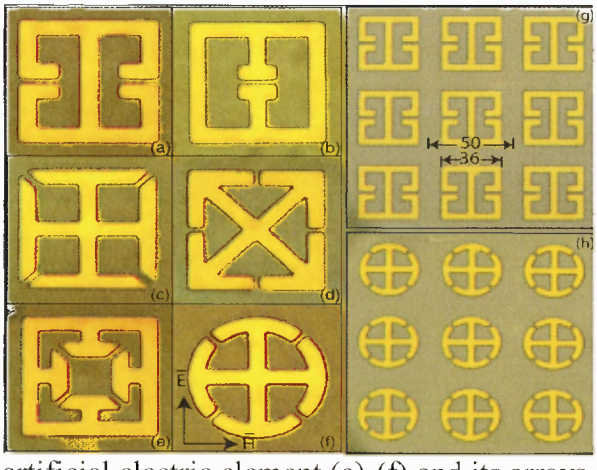

Figure 2.3 Design of artificial electric element (a)-(f) and its arrays (g), (h) from Los Alamos National Laboratory[24].

For the negative permittivity-positive permeability metamaterials, applying the excitation electric field will induces a current along the axis and generates an equivalent electric dipole moment. These metamaterials exhibits a plasmonic-type permittivity frequency function. In reference to thin wire as a medium, the permittivity derived by Pendry *et al.* has the form

$$\varepsilon(\omega) = 1 - \frac{\omega_{pe}^2}{\omega^2 + i\omega\zeta} \tag{2.2}$$

where ω_{pe} is electric plasma frequency given by equation as below

$$\omega_{pe} = \sqrt{\frac{2\pi c^2}{p^2 \ln p/r}} \tag{2.3}$$

and, ζ is the damping factor due to the metal losses

$$\zeta = \frac{\varepsilon_0 (p\ \omega_{pe}/r)^2}{\pi\sigma} \tag{2.4}$$

c, r, σ and p is the speed of light, radius of the wires, conductivity of metal and lattice size, respectively. The design rule for achieving the negative permittivity is

$$\omega^2 < \omega_{pe}^2 - \zeta^2 \tag{2.5}$$

2.2.2 Artificial Magnetic

Artificial magnetic materials, which have negative permeability and positive permittivity, are usually composed from elements that are resonant. The typical magnetic resonators are split ring resonators (SRR) as shown in Figure 2.4[25]. An artificial magnetic formed by SRR possesses negative permeability within the narrow band frequency near the resonant frequency of the split ring resonators. A variety of shapes and designs have been developed including the single split ring resonator, and s-shape resonator.

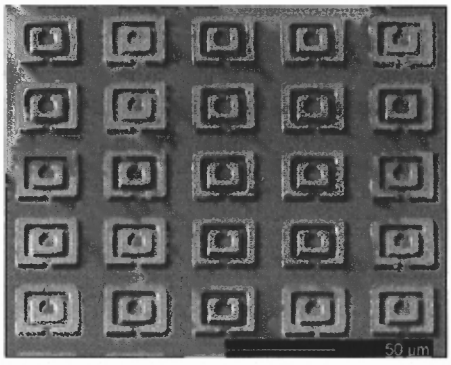

Figure 2.4 Scanning electron microscope image of the double split ring resonator in micro size [25].

For negative permeability metamaterials, the excitation magnetic field H perpendicular to the sample plane will induce resonating currents in the loop and generate an equivalent magnetic dipole moment. Using the double ring SRR as an example, this metamaterial exhibits a plasmonic-type permeability frequency function of the form

$$\mu(\omega) = 1 - \frac{F\omega^2}{\omega^2 - \omega_{om}^2 + i\omega\zeta} \tag{2.6}$$

where ω_{om} is magnetic resonance frequency,

$$\omega_{om} = c\sqrt{\frac{3p}{\pi \ln(2w/\delta)r^3}} \tag{2.7}$$

and the damping factor due to metal losses is

$$\zeta = \frac{2p\rho}{r\mu_0} \tag{2.8}$$

where w, δ, r, ρ are the width of the ring, radial spacing between the ring, inner radius of small ring and metal resistance per unit length. F is filling factor based on the geometry of the SRR structure. In order to obtain negative permeability, the incident frequency must fall in range as shown in Equation 2.9

$$\omega_{om} < \omega < \omega_{pm} \tag{2.9}$$

where,

$$\omega_{pm} = \frac{\omega_{om}}{\sqrt{1-F}} \tag{2.10}$$

2.2.3 Left-handed Metamaterials

A special place within metamaterials is occupied by double-negative media (DNG): material which has both negative permittivity and permeability. The properties of such materials were analyzed theoretically by Veselago in 1968[12]. Veselago introduced the term ''left-handed materials'' based on its reverse direction of energy flow given by $\vec{E} \times \vec{H}$. Growing interest in these exotic media was propelled only after D.R. Smith created a first prototype of LHM consisted of a combination of the SRR which exhibits negative permeability and wire grids which provide the negative dielectric behavior[25] as shown in Figure 2.5(a). Modern LHM has also been introduced[26] which consists of a 2D layer of rod and split ring resonator as shown in Figure 2.5(b) that possess an electromagnetic response in the terahertz regime.

Electromagnetic waves in LHM will result in unusual reversed propagation phenomena which are due to the combination of the negative ε and μ obtained from microstrips and SRR. The unusual phenomena include backward wave, negative refraction, reverse Doppler and Vanilov-Cherenkov effects, etc. The details of the LHM phenomenon will discussed in the following section of this chapter.

LHMs attract attention due to very interesting applications. Many researchers from all over the world are studying various aspects of this class of metamaterial. Several ideas and suggestions for future application of these materials have been proposed. Some current application will be listed and discussed in this chapter.

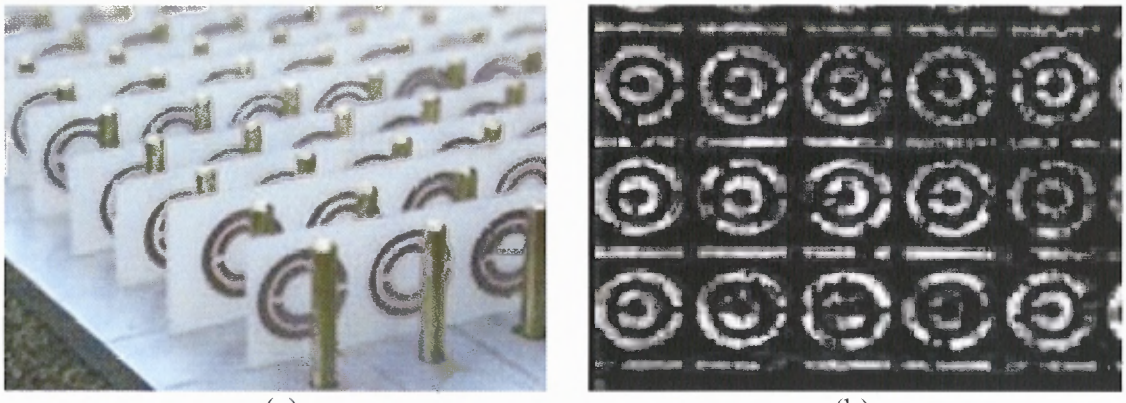

(a) (b)

Figure 2.5 Examples of LHM (a) The composite LHM employed by Smith *et al.* the medium consists of a split-ring resonators, printed on a circuit board, and metallic post[25] and (b) Modern LHM, Rod-Split-Ring-Resonator in 2D, 80 μm of element size[26].

2.3 A Historical Overview

The first ever known metamaterials were artificial dielectric metamaterials developed by W.E. Kock in the late 1940's[27] and used in the design of low-weight dielectric lenses at microwave frequencies. These materials which consist of artificially created dielectric or metallic 'molecules' in certain shape, imitate natural materials. Another artificial dielectric MTM is the wire medium[23] (also called rod medium) which has been known since the 1960s. The most recent artificial dielectric material, other than metal wire, for frequencies of a few terahertz, (see Figure 2.3), has been invented last year by W. J. Padilla *et al.* of Los Alamos National Laboratory[24].

Artificial magnetic materials have no shorter history than artificial dielectrics. The most popular artificial magnetic are described in detail in Reference 28 but they have been known for a long time before that, since the 1950s[29]. The typical magnetic elements are split-ring resonators and Swiss rolls.

LHM were theoretically investigated by V.G. Veselago in 1968[12]. His study showed that the direction of the Poynting vector for a monochromatic uniform plane

wave in LHM is antiparallel to the direction of phase velocity, conversely to the case of plane wave propagation in conventional simple medium.

J.B. Pendry was the first person who theorized a practical way to make a LHM. His initial idea was to utilize the metallic wires aligned along the propagation direction to provide a metamaterial with negative permittivity. The challenge was to construct a material which showed negative permeability. In 1999, Pendry demonstrated that an open ring ('C' shape) with axis along the propagation direction could provide a negative permeability[28]. In the same paper, he showed that a periodic array of wires and rings could give rise to a negative refractive index medium. Since then, LHM has grown rapidly in microwave region. Another related negative permeability particle which was also proposed by Pendry is the swiss roll[28].

Most of the experiments on metamaterials have been performed at microwave frequencies due to the simplicity of fabrication as well as ease of complex transmission and reflection experiments[13, 30, 31]. There is a sustained effort in the community to push the operation frequency of metamaterials toward the terahertz frequency region. The first SRR in THz region is created by Yen *et al.*[32] which demonstrated that the inherently nonmagnetic SRR could exhibit strong magnetic response in the terahertz frequency region. The dimension of their design is about ~50μm on quartz substrate using self-aligned microfabrication technique called photo-proliferated process. Fourier transform infrared spectroscopy from 0.6 THz to 1.8 THz was used, which shows these SRR exhibit a magnetic resonant frequency at 0.8, 0.88 and 1.15 THz for element lengths of 36μm, 44μm and 50μm. A similar work has been continued by H. O. Moser *et al.*[14] with a different structure, which is a combination of the microstrips and SRR on a planar

substrate that possessed both electric and magnetic resonance. The transmission property of planar composites of double-ring-SRR was studied for the first time in time domain terahertz spectroscopy by Oklahoma State University's terahertz group[33]. At the same time, Los Alamos Laboratory investigated its dynamical electric and magnetic respond using THz-TDS[8, 24, 34]. The structures were fabricated upon a highly resistive GaAs substrate which acts as a fast photoconductor when the substrate is illuminated on the carriers in the substrate. The free carriers shunt the gap of the SRR hence providing a symmetric structure that effectively turns off its magnetic response. This work, for the first time, demonstrates that SRR can be dynamically controlled and implemented as a terahertz switch. Based on the recently advanced fabrication technologies, there are also reports of characterization of negative index material in the far infrared region and in optical spectra[35,36,37].

2.4 Fundamental Phenomenon of the LHM

2.4.1 Backward Wave

For a plane wave travelling in a conventional medium, the Maxwell's first order differential equations are explicitly reduced to

$$\vec{k} \times \vec{E} = \omega \mu \vec{H}$$

$$\vec{k} \times \vec{H} = -\omega \varepsilon \vec{E} \tag{2.11}$$

However, for simultaneous negative ε and μ, the above equations are reduced to

$$\vec{k} \times \vec{E} = -\omega |\mu| \vec{H}$$

$$\vec{k} \times \vec{H} = \omega |\varepsilon| \vec{E} \tag{2.12}$$

Therefore, for right-handed material (RHM), $\vec{E}, \vec{H}$ and $\vec{k}$ form a right-handed orthogonal system of vectors and for LHM, the $\vec{E}, \vec{H}$ and $\vec{k}$ form a unusual left-handed triad. This is thus where the name of Left-handed materials originates.

The direction of the time-averaged flux of energy is determined by the real part of the Poynting vector,

$$\vec{S} = \frac{1}{2}\vec{E} \times \vec{H}^* \tag{2.13}$$

which is unaffected by a simultaneous change of sign of ε and μ. Thus, $\vec{E}, \vec{H}$ and $\vec{S}$ still form a right-handed triad in LHM. Therefore, energy and wavefronts of LHM travel in opposite directions resulting in backward propagation. Figure 2.6 illustrates the orientation of $\vec{E}, \vec{H}, \vec{S}$ and $\vec{k}$ in right handed and left-handed medium. Backward-wave propagation is a unique property of LHM even though it may also appear in a nonuniform waveguides. As will be shown, most of the surprising unique electromagnetic properties of these media arise from this backward propagation property.

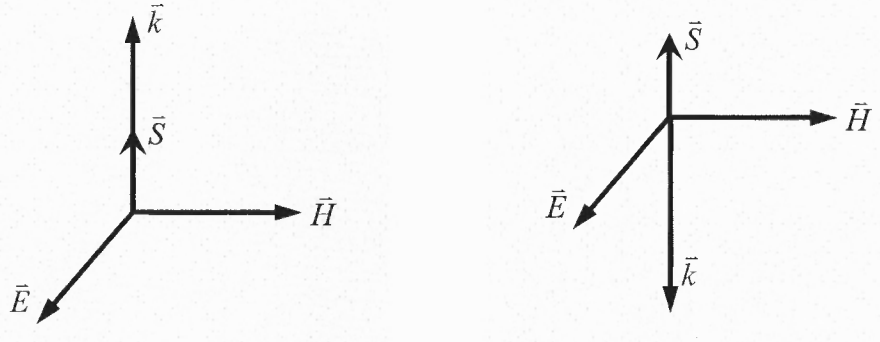

Figure 2.6 System of vectors $\vec{E}, \vec{H}$, $\vec{S}$ and $\vec{k}$ for a plane wave in (a) RHM and (b) LHM.

2.4.2 Phase and Group Velocity

Backward-wave propagation implies opposite signs between phase and group velocity. In fact

$$\frac{\partial k^2}{\partial \omega} = 2k\frac{\partial k}{\partial \omega} = 2\frac{\omega}{v_p v_g} \tag{2.14}$$

where Phase velocity and Group velocity of wave propagate in the medium is define as

$$v_p = \frac{\omega}{k} \text{ and } v_g = \frac{\partial \omega}{\partial k} \tag{2.15}$$

In addition, the dispersion relation of the medium is

$$k^2 = \omega^2 \varepsilon\mu \tag{2.16}$$

$$\frac{\partial k^2}{\partial \omega} = \omega\varepsilon\frac{\partial(\omega\mu)}{\partial \omega} + \omega\mu\frac{\partial(\omega\varepsilon)}{\partial \omega} \tag{2.17}$$

Since $\frac{\partial(\omega\varepsilon)}{\partial \omega}$ and $\frac{\partial(\omega\mu)}{\partial \omega}$ must be larger than zero for positive energy density. Consequently $\frac{\partial k^2}{\partial \omega}$ must be negative. Therefore, from Equation 2.14, it follows that $v_p v_g < 0$. The negative wave vector in a LHM leads to negative phase velocity. Therefore, the group velocity must be positive in order to fulfill the $v_p v_g < 0$ condition. It follows that in LH medium phase, which is related to phase velocity v_p, the wave propagates backward to the source in the opposite direction of the power (Poynting vector), related to group velocity v_g. This implies that the wavepacket and wavefront are travelling in the opposite directions.

2.4.3 Reversal of the Boundary Condition

From Maxwell's equations, the boundary conditions[38] at the interface between two media in the absence of charge and sources are

$$\hat{n}\cdot(\vec{D}_2-\vec{D}_1)=0$$

$$\hat{n}\cdot(\vec{B}_2-\vec{B}_1)=0$$

$$\hat{n}\times(\vec{E}_2-\vec{E}_1)=0$$

$$\hat{n}\times(\vec{H}_2-\vec{H}_1)=0 \qquad (2.18)$$

where $\hat{n}$ is a unit vector normal to the interface pointing from medium 1 to medium 2. The upper two equations state that the normal component of $\vec{D}$ and $\vec{B}$ are continuous, whereas the lower two equations state that tangential components of $\vec{E}$ and $\vec{H}$ are continuous:

$$\vec{D}_{1n}=\vec{D}_{2n}$$

$$\vec{B}_{1n}=\vec{B}_{2n}$$

$$\vec{E}_{1t}=\vec{E}_{2t}$$

$$\vec{H}_{1t}=\vec{H}_{2t} \qquad (2.19)$$

where t and n stand for tangential and normal, respectively.

Now, consider the specific case of an interface between RH and LH media. Since the relations on the tangential components do not depend on ε and μ, the boundary conditions on the tangential components of $\vec{E}$ and $\vec{H}$ are unaffected at interface. But the boundary conditions on the normal components are altered, since they depend on ε and μ with changes in signs. Therefore, the boundary conditions at RH/LH interface are

$$\vec{E}_{1n} = -\frac{|\varepsilon_2|}{|\varepsilon_1|}\vec{E}_{2n}$$

$$\vec{H}_{1n} = -\frac{|\mu_2|}{|\mu_1|}\vec{H}_{2n}$$

$$\vec{E}_{1t} = \vec{E}_{2t}$$

$$\vec{H}_{1t} = \vec{H}_{2t} \qquad (2.20)$$

Thus the tangential components of $\vec{E}$ and $\vec{H}$ remain continuous while their normal components become antiparallel at the interface between a RHM and LHM.

2.4.4 Reversal of Snell's Law

The consequences of negative refractive index when LHM is interfaced with RHM can be seen from Snell's law. Consider a plane wave incident from a medium (e.g. vacuum) with n>0 onto a medium with n<0. If θ_1 and θ_2 are the angles of incident and transmission, respectively, then according to Snell's law;

$$\sin\theta_1 = n\sin\theta_2 \qquad (2.21)$$

From the equation, negative n lead to negative values of $sin\ \theta_2$ implies that the transmitted rays make a negative angle with respect to the normal of the interface. In other words, the refracted rays are bent to the opposite side, as shown in Figure 2.7, compared with the conventional case. Experimental evidence for this aspect of LHM is discussed[39].

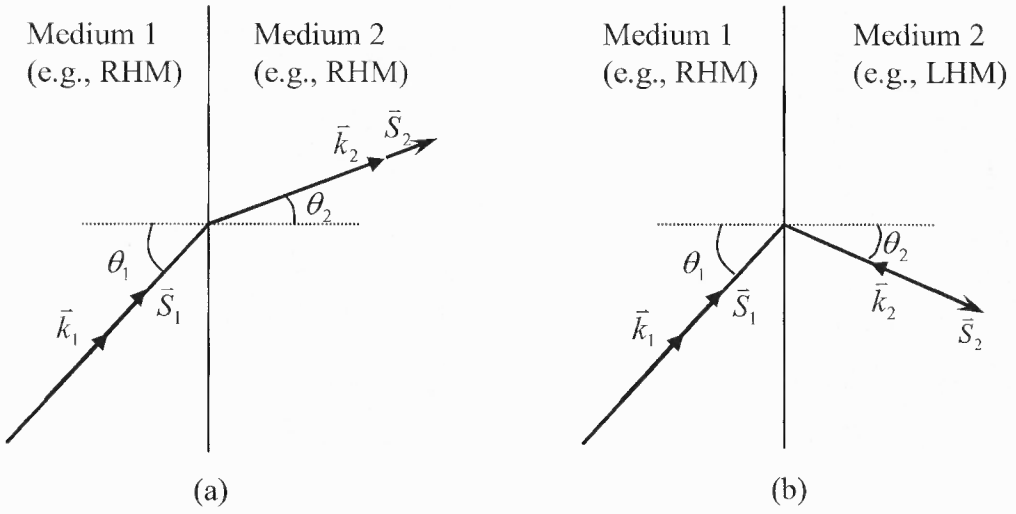

Figure 2.7 Refraction of an electromagnetic wave at the interface between two different media (a) case of media of same handed (either RH or LH) (b) case of two media of different handed (one RH and other one LH).

2.4.5 LH Effect of Flat, Concave and Convex Lenses

A double focusing effect can be obtained from a flat LH slab sandwiched between two RH media. As illustrate in Figure 2.8, the rays radiated from a source at the distance l from the first interface is focused in two locations, in the slab with distance s from the first interface and refocus in the second RH medium. The first focus distance s is obtain by simple trigonometric considerations as

$$s = l\frac{\tan\theta_{RH}}{\tan|\theta_{LH}|} \tag{2.22}$$

where the angle θ_R is the incident angle θ_L is obtain by Snell's law

$$\theta_L = -\sin^{-1}\left(\frac{n_{RH}}{n_{LH}}\sin\theta_{RH}\right) \tag{2.23}$$

If the LHM and RHM have the same electromagnetic density, where $n_{LH} = -n_{RH}$, then focusing is obtained at the mirror image of the source. Since $\theta_{RH} = \theta_{LH}$, each pair of rays

will focus at the same point so that the focus distances are the same for all pairs of rays. If the electromagnetic density of the two media are different, then rays with different incident angles refract to different focal point because the different ratio of $\tan\theta_{RH} / \tan|\theta_{LH}|$ for different pairs of rays which lead to different focal distances. In this case, the focal point degenerates into a diffuse focal spot as a consequence of spherical aberrations. This is the drawback of the LHM flat lens.

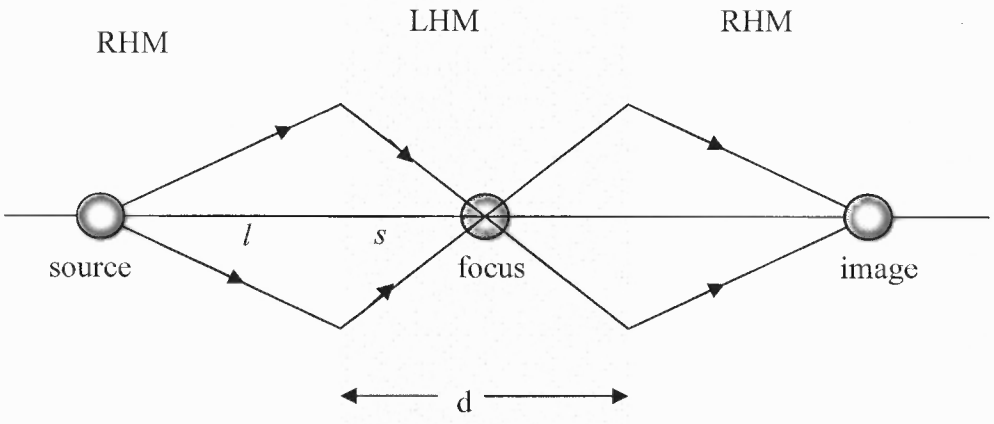

Figure 2.8 Double focusing effect in the LHM flat lens sandwich between RH media.

The principle of geometrical ray optics laws maybe revisited in the light of the unusual and exotic effects achieved with LH lenses[2]. Figure 2.9 illustrates the reversal of the convergence and divergence effects of the LHM convex and concave lenses, respectively. The focal length on a thin lens is given by

$$f = \frac{R}{|n-1|} \tag{2.24}$$

where R is the radius of the curvature of the lens. From this formula, it appear that for a given R, a LH lens with an index of n=–1 would have the same focal length as a conventional lens of index n=+3. Therefore, a LH lens would have a smaller focal length and would be more compact compared to a RH lens with the same index magnitude.

Another potential benefit of LH lenses is that a LH lens of n=−1 would focus electromagnetic waves with a focal length of f=R/2 whereas a RH lens with the same electromagnetic density, n=+1 would not.

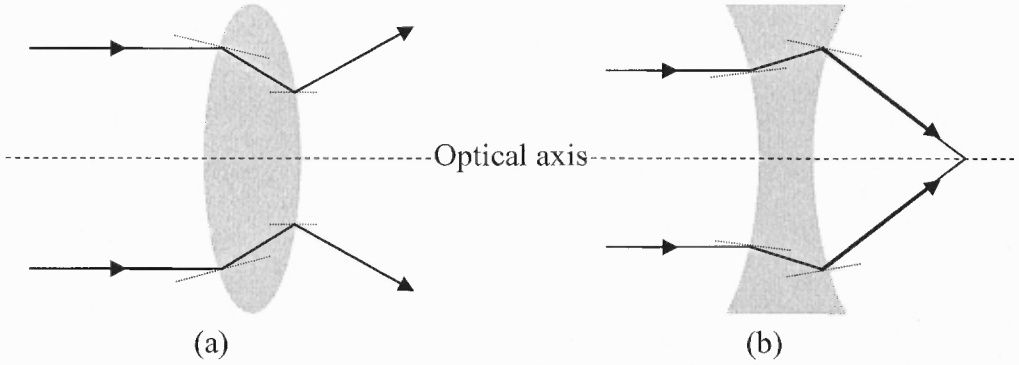

Figure 2.9 Convergence and divergence of ray in the LHM lens. (a) LH convex lens consequence diverging rays and (b) LH concave lens consequence the converging rays.

2.4.6 Reversal of Doppler Effect

Consider an electromagnetic radiating source S moving along z direction as illustrated in Figure 2.10. In the far-field, the radiated fields have the form

$$\vec{E}(z,t),\vec{H}(z,t) \;\alpha\; \frac{e^{i\varphi(\omega,t)}}{r} \tag{2.25}$$

with the phase $\varphi(\omega,t)=\omega t-\vec{k}\cdot\vec{r}$, where k represents the wave number and r the standard radial variable of the spherical coordinates system. If the source moves towards the positive direction of z with a velocity v_s, its position as a function of time is $z=v_s t$. Thus, the phase seen by an observer O is developed as follows

$$\varphi=\omega t-kv_s t=\omega(1-\frac{k}{\omega}v_s)t=\omega(1-\frac{v_s}{v_p})t=\omega(1-s\frac{v_s}{v_p})t \tag{2.26}$$

where s is the handedness sign function where negative sign represent LHM and vice versa.

The Doppler frequency $\omega_{Doppler}$ is the difference of the frequency ω of the source and the Doppler frequency shift $\Delta\omega$,

$$\omega_{Doppler} = \omega(1 - s\frac{\upsilon_s}{\upsilon_p}) \tag{2.27}$$

$$\Delta\omega = \omega\frac{\upsilon_s}{|\upsilon_p|} \tag{2.28}$$

In a RH medium, $\Delta\omega>0$ since s =+1 and, therefore, the frequency measured by the observer looking at the receding source is shifted downward or "red-shifted", as illustrated in Figure 2.10; on the other hand , an observer located on the right-hand side of the source, seeing a proceeding source, would measure a frequency shifted upward or "blue-shifted". In a LH medium, because s=−1, the Doppler frequency of a receding source is blue-shift, whereas that of a proceeding source is red-shifted.

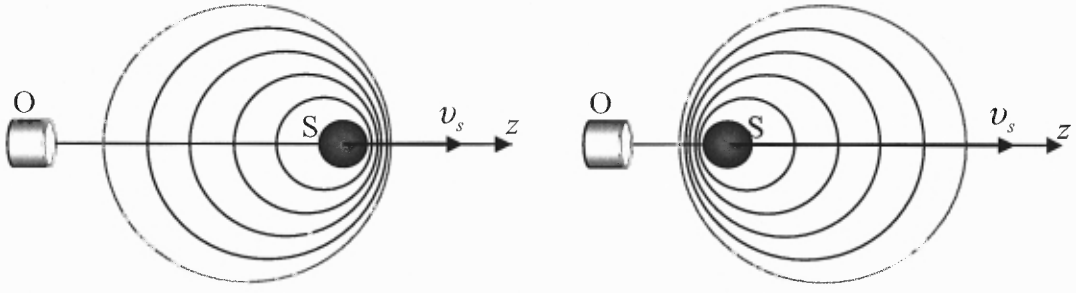

(a) (b)

Figure 2.10 Doppler Effect of (a) RHM and (b) LHM.

2.4.7 Reversal of Vavilov-Cerenkov Radiation

Vavilov-Cerenkov radiation is the visible electromagnetic radiation emitted by liquids or solids when bombarded by fast-moving electron beams which exceed the velocity of light. Consider a single electron e of charge q moving at the velocity υ_e along a direction z, as illustrated in Figure 2.11 In considering the wave like nature of matter, the isolated

electron considered is a wave, and therefore, the phase velocity is the same as the velocity of electron. Vavilov-Cerenkov radiation is directive, with a radiation angle depends on the velocity of the electron. Thus the radiation angle is

$$\theta = \sin^{-1}\left(\frac{c}{v_e}\right) \tag{2.29}$$

where c is the velocity of light.

It is obvious that in a RH medium, Vavilov-Cerenkov radiation occurs at positive angles since k is positive. Since $k<0$, wave propagation is backward in LHM, Vavilov-Cerenkov radiation occurs at negative angles. This implies that in LHM, a source generating a modulated beam of electrons toward positive direction of z, the group velocity carrying power would naturally propagate toward positive z direction, whereas the electron wave would propagate backward. A theoretical study of Vavilov-Cerenkov radiation in LHM is presented in Reference 40.

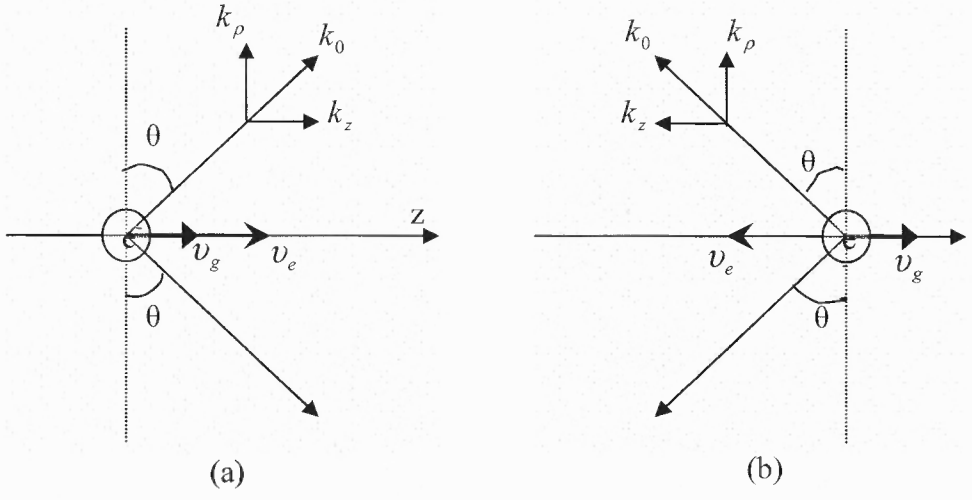

Figure 2.11 Vavilov-Cerenkov radiation. (a) in conventional medium ($\theta>0$) and (b) in LHM ($\theta<0$) indicate the reversal of Vavilov-Cerenkov radiation.

2.4.8 Negative Goos-Hänchen Shift

When a beam of finite extent is incident from medium 1 to medium 2, where the refractive index of medium 2 is larger than medium 1 and the incident angle exceeds the critical angle so that total reflection occurs, the reflected beam experiences a finite lateral shift Δ called Goos-Hänchen shift as illustrate in Figure 2.12. The lateral shift is the consequence of a nonuniform plane wave which penetrates into medium 2 by a small distance, forming an evanescent wave in the direction normal to the interface and propagated along the interface. For ordinary medium 2, power associated with this plane wave flows parallel to the interface in the forward direction. The Goos-Hänchen shift must be positive in ordinary media. However if the medium 2 is a left handed medium, energy flow and wavefront propagation are anti parallel. Therefore, the Goos-Hänchen shift must be negative. The Goos-Hänchen effect occurring in layer structure of negative refraction index has been analyzed in detail[41].

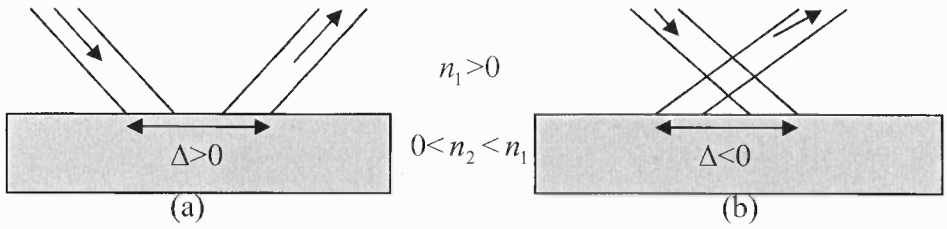

Figure 2.12 Goos-Hänchen effect. (a) Conventional case, at the interface between two RH media. (b) The reversed effect, at the interface between a RH and A LH medium.

2.5 Metamaterial Current Applications

Metamaterial technology is a breakthrough, due to the controllable electromagnetic properties of the materials level that was not available in natural materials. This advantage offers brilliant application in developing the novel components and

subsystems. In addition, metamaterials offer a very promising prospective that could overcome the limitations of current technology, covering the frequency range from microwave to visible range. The novel ideas expand this rapidly developing scientific area with extremely high rate, and promising effects attract researchers from various scientific communities. Below, is listed a few recent developments of metamaterials in industrial applications.

2.5.1 Superlens

All conventional RH lenses suffer from a diffraction limit which cannot focus the electromagnetic radiation onto an area smaller than the square wavelength. The LHM lens that is described by Veselago achieves "perfect imaging" since it focuses the source and object propagating waves and restores the amplitude of the evanescence wave at the focal plane. The LHM lens completely regenerates the source plane at the internal and external focal planes as discuss in the above section. The "perfect lens" predicted by Pendry only occurs when the lens and the surrounding RHM are lossless and two specific condition are met. The conditions are 1) impedance matching in LH and RHM and 2) LH and RH materials must have relative index of -1 with respect to each other. The first condition eliminates any reflections at the interfaces of the LHM lens and the second condition ensures there are no aberrations.

The first superlens with a negative refractive index provided resolution three times better than the diffraction limit of conventional lens and was demonstrated at microwave frequencies at the University of Toronto by A. Grbic and G.V. Eleftheriades[42]. To make a perfect lens, one also needs zero dissipation and amplification of evanescence wave. Metamaterials typically lower the dissipation but do not make it

exactly zero. Exactly zero dissipation is physically impossible. In fact, the dissipation is usually strong near the resonant frequencies, thus more problematic. Also, the amplification of the evanescence wave in LHM becomes ambiguous at high frequencies due to the inability of well defining μ. Therefore, at high frequency, a superlens is physically hard to establish. The first optical superlens which exceeds the diffraction limit was created and demonstrated by Xiang Zhang *et al.* of UC Berkeley[43]. However, they used a thin silver film to enhance the evanescent modes through surface plasmon coupling instead of using LHM.

2.5.2 Cloaking

Cloaking of an entity from electromagnetic fields refers to reduce the total scattering cross section of the object. In science fiction, a cloaking device refers to the advanced stealth system which causes an object, such as a spaceship or individual, to be invisible and undetectable with sensing instrumentation. Since 2005, cloaking devices are no longer just science fiction. The theoretical possibility of using plasmonic and metamaterials for reducing the scattering from spherical objects whose dimensions are comparable with the incident wavelength has been considered[44]. The key aspect is that the propagating wave within a metamaterial can be "bent" without any reflection or scattering. Thus, a metamaterial shell can be used to guide electromagnetic wave propagation around and passing the shielded entity, rendering it "invisible" since no information in terms of phase or directional change is present in the electromagnetic wave[45]. This capability was proposed for use in concealing objects within a metamaterial cloak[46,47]. The first experimental of this cloaking effect is demonstrated by Schurig *et al.*[48]. The experiment demonstrated the use of a cylindrical metamaterial consisting of

concentric shells of split ring resonators as a cloaking device in the microwave region. The guiding was achieved by tuning the geometric parameters of the SRRs for appropriate permeability values. Numerical simulations for the cloaking effect are also demonstrated[49,50]. Another proposal involving metamaterial based cloaking is hiding the presence of nearby objects by resonate the scattered light from the nearby particles with the metamaterial. This will cause the trapped light cancel out and thus effectively hiding the object from view[51].

2.5.3 Planar Circuit and Waveguide Miniaturization

An efficient waveguiding structure is required for microwave and sub/ millimeter wave components. In spite of the maturity of standard waveguiding principles, established methods encounter the limitations due to cost issues at low frequencies or with regard to losses at higher frequencies. Photonic bandgap (PBG) materials have demonstrated interesting waveguiding properties which enable very attractive loss levels e.g. below 0.25 dB/m at 18 GHz[52,53]. However, such concepts usually required large areas for implementation. Reduce the size of the component such as a waveguide and circuit, is a key to reducing the cost of the system. A highly interesting potential for LHM was demonstrated by Caloz *et al.* in terms of transmission line and circuit integration[54]. A reduction of the footprint of a simple transmission line based component, a diplexer including two filter and transmission line structures, was demonstrated to be achievable within an area, which reduces the component space in comparison to a typical solution. This example illustrates the huge components integration and cost reduction potential. Broad applications of this effect are therefore foreseen, especially in mobile terminal

equipment area where increase complexity has to be achieved at increasing spatial and cost constraint.

Waveguides consisting of metamaterials can exhibit have extremely unusual dispersion characteristics in comparison to standard waveguides. Examples of LHM waveguides include coupled cavity waveguides[55], backward lines, etc. The dispersion controllability of the LHM is an extremely attractive characteristic to provide more compact component space and therefore, reduce the cost of the device such as phase shifters and delay lines that can find applications e.g. in communication systems[56]. Recent developments are focused on combination of backward and forward lines[57]. This combination allows simultaneously adjust of the characteristic impedance and propagation constants of a waveguide, thus provide ability for matching over broad frequency ranges.

2.5.4 Antennas / Antenna Arrays

Metamaterials provide excellent opportunities for optimizing the radiation characteristic of an antenna due to its tunable capability in electromagnetic wave propagation. The intense interest has been shown in the recent design of multiple input multiple output (MIMO) communication systems where antennas arrays are used to transmit and receive the information simultaneously. However, the interaction between the antennas is a disturbing factor when they are placed in close proximity. The used of Non-resonant metamaterials such as the wire medium in this steerable antenna array[58] design which would received and transmit signal in only one direction and thus eliminate the interference noise. This has wide benefits for wireless communication technologies as well as microwave and millimeter wave imaging applications. Recent work has also

addressed the combination of LHM and RHM for antenna applications. Using RHM/LHM composites novel backfire-to-endfire leaky wave antennas can be realized, enabling for the first time the realization of full-space scanning antennas[59].

Other examples include single-excitation dual-band antennas[60]. Antennas with a directive radiation with a best half-power beamwidth of 10° can be achieved with acceptable radiation-power gain within a certain frequency range[61]. Intense work has also been dedicated at using LHM for the reduction of antenna size, while maintaining a reasonable performance.

2.5.5 Application of Tunable Materials

Under appropriate configurations of metamaterial, small variations of the size and structure may lead to radical changes of its properties. Tunable devices or components can therefore, be realized much more effectively in metamaterials, leading to more efficient modulators, broadly tunable components, enhance flexibility of the systems, etc. These opportunities can be widely explored for communication purposes, particular enhancing the performance in cellular phones component such as antenna, filter and signal amplifier. Several telecommunication companies are involving their effort in this research era. The use of metamaterials has extended interest in sensing applications e.g. for biochips to enhance sensitivity.

CHAPTER 3

FABRICATION

3.1 Effective Medium

The essential theoretical framework in the study of the metamaterials is the effective medium approach [62] which enables calculation of the effective permittivity and permeability. This effective medium approach introduces an effective homogeneous structure whose structural average cell size p is much smaller than the guided wavelength. A composite metamaterial may behave as a homogenous medium at wavelengths much longer than one of its characteristic spatial scale, such as its lattice period. Due to the concept of homogeneity of the effective unit cell, LHM can support unusual phenomenon like negative refraction and subwavelength focusing. Furthermore, knowing the effective medium parameters of a metamaterial is useful for studying its wave propagating characteristics.

Effective medium theory calculates effective properties for media with located symmetric inclusions. When a wave propagates inside the metamaterials medium, the refractive phenomena will dominate over scattering or diffraction phenomenon[2] if the average cell size, p, is at least smaller than a quarter of the incident wavelength, $p < \frac{\lambda}{4}$. Under this situation, the structure behaves as a homogeneous material and electromagnetic waves only probe the average well-defined macroscopic constitutive parameters which depend on the features of the unit cell. As shown in Figure 3.1 (a) for unit cell much smaller than the incident wavelength, interference effects cannot take place because the phase difference between adjacent cells is negligible. Instead, the wave

simply travels through the material in a straight line, thus probing average or effective constitutive parameters.

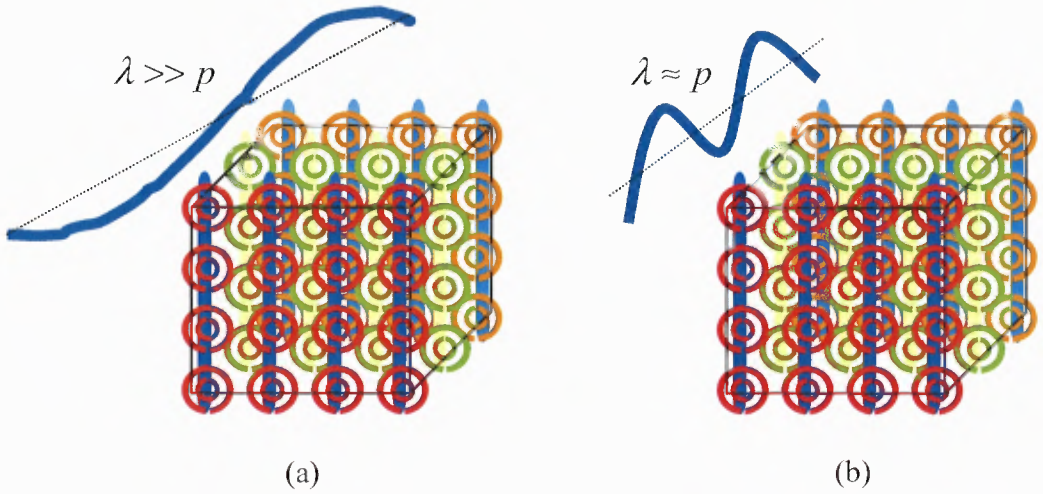

Figure 3.1 Wave propagated in MTMs medium (a) long wavelength propagate through the medium which shows no scattering effect (b) short wavelength close to lattice size of the structure that exhibits scattering effects.

3.2 Conventional Techniques

3.2.1 Screen, Stencil and Circuit Board Fabrication Technique

The early MTMs fabrication is based on mostly conventional circuit board fabrication[63]. The process consists of negative etching off the unwanted pattern of a thin conductive metal layer such as copper that covers on the surface of the insulating substrate. This process undergoes a chain of chemical reactions leaving the desired pattern (e.g. SRR or microstrips) on the surface of substrate. Due to the limited resolution, this process is only ideal for fabricating of structure size used in microwave region which the structure size is above 1cm. Sometimes, in order to produce time and cost effective product, screen and stencil printing are used[64]. However, the structures suffer from the poor resolution.

3.2.2 Photolithography

Photolithography is a process used in microfabrication. Similar to circuit board fabrication, this process is selectively remove parts of the conducting materials and leaving pattern remains on the substrate[65]. Photolithography shares the some fundamental principles with circuit board fabrication except it uses light to transfer a geometric pattern from a photomask to a light-sensitive chemical, (photoresist) on the substrate.

The process begins with the generation of the pattern layout using design software. This information is then transferred to a photomask pattern generator, which the pattern is drawn by a laser on a quartz plate covered with a thin layer of chrome and a light sensitive material called photoresist. This quartz plate is then developed and the chrome is etched, creating the photomask. Light is passed through the photomask, exposing the photoresist on the wafer and creating the blueprint that will be deposited on it. A series of chemical treatments then etch the exposure pattern into the desired structure.

This step is like an ultra high precision version of the method used to make printed circuit boards. This method offers exact control over the shape and size of the created objects. In THz region, λ/p ~10 are achievable with conventional micro-fabrication methods. Yen *et al.* fabricated a SRR structure with a resonance around 1THz[32]. They have successfully reduced the structure size to the order of ten microns. However, in the microfabrication process, defects in the samples are generally induced due to poor adhesion of the photo resist and metal film on quartz substrate. During the development process, some of the resist pattern can peel off from the quartz resulting in defects such as imperfectness of the ring, residue metal and side-wall. Although an

improved method of microfabrication has been invented with the adhesion enhanced by spinning down the hexamethlydisilazane (HMDS) on the quartz before spinning photoresist[66], still, this technique is expensive, complicated and time consuming.

3.2.3 Nanolithography

When the size of the devices shrinks toward the nanometer range, a battle is on to develop next generation microlithography technologies capable of resolving nano features. The technique, called nanolithography[67] which improves upon microlithography, using, for example improved lenses and photomasks, capable of fabricating minimum feature size of 130nm or smaller. Other alternate nanolithography lead beyond that scale includes dip-pen lithography, nanoimprint, X-ray, electron beam and ion beam.

Dip-pen lithography uses a small tip as a "pen" to deposit molecules on a surface. This tip is imitating an atomic force microscope (AFM) tip but coated with thin film of molecules. During the process, the molecules, follow the tip movement, migrate from tip to surface of the substrate and make a nanoscopic pattern. This technique can achieve very small sizes, but currently cannot go below 40nm.

The idea of nanoimprint is to embboss a pattern on the surface using the prepared piece of nanostructured material as a "stamp" that is pressed against the surface leaving a characteristic pattern behind. These techniques are sometimes used with combination of UV exposure which stabilizes the pattern.

Electron/ ion beam lithography uses a scanning electron/ ion microscope for writing patterns on surfaces. Due to the electron irradiation, the material locally changes its properties which can then be used to selectively 'etch' the irradiated sample. In this method, incredibly small sizes (in the order of 20nm) may be achieved. However,

Electron-beam lithography is much more expensive and time consuming making it a difficult sell for industry applications of nanolithography. X-ray lithography functions similarly to Electron beam lithography except it use X-ray photon instead of electron.

The use of nanofabrication is expected to dominate the production of metamaterials structured on a nanometer scale. Metamaterials possess electromagnetic behaviors that respond in far infrared and optical region have been established using technique mention above. New nanofabrication technologies are constantly being researched and developed, leading to smaller and smaller possible sizes. However, many problems occur when one wants to precisely position the atoms or molecules specific location on surfaces. Some of the problems are due to the quantum nature of atoms. This poses an important technological difficulty and raises the cost of this technique.

3.3 The Novel Microfluidic-jetted Technique

As mention, an array of conducting elements act as an effective medium when the radiation wavelength is much larger than the element lattice spacing that is $p<<\lambda$. Therefore, the fabrication of structure in microwave region is relatively easy compare to structure in terahertz and optical region. The conventional fabrication technique listed above, even through offer a good resolution; but they still suffer from high cost and long fabrication time.

In this thesis, the use of a new fabrication technique, namely Microfluidic-jetted technique, for implementing 2D and 3D THz MTMs samples is demonstrated. This technique is basically originated from ink-jet printing technique[68]. The main different between inkjet printing and microfluidic-jetted technique is the size of the nozzles used.

In microfluidic-jetted technique, instead of using large nozzles, 9μm diameter nozzle is used for samples deposition which improved the resolution up to ~10μm. in addition, only one nozzle is used in microfluidic-jetted technique and the drop volume of one drop is approximately 1pL. Thus, a micron size device such like terahertz MTMs is able to fabricated using this technique.

The work reported in this chapter is concerned with investigating microfluidic-jetted technique for fabricating the metamaterials in the terahertz region. Therefore, the understanding of the fabrication system, fabrication steps, formulating of fabricated materials, substrate preparation and resolution of the fabrication is a prerequisite in this work. In addition, factors which affect the fabricated resolution are discussed as well as the advantage and disadvantage of this fabrication technique compared to conventional techniques.

3.4 Comparison of Conventional and Microfludic-jetted Technique

Both microlithography and nanolithography are a complex processes which involve the removal of material. Thus, one may suspect that those methods may not be economical and are wasteful processes due to the onetime use of mask and etching chemicals. Also, many of the materials and chemicals involved may be harmful to the environment. In addition, the multiple procedures are complicated and time consuming. Although the process provides a high resolution fabrication, still, it is common to experience some percentage of failure due to defects in the masking and etching process which may or may not be detected *a-priori*. Microlithography and nanolithography require extremely clean operating conditions. Therefore, an advanced cleanroom chamber is a need for the

process, thus adding to the cost of the fabrication. Also the lithography technique only is restricted to rigid substrate such as quartz, PCB board or silicon wafer. On the contrary, microfluidic-jetted techniques allow the use of broad variety of substrate include paper, polymer even cloth. The advantage of the lithography process especially nanolithography is the relatively high resolution compared to jetting fabrication.

There are many advantages and challenging disadvantages of using microfluidic-jetted technique in device fabrication. The main advantages include high-speed fabrication, low fabrication cost; broad choices of substrates include flexible, flimsy substrate; and less waste for minimized environment impact. On the other hand, the technique also has its limitations, such as poor resolution for micro device fabrication as compare to nanolithography, registration failure and uniformity of the printed layer. The resolution is affected by types of fluidic and types of substrate use. For example using PEDOT: PSS in it optimum jetting would give 18μm resolution while using nanogold in toluene based gives 35μm resolution. The factors causing the listed limitation above and precautionary steps will be discussed later in this chapter. In addition, there is a need for deeper investigation of fluidic properties and performance. Sometimes, for specific device fabrication, preparing the printable fluidic from raw material is needed since there is not much printable fluidic available in the market. Therefore, basic materials chemistry knowledge is a need for using this technique.

3.5 System Description

The Dimatix Materials Printer (DMP) is a laboratory tool that enables ink jetting printing technology for new manufacturing and analytical processes. The DMP is a laboratory and

limited production tool that enables researcher, scientists, and engineers to evaluate the use of ink jetting technology for new manufacturing and analytical processes. It is designed to be convenient and easy to use to carry out "proof of concept" and development work using ink jet technology. The low cost user-fillable piezo-based jetting cartridges can print up to 1 picoliter drop volume from nozzle of size 9μm. Its operation is PC-controlled which also includes visual monitoring of ink jetting and printed pattern inspection. The package software provided by FUJIFILM allows the user to generate a required printed pattern or to import the pattern from other CAD software. Thus, unlike other fabrication techniques, masks are not required. The schematic and its real image are shown in Figure 3.2 Schematic of Dimatix Material Printer (DMP) system and Figure 3.3. It consisted of three main sections, (i) a computer controlled (ii) fabrication module (iii) substrate holder (iv) drop watcher (v) cleaning station and (vi) microfludic module.

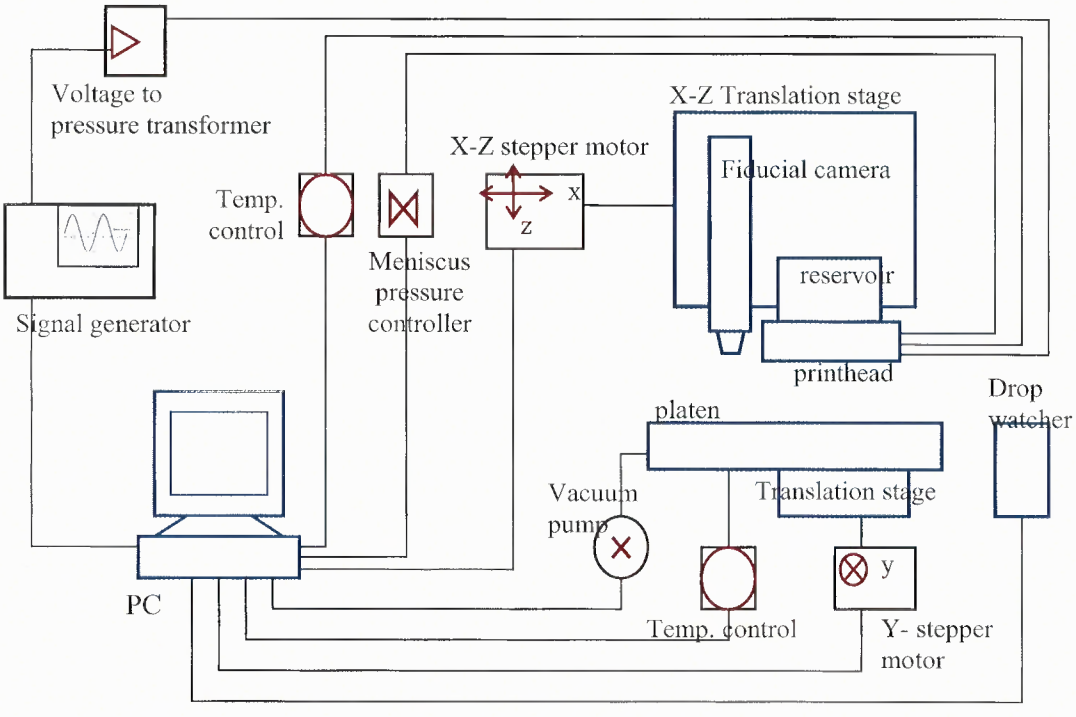

Figure 3.2 Schematic of Dimatix Material Printer (DMP) system.

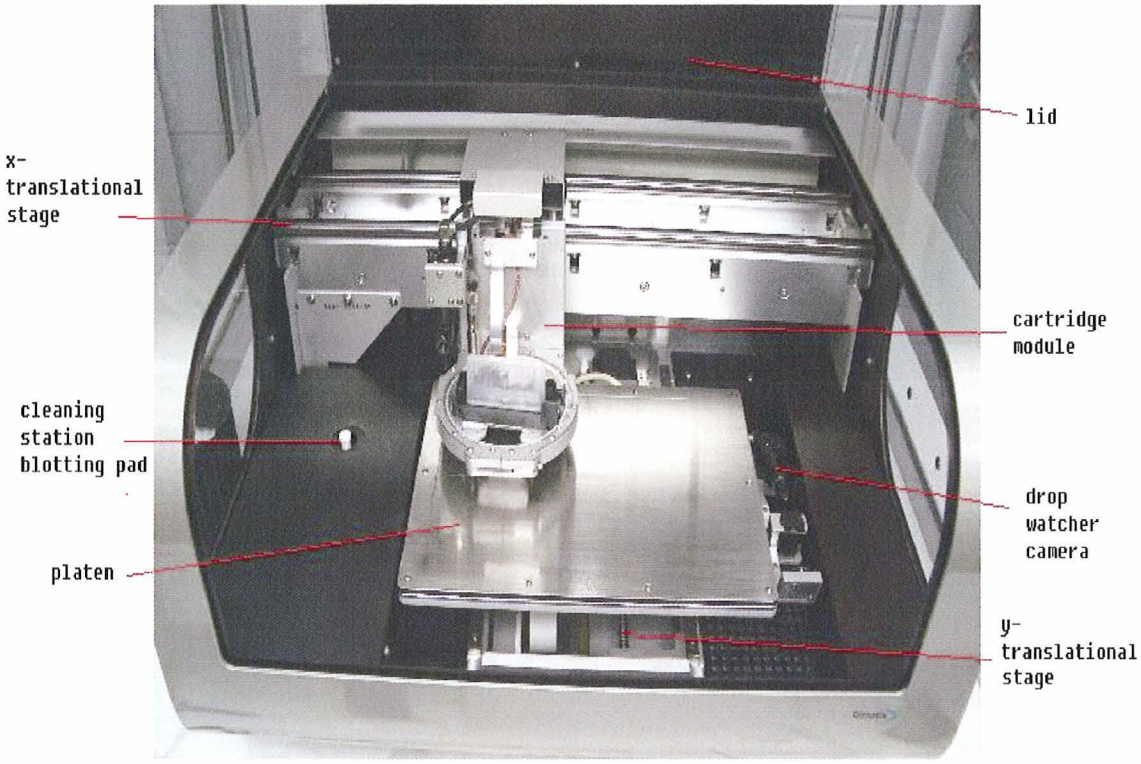

Figure 3.3 Image of Dimatix Materials Printer (DMP).

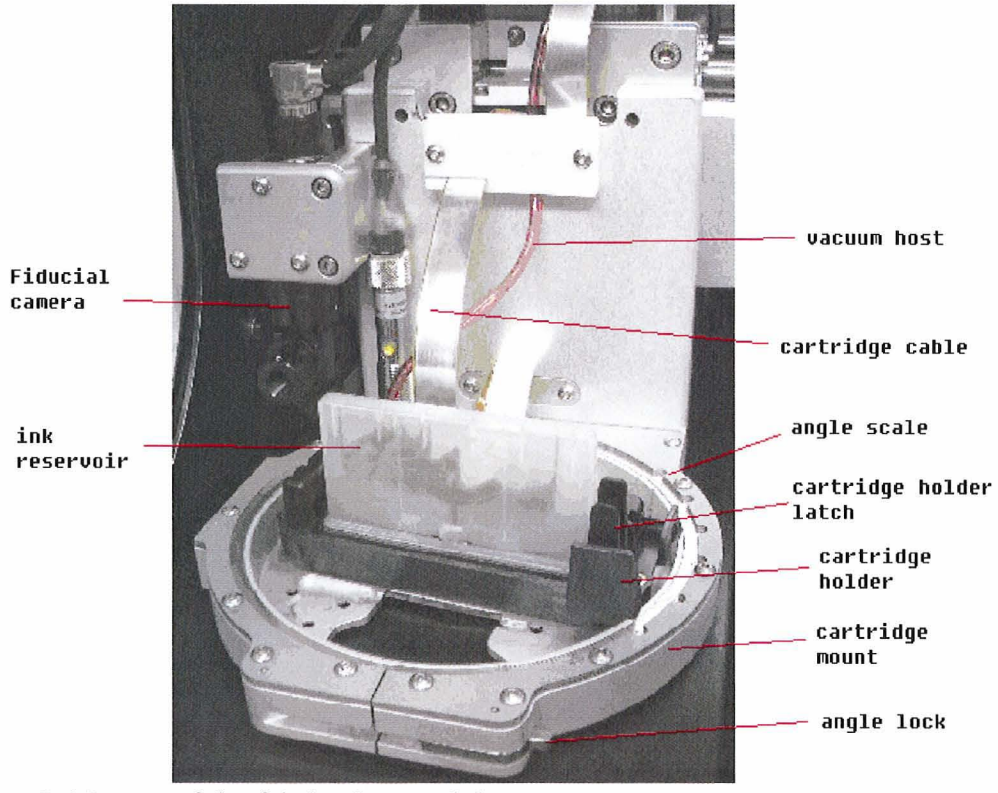

Figure 3.4 Image of the fabrication module.

PC-controlled operation includes visual monitoring of ink jetting and printed pattern inspection. The Computer interface eliminates manually adjustment thus providing precision control for the system. Also, the interface software includes a pattern editor allowing one to create or modify design patterns.

The main parts of the fabrication module consist of cartridge holder, Fiducial camera and cartridge angle adjustment scale. The solid cartridge holder is where the microfludic module is mounted. The cartridge holder connects the piezoelectric transducer of the microfludic module printhead and microelectronics controller. The cartridge angle scale, as shown in Figure 3.4, is set for precise droplet positioning based on the selected drop spacing in use, and it is the only manual adjustment for the system. The detail of angle setting versus drop spacing will presented later in this chapter. In order to align droplets accurately a magnifying optical system was required with the ability to locate surface features and droplet deposits. A Fiducial camera mount beside the cartridge holder allow user to view the fabricated pattern and to position the pattern in the substrate. The two latches are for fasten the cartridge and lock the set cartridge angle. The cartridge cable connects between PC and the microelectronic in the cartridge holder provide fine controlling of PZT diaphragm via the waveform editor. The detail of this matter is discussed later in this chapter. The computer controlled stepper motor drive of the x-stage allows the x position of printed location to be known at any time.

The platen mount on top of y-stage stepper motor with dimensions of 8"×11" provides a large printable area for loading/ unloading of substrate. Combined with the x-stage driven cartridge module, the position of the nozzle location can be precisely

located. The platen is built with 0.5mm diameter vacuum suction holes which are spaced very half inch thus capable to fasten the substrate on the platen.

The drop watcher provides an *in-situ* image of the droplet to check for satellite droplet generation as well as to measure the droplet velocity and size. The drop watcher camera system allows direct viewing of the jetting nozzle and droplets performance. The flight of the ink droplet from the nozzle is captured, in image and movie file, using a stroboscope broad band, white light emitting diode and a charge coupled device camera with 4x magnification. The camera's field view is approximately 1.2 ×1.6 mm with a resolution of 2.5 μm/pixel. A cleaning station with changeable cleaning pad installed ensures the jetting nozzle is in good condition. The cleaning cycle consists of split, purge and blot. By computer control, the sequence, duration and delay of the cleaning cycle is editable by the user based on the specific needs.

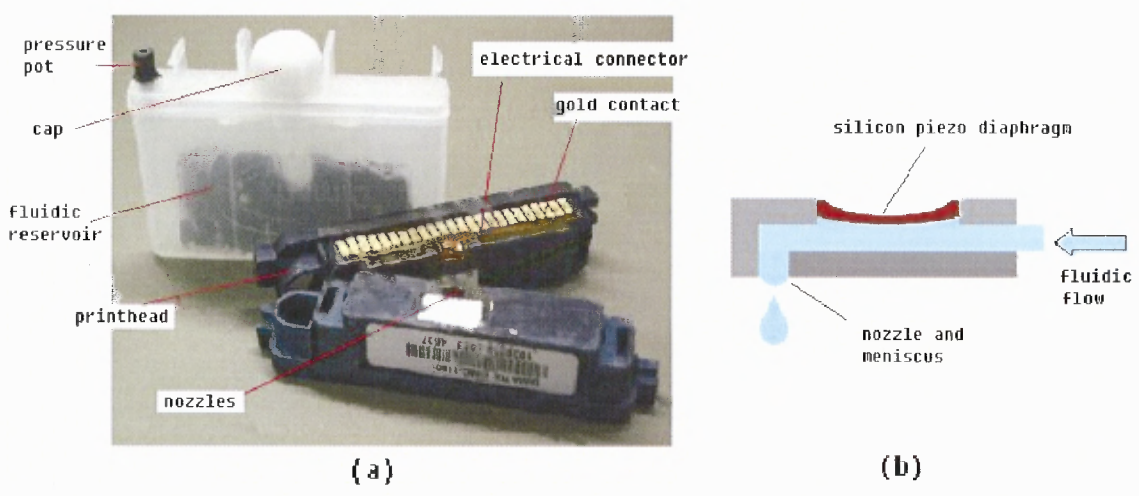

Figure 3.5 Microfluidic module: (a) printhead and reservoir and (b) the enlarged schematic diagram of a piezoelectric transducer bonded to a silicon diaphragm integrated inside printhead.

The microfludic module consists of printhead and 1.5mL microfludic reservoir as shown in Figure 3.5(a). The printhead is integrated with a piezoelectric transducer

bonded to a silicon diaphragm (PZT) [Pb(Zr0.53Ti0.47)O3] (see Figure 3.5(b)) that generates acoustic energy, driving drop formation. The printhead consists of 16 nozzles and electrical connector for PC-interface. The nozzle dimension used in microfluidic-jetted technique is 9μm in diameter and 266.5μm spacing to adjacent nozzles. The number of firing nozzles used can be adjusted according to the user specifications. The deposition time is determined by the number of nozzles used. However, in microfluidic-jetted technique in micron structure fabrication, only one nozzle is used for optimizing the resolution. The electronics pulse or waveform to the piezo electric printhead is maintained for each fluid as optimized for printing sustainability. The pulse potential and duration could be varied until the correct ejection of droplets was obtained. The frequency of the ejection could be varied between approximately 100 Hz to 2.3 kHz. The detail of the waveform setting for optimizing the jetting performance will be discussed later.

3.6 Fabrication Steps

3.6.1 Substrate Chosen and Preparation

Before deposition, the substrate needs to clean of dirt or unwanted particles. The substrate is pre-cleaned with acetone, followed with isopropanol rinses and blew dry with air. It is then boiled with distilled water mix with three drops of cleaning agent D-91 for 60 minutes and followed with 60 minutes ultrasonic bath. Finally, it is rinsed with acetone and isopropanol and air blown to dry. The substrate cleaning is an important fabrication step, particularly for micron features fabrication, because the fabricated resolution is not only determined by drop volume and fluidic properties such as viscosity

and surface tension, but also by the contact of jetting fluid with the substrate. A single particle on the surface of the substrate may affect the surface tension of the fluidic and it tends to smear out to form a large sometimes non-uniform drop shape. The above substrate cleaning is for polyimide or Kapton, quartz and silicon substrates only. While for non-water proof substrate like Photo paper, soft plastic and commercial copper sheet; the printed surface is only necessary to clean with acetone wiping and followed with isopropanol.

3.6.2 Morphology of Deposited Fluidic

The microfluidic fabrication system permits a broad variety of fluids, either mix in the lab or market available printable fluidic, that can be use for fabrication. To achieve optimum jetting performance, some of the fluidic physical characteristics such like viscosity, surface tension, low volatility, density, degassing and filtration must be within certain specifications. Once ideal fluidic properties are met, a specific pulsed voltage applied to nozzles through a requisite user-controlled waveform, would produce ideal spherical droplets regardless of ink composition.

For optimize jetting, the viscosities of the fluidic must in the range of 8 to 15mPa. The viscosity values will affect the intermolecular forces within a drop, producing a dampened velocity thus may cause fault placement of droplet. In addition, the drop may be held inside the nozzle even when high jetting voltage is applied. The viscosity of fluidics can be controlled by mixing with a similar based solvent. Ideally, a viscometer for measuring the viscosity is needed for ease in carry out the fluidic formulation. However, without a viscometer, a trial and error method maybe used to determine the ideal jetting performance.

Ideal surface tension for optimize jetting is around 28 dyne/cm. Surface tension is obviously varies for different fluidics due to their different solvent base. For example, water based fluidics have a high surface tension compared with toluene based fluidics. Thus water based fluidic is very often formulated with alcoholic co-solvents and/or surfactants in order to lower surface tension for optimized jetting performance.

Different fluidics will have different output response even though the viscosity and surface tension are the same. A study[69] is carried out for three different jetting fluidic with similar viscosities and surface tensions. The studied showed that all the fluidics have different jetting profiles. This is perhaps due to the density of the different material.

Low volatility or stable fluidic is necessary to avoid possibility of any hazardous damage to the fabrication system. Degassing and filtration are precaution steps to eliminate the occurrence of gas bubbles or agglomeration of the fluidic.

Three different materials used for the fabrication of metamaterials: (a) toluene based functionalized-nanogold[70] purchase from Sigma-Aldrich, (b) conductive polymer, PEDOT: PSS[71] from H. C. Starck and (c) liquid polyimide from HD MicroSystem in conjunction with Pyralux substrate (copper clad Kapton HN).

(a) H_2O based PEDOT:PSS. The first fluidic used in the metamaterial fabrication was commercially available water based PEDOT: PSS also called Baytron P produced by H.C. Starck. PEDOT (Poly(3,4-ethylenedioxythiophene)) is a polythiophene developed at Bayer AG in 1988[72]. It was found in 1991 that PEDOT could be doped with PSS (poly(styrenesulfonate)). PSS is water soluble and dopes the PEDOT during polymerisation by acting as a counter ion to the polythiophene chain resulting in a soluble conducting polymer[73]. Thus, PEDOT: PSS is a polymer mixture of two ionomers (see

Figure 3.6) made up of poly(3,4-ethylenedioxythiophene) or PEDOT and sodium polystyrene sulfonate which is a sulfonated polystyrene. Part of the sulfonyl groups are deprotonated and carry a negative charge. PEDOT is a conjugated polymer and carries positive charges and is based on polythiophene. Water soluble PEDOT: PSS marketed commercially as Baytron P which fulfilled the requirement for ease of fabrication. It forms good films while at the same time retaining its optical transparency and high chemical stability.

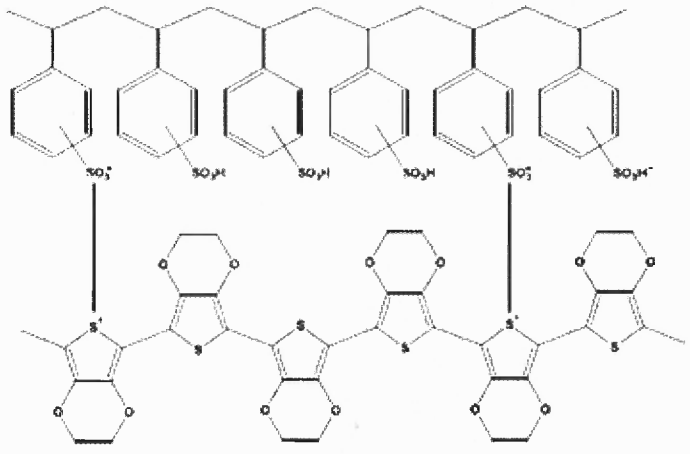

Figure 3.6 Chemical structure of PEDOT doped with PSS[71].

Now, PEDOT: PSS are also soluble in other solvents such like xylene, chloroform and isopropanol. But the water based PEDOT: PSS provides the best fabrication result in reducing the droplet size to ~18μm due to its relatively high surface tension compare to other solvents. Any inkjet print system, as well as microfluidic-jetted system, should be able to deposit single droplets of such solutions reliably. That is why PEDOT:PSS has been used in many applications, such as polymer light emitting diodes (PLEDs)[74], organic transistors[75], smart windows, electronic paper, antistatic coating, sensors, batteries, solar cells, and others[76, 77].

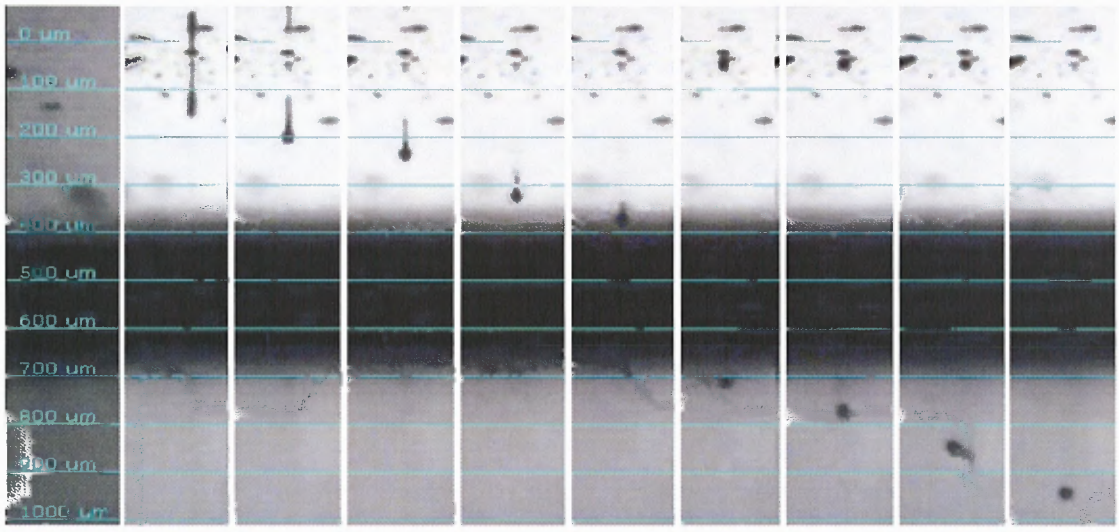

Figure 3.7 Time of flight of PEDOT: PSS droplet jetting. Image taken by system built in drop watcher camera.

(b) Dodecanethiol Functionalized Nanogold. Dodecanethiol functionalized nanogold (DDT-AuNPs)[78,79] with particle size of 2 to 4nm purchased form Sigma-Aldrich has resistivity as low as 10^{-7} Ω-cm which is 4x lower then the resistivity of the bulk gold[80].

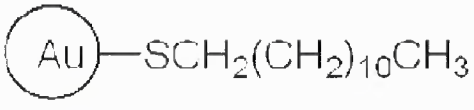

Figure 3.8 The structure of Dodecanethiol functionalized gold nanoparticles solution. Dodecanethiol is the polymer attach to the Au nanoparticle.

Figure 3.8 shows the Dodecanethiol functionalized gold nanoparticles solution. The interest part of this solution is the protecting dodecanethiol (HS(CH2)nX) monolayer. A typical dodecanethiol, allows properties such as chain length (denoted by n) and the chemical identity of the terminal functionality (denoted by X) to be modified either through the choice of the dodecanethiol, through ligand exchange (where one dodecanethiol replaces another) or through chemical modification by reaction with an

appropriate terminal group on the dodecanethiol. The dodecanethiol layer also provides stability and isolates the nanoparticle and allowing them to be re-suspended.

The DDT-AuNPs SRR and microstrips were created on a polyimide substrate by the generation of microdroplets using microfluidic-jetted technique which 9μm nozzle size was used. The toluene based nanogold has small viscosity and low surface tension, to prevent it from leaking from the nozzle. A low voltage amplitude of 13 to 15V and meniscus vacuum of 4.5 inchesH_2O was applied to jetting the fluid. The waveform setting will be discussed later. Since nanoparticles melt at low temperatures, there is great potential for producing the samples at low processing temperature suitable for polymeric substrate that is not stable for high temperature. An *in situ* "frozen" image of the droplet is capture as shown in Figure 3.9.

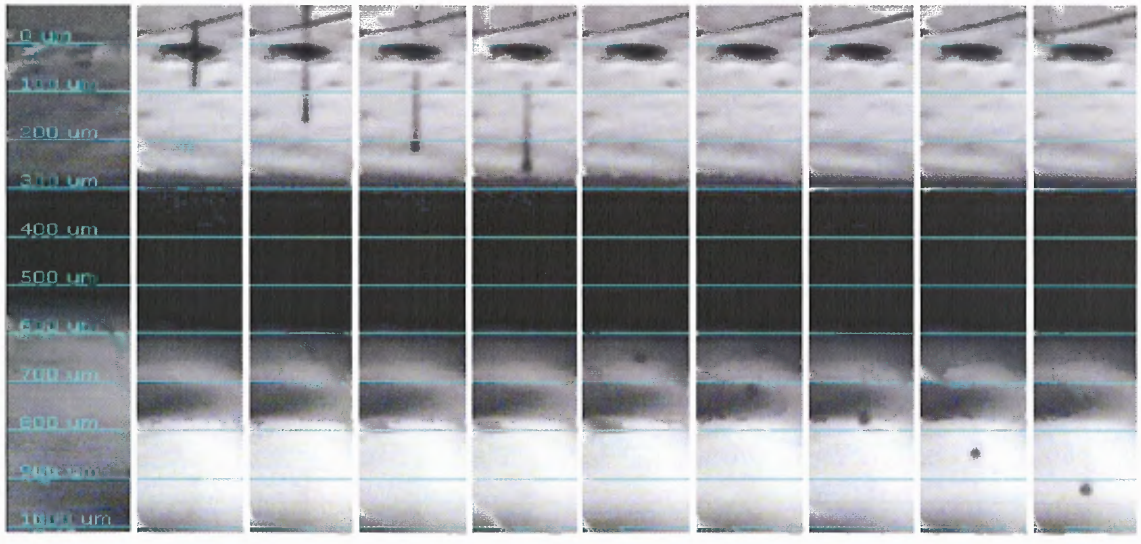

Figure 3.9 Time of flight images of single droplet DDT-AuNPs deposition. The relative long "tailing" effect compare to PEDOT: PSS was due to its low surface tension and viscosity.

(c) Liquid polyimide. In fabricating one of the sample in this thesis, liquid polyimide is used as a printed mask deposited on top of a conventional copper sheet. Liquid polyimide is purchased from HD MicroSystem®. This fluidic are supplied as

solution suitable for coating application. It can be coat into variety of metal and is inert to etchant, thus suitable to use as masking material in this dissertation work for fabrication of copper samples.

3.6.3 Design Layout

In order to deposit the desired structure, the design pattern must first be transferred and loaded to the DMP system for printing. The fabrication structure is designed in the DMP software package bitmap editor. The editor allows the user to select a desired grid spacing between 5 to 266.5μm. The Bitmap sample layouts are shown in Figure 3.10 where in this design; a grid spacing of 5μm and 10μm are used for 80μm SRR and 180μm structures. A grid spacing of 5μm, meaning that a drop can be place as close as 5μm to an adjacent drop, adds more flexibility for pattern design.

There were three types of drop spacing setting in the 80μm SRR design: 15μm for the upper 4 drops, 15μm for the sides and 5μm at the gap (see Figure 3.10 (a)). Drop spacing is important factor in optimizing the resolution of the fabrication. For too narrow drop spacing relative to its drop size, the fluidic is considered too dense and will spread out to form a blurred structure. If the drop spacing is too broad, a gap between droplets will form. Thus, the chosen drop spacing must be close to the individual droplet size. For example, the droplet size of PEDOT: PSS is ~18μm, so the ideal drop spacing is 15 to 20μm. And for the nanogold, the droplet size is ~35μm, so the chosen drop spacing is 30 to 40μm.

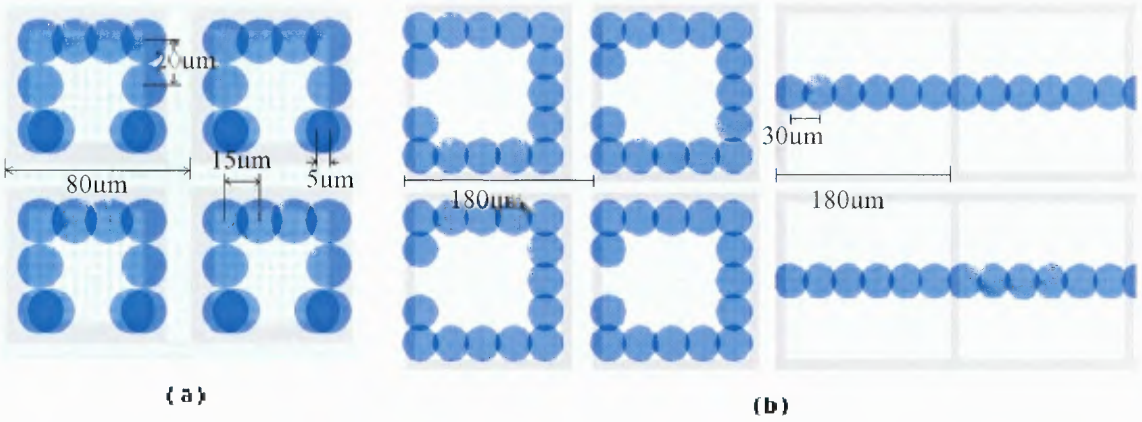

Figure 3.10 Shows the image of Bitmap layout of (a) 80μm lattice size SRR for PEDOT: PSS fluidic used. The grid spacing used is 5μm and the blue dot diameter is 20μm. And, (b) LHM with lattice size of 180μm (both SRR and rod) for DDT-AuNPs . The grid spacing is 10μm, drop spacing is 30μm and blue dot diameter is 35μm.

When the deposited pattern is designed in Bitmap editor, the selected grid spacing must compatible with the structure lattice size. Incorrect drop spacing relative to lattice size will cause the drop misplace in the array. Figure 3.12 shows the 15 grid spacing used for lattice size of 75μm, 80μm and 90μm. The drop was shifted in every third row. The correct grid spacing used must be factor of the lattice size.

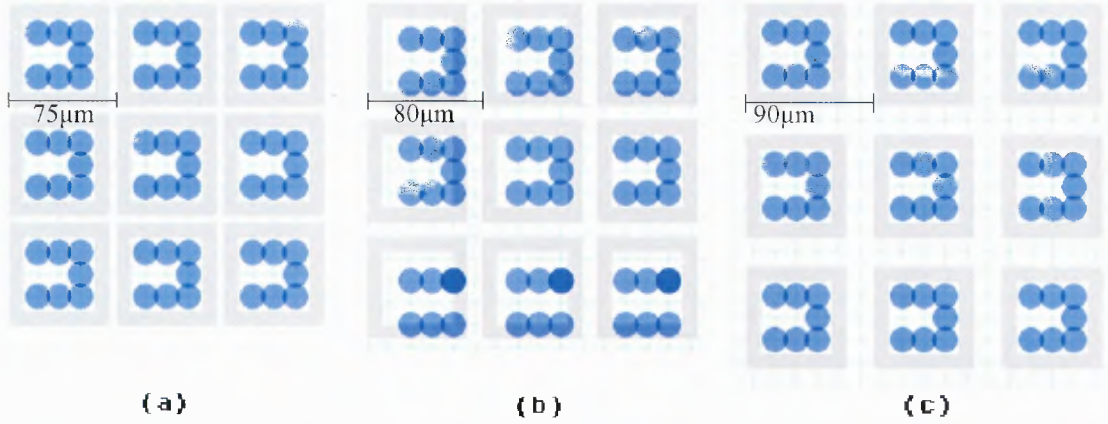

Figure 3.11 Bitmap layout of grid spacing of 15μm (a) 75μm (b) 80μm and (c) 90μm lattice size SRR. Since 80 is not factor of 15, thus the image on (b) is the wrong lattice size which causes the middle drop to be shifted in the third row array.

Before the pattern is loaded for printing, the X-start and Y-start must be carefully set. X-start and Y-start is the position relative to the printing origin where the first drop

place is to be placed. The X-start and Y-start selected must be compatible with the drop spacing. For example, if 15μm drop spacing is used, the first drop must start at position of n×15μm where n is discrete number. Figure 3.12 shows a misplaced pattern when incorrect position is used for X- and Y- start.

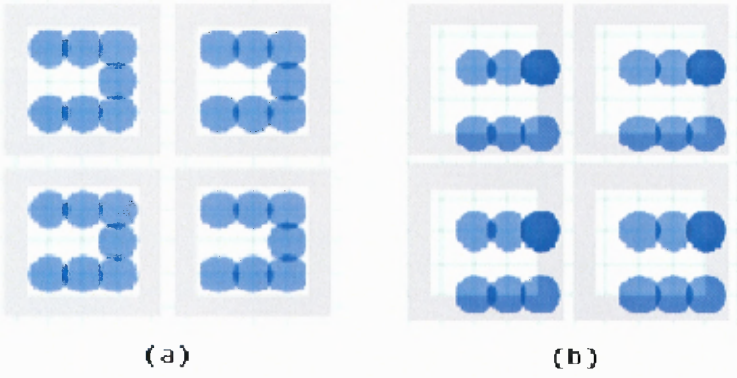

Figure 3.12 Pattern with (a) correct X- and Y- starting point and (b) drop misplace due to incorrect position of X- and Y- start on every arrays.

3.6.4 Cartridge Setting

The cartridge settings tab windows is the portion of the DMP control software where the jetting waveform, firing voltage, number of nozzle, nozzles temperature, print height, meniscus of drop near the nozzle, jetting frequency and cleaning cycle is set before deposition. In microfluidic deposition, only one out of 16 nozzles is used because micron size features require deposition drop by drop. Using more then one nozzle will cause multiple drops to group together forming a larger drop. Thus, it is difficult to achieve a minimally sized structure. The print height which can vary between 0.25 to 1.5mm is the distance between nozzle and substrate. For sample fabrication in this thesis, a print height of 0.5 to 0.6mm is used. The chosen print height is critical to fabrication resolution that will discuss in the following section in this chapter.

The DMP operates under negative pressure to keep the meniscus at the edge of the nozzle. This meniscus pressure is adjusted in scale from 1 to 5 inches H_2O depending on the viscosity and surface tension of the fluid. For example, meniscus pressure for PEDOT: PSS, DDT-AuNPs and liquid polyimide was set to 1-2, 4-4.5 and 3 inches H_2O, respectively. Having incorrect settings will cause excess fluidic jetting or difficulty in jetting. The effect might not be significant for certain fluidic such as PEDOT: PSS since it has relatively high surface tension due to its water based solvent. However, for certain fluidic like DDT-AuNPs, a small change of the meniscus pressure will cause huge effect on the jetting performance.

Nozzle temperature is adjusted due to the viscosity of the fluidic used. Increasing the nozzle temperature may cause the solvent to evaporate thus increase the viscosity of the fluidic. For toluene based nanogold deposition, the viscosity is low, therefore, a nozzle temperature of 29-33°C is applied to get the desired jetting performance. PEDOT: PSS has perfect viscosity thus 28°C nozzle temperature is set. If platen heat is applied while printing, heat from platen may transfer to printhead thus increase the temperature of the nozzle. However, by setting the nozzle temperature to specific value, once the temperature deviates from that value, a DMP printer message will notify the user of the temperature deviation and tune back to the selected temperature before printing.

In sample fabrication here, the cleaning cycle and idle setting for deposition was set as shown in Table 3.1. This cleaning cycle can be applied when the system starts or/ and at the end of jetting. The idle setting is the task done while the printhead is at rest to keep the nozzle "alive". The cleaning cycle can be varied depending on the situation. For example, longer spit time is used for miscellaneous nozzle clogging.

Table 3.1 Cleaning Cycle and Idle Setting for Microfluidic Deposition

	Task	time	frequency	delay
Cleaning cycle	Spit	100-200ms	2kHz	1s
	Purge	2-4s	-	1s
	Spit	300-500ms	2kHz	1s
	blot	1-2s	-	-
Idle	Spit	100ms	1.5kHz	2s

3.6.5 Waveform Setting

One of the issues involved in deposition is the square waveform used to drive the piezoelectric transducer which in turn generates pressure for ejection of each single droplet. Each individual fluidic require its own unit waveform setting. Also, the new waveform has to be reformed when switching from 21μm to 9μm nozzle even though the same fluidic is used.

Waveform setting is divided into four phases. Phase 1 is the beginning of the firing action where the fluid is pulled into the reservoir through the inlet. Phase 2 is a drop ejection phase where the reservoir is compressed and pressure is generated to eject a drop. Phase 3 is the recovery phase where the piezo voltage is brought back down and the reservoir decompresses partially refilling in preparation for the next pulse. Final phase 4 reverts the diaphragm back to its natural or relaxing position. Each segment has three properties: duration, amplitude and slew rate. The applied amplitude (voltage) and slew rate are related to how far and how fast the silicon piezo diaphragm is bent. The duration controls how long the silicon piezo diaphragm is maintained in that position. The amplitude (voltage) and the first two phases have the most impact on the jetting process. Changing the properties in these two phases will significantly effect drop formation. Figure 3.13 (a), (b) and (c) show the waveform setting of PEDOT: PSS, DDT-AuNPs and liquid polyimide solution, respectively.

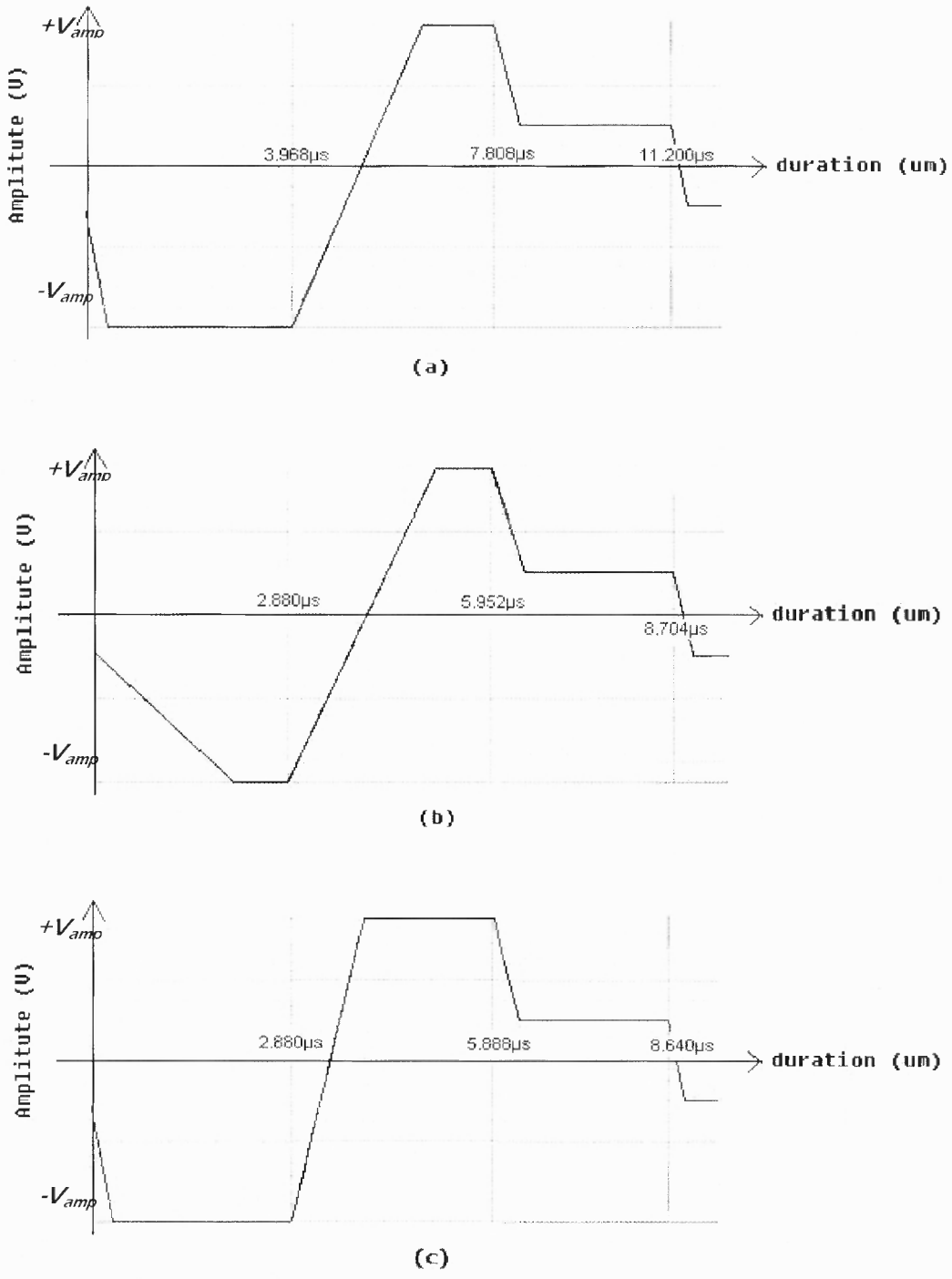

Figure 3.13 Waveform setting of (a) PEDOT: PSS, (b) DDT-AuNPs solution, (c) Liquid polyimide. V_{amp} for PEDOT: PSS was 11-13V, DDT-AuNPs was 15-17V and liquid polyimide was 19-21V.

3.6.6 Curing

The DDT-AuNPs solution contains 98% of toluene leaving only 2% weight per volume Nanogold deposited on polyimide substrate. For obtaining a highly conductive gold line, the deposited structure is cured with heat. When heating with temperature 60-90°C, the dodecanethiol tail is evaporated and the nanoparticle tend to move close to each other. While heating with 100 to 120°C, a uniform layer of nanoparticle film is formed[80].

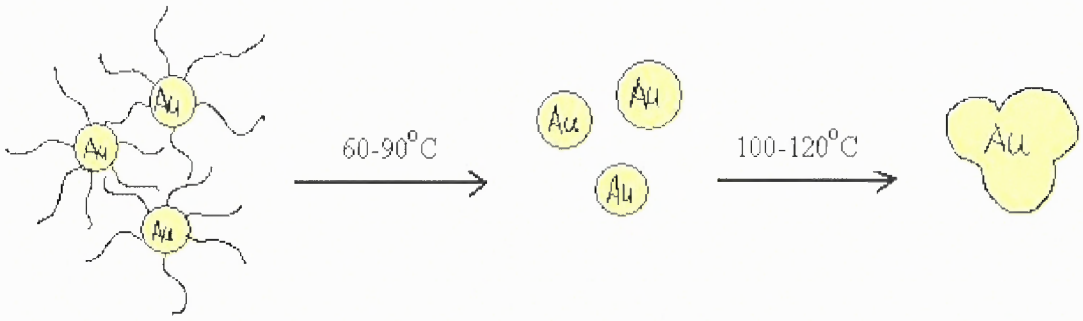

Figure 3.14 Individual nanogold atom surround by Dodecanethiol ligands can be further cure to form high conducting film at low temperature. By Nanomas technology, Inc.

When depositing materials on a heated platen, the solvent evaporates soon after contact with substrate. The rapid solvent evaporation also eliminated humidity problems in the fabrication environment, such as uneven wetting in response to contamination of the samples. However, there are limitations in deposition on a heated substrate. Since the gap between nozzles and substrate is very small (~0.6mm), this causes heat transfer and a rise in the temperature in the nozzle. Thus, this consequently decreases both the viscosity and surface tension of fluid and sometimes the fluidic dry and clog the nozzles due to the solvent evaporate in the nozzle. The platen temperature is set to 30-35°C while printing and allowing it for 20-30 minutes to dry before next layer is printed.

3.7 Print Quality Control and Troubleshooting

In microfluidic-jetted fabrication, reducing the dimensions of the deposited structures is the overall aim of the investigation; the deposited droplets would have to be relatively small. Reduction in drop size is a major topic in improving the resolution or precision of microfluidic-jetted technique. The resolution was limited to 18μm, 25μm and 30μm for PEDOT: PSS, liquid polyimide and DDT-AuNPs, respectively. Thus quality control and troubleshooting such as drop placement accuracy, alignment and overall jetting uniformity are necessary to study in order to improve quality and to allow the technology to expand into high resolution terahertz MTMs fabrication. A high rate of droplet generation was not required in here. More important was the ability to deposit single droplets on demand.

3.7.1 Droplet Ejection Accuracy

The accuracy to which a droplet can be placed on a substrate is dependant on several factors include jetting straightness and printhead-to-stage alignment. When the piezoelectric actuator generates a pressure in the ink within the print nozzle, the ink is driven out of the nozzle, forming a single droplet. This droplet then falls to impact with the substrate. The critical issue involved is the deviation of droplet placement on the substrate is due to the misdirected or unstraightness of droplet jetting.

Misdirected drop refers to drops that are traveling off the straight axis forming a deviated angle from axis. Figure 3.15 shows an image of a jetting droplet that is off axis captured using the drop watcher camera. Misdirected droplets may due to several issues: the primary causes are contamination on the nozzle plate and imperfectness or damage of nozzle. Contamination refers to debris or air bubbles that form near the nozzle that

partially clogs of the nozzle and force the drop to eject at a deviated angle. Figure 3.16 shows the images captured by built-in Fiducial camera, as well as the deposited result of misdirected droplets (Figure 3.16 (a)) compare to perfect jetting result (Figure 3.16 (b)).

To avoid the misdirect jetting, the cleaning process is set for the nozzle so that it splits to remove any agglomerated particles that block the nozzles and blot in the clean pad. Micro filters of 0.2-0.45μm are used before filling the reservoir with ink to ensure the agglomerated particle and air bubble is filtered. Ultrasonic is an essential procedure to remove the agglomerated particle and micro-bubbles before the microfluidic is used for deposition.

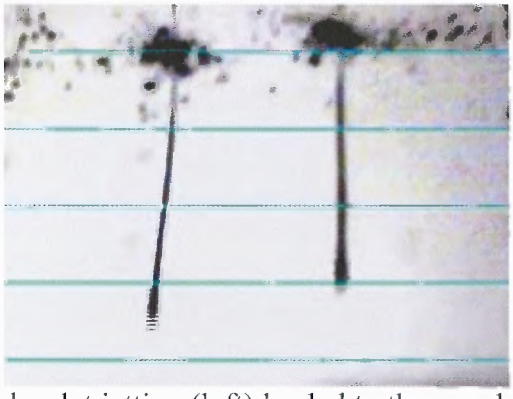

Figure 3.15 The bended droplet jetting (left) leaded to the angular deviation of droplet placement and the straight droplet jetting (right).

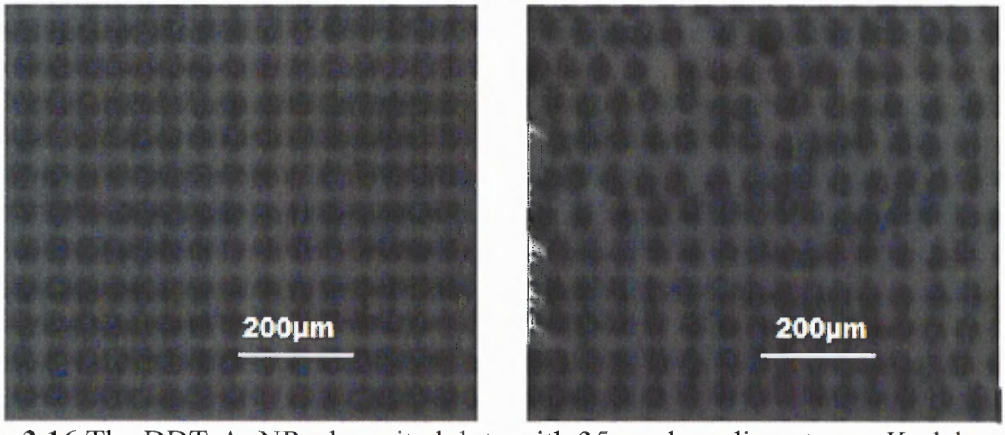

Figure 3.16 The DDT-AuNPs deposited dots with 35μm drop diameter on Kodak EasyShare photo paper. Sample printed with (a) straight jetting droplet (b) unstraight jetting droplet.

Imperfections of the nozzle due to its manufacture, similar to the nozzle contamination, will misdirect the droplets to form and cause angular deviation. Figure 3.17 shows a "Kirk" in the side of the nozzle which affects the jetting straightness. Replacement of the nozzle is necessary for this issue. The other reason is due to the solvents or fluidic used that may corrode the nozzle. For example, a polystyrene sulfonic acid (PSS) of Baytron P (PEDOT: PSS) has a pH value 1.5 and could corrode metallic components potentially destroying the printhead, thus causing the unstraightness of droplet jetting. Figure 3.17 shows the etched nozzle by PEDOT: PSS. To solve this issue, an alternate material such as silicon[81] is used to replace the nickel plate nozzle.

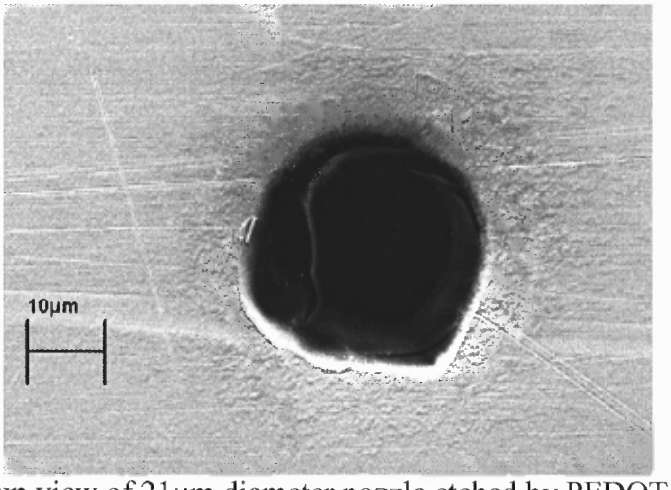

Figure 3.17 Close up view of 21μm diameter nozzle etched by PEDOT: PSS[82].

Reduction of the distance between the nozzle and substrate may minimize the drop placement error caused by a misdirect droplet. Figure 3.19 illustrated the deviation angle, θ, of droplet due to the misdirected jetting and formation of a placement error, $e_{drop\_placement}$, on substrate. The relation of drop placement error, print height, h and deviation angle from axis is

$$e_{drop\_placement} = \frac{h}{\cos\theta} \tag{3.1}$$

Since drop placement error is proportional to the print height, the reduction of nozzle to substrate position will reduce the drop placement error. However, the minimum print height that can reach in sample fabrication here is 0.45mm. Print height smaller then 0.45mm may cause scratching of the deposited sample by the printhead.

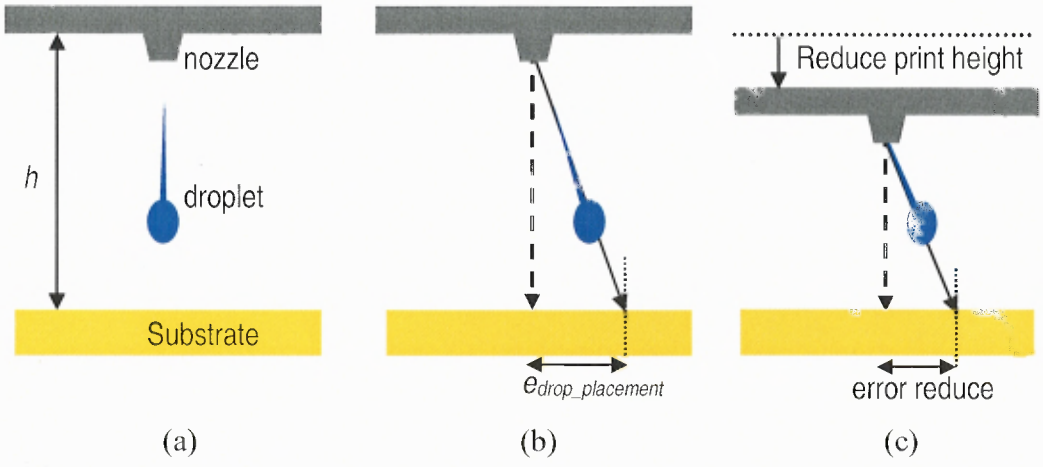

Figure 3.18 The jetting droplet from a nozzle (a) perfectly straight, (b) drop displacement error due to deviation of the jetting and (c) reduction of the displacement error by reducing the print height.

3.7.2 Cartridge Alignment

Machine and staging error may also contribute to the drop placement error. Therefore, proper alignment is needed before the deposition. Alignment of the print cartridge is the most often missed contributor to print quality. This is because DMP software relies on the user to manually rotate the angle of the printhead to match the drop spacing used in deposition. Failure to adjust this angle accurately will result in gaps between drops or overlapping of drops as shown in Figure 3.19.

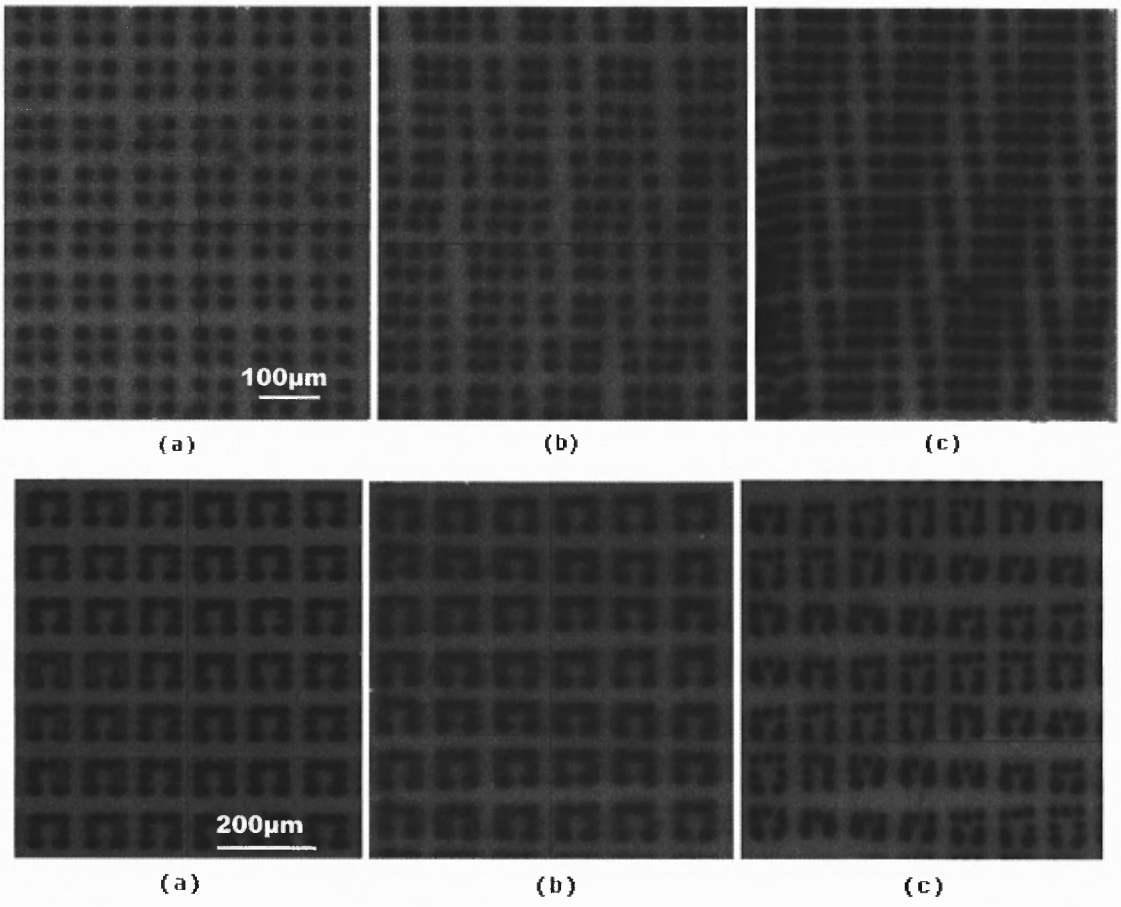

Figure 3.19 Image taken by built-in Fudicial camera shows the placement error of 4 Dots (upper) and 140µm SRR (bottom) due to the incorrect cartridge angle setting. Image with (a) correct angle (b) angle deviated of (b) ~0.5° and (c) ~1° from the correct angle is shown.

Sometime, the staging error may occur due to the mechanical stepping motor fail to send the stage back to its zero position. This caused the failure of the second deposited layer to be placed on top of the first layer as shown in sample of Figure 3.20. In order to ensure that the second layer is aligned to the first layer, with the substrate never removed from the platen, drop offset routine will need to be run. Thus, droplets can be accurately aligned with respect to each other with no optical system required. If the substrate is moved with respect to the stage then a marker is needed for the aligning purpose.

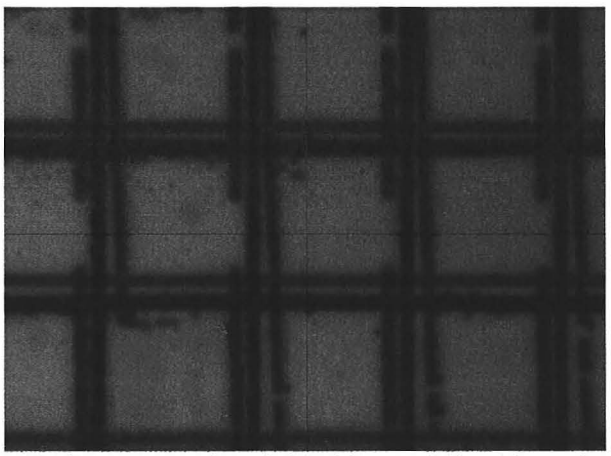

Figure 3.20 Sample with first, second and third layer fail to deposit on top of each other due to the staging error.

3.7.3 Angle Calibration

The difference between the microfludic-jetted technique from the typical ink-jetted technique is the use of 9μm instead of 21.5μm nozzle diameter. To switch from this 9μm nozzle diameter, the angle of the cartridge due to the selected grid spacing needs to be recalibrated. Figure 3.21(a) illustrated the nozzles in 21.5μm (red circle) and 9μm (blue circle) diameter. The nozzle spacing between the 21.5μm is 254μm whereas for the 9μm nozzle, the spacing is 266.5μm. When the cartridge tilted, the nozzles are also tilted in the same amount since they are parallel to each other. Figure 3.23 (b) shows the orientation of tilted cartridge angle θ and grid spacing d. where θ is obtain from simple trigonometry calculation,

$$\cos\theta = \frac{d}{S_N} \tag{3.2}$$

where S_N is nozzle spacing. Figure 3.22 showed the plot of cartridge angle setting due to selected grip spacing for 21.5μm and 9μm nozzle.

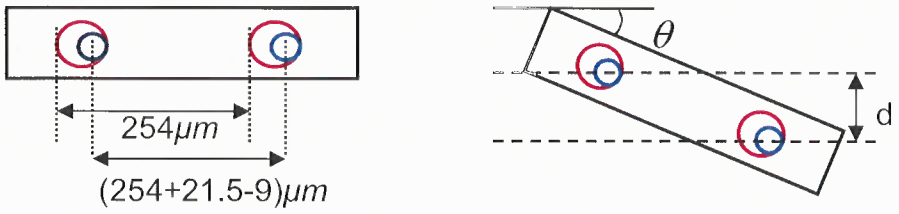

(a) (b)

Figure 3.21 Diagram of nozzle (a) red circle indicate 21.5μm nozzle with 254μm spacing and blue circle is 9μm nozzle with (254+21.5-9)μm spacing. (b) Cartridge angle tilted to provide drop spacing accuracy.

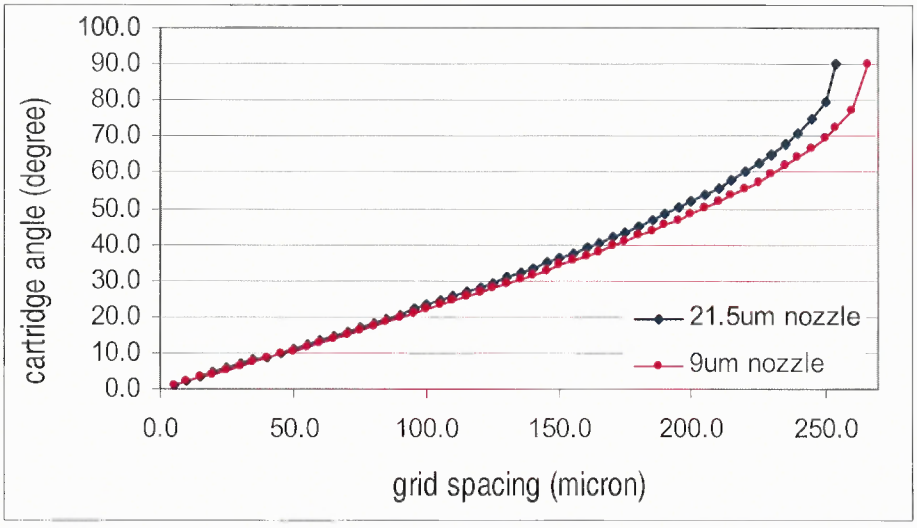

Figure 3.22 Plot for calculated cartridge setting angle versus deposited drop spacing for 21.5μm and 9μm nozzle size.

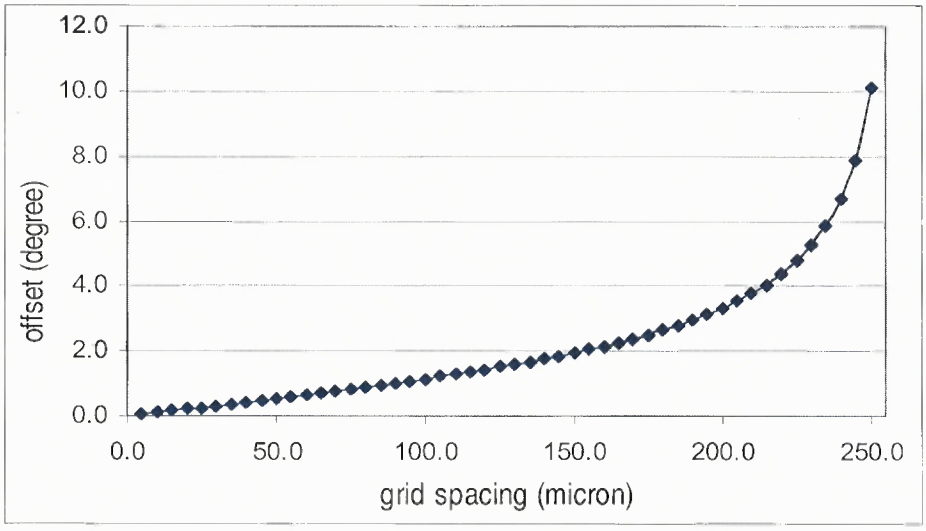

Figure 3.23 The plot of offset which is the angular difference between the 21.5μm and 9μm nozzles. It is increases for larger grid spacing.

3.7.4 Distance between Nozzles and Substrate

When the droplet is jetted from the nozzle, it falls through a distance, *h*, before hitting the surface of the substrate. The impact of the droplet on the substrate is proportional to the distance, *h*. since this impact is directly related to the size of deposited droplet, thus it effects the deposition resolution. Figure 3.24 showed the drop diameter as a function of printing gap between nozzles and substrate. This data is taken from PEDOT: PSS deposition using 21μm nozzle diameter. The same trend would be expected if the 9μm nozzle were used. The drop deposited below a print height of 0.4mm was unable to be defined because the nozzle was too closed to the substrate and damage the sample. For the print height above 1.2mm, the drop diameter saturated because the minimum drop volume has formed. In addition, as mention in Subsection 3.7.1, the reduction of print height will also reduce the placement error.

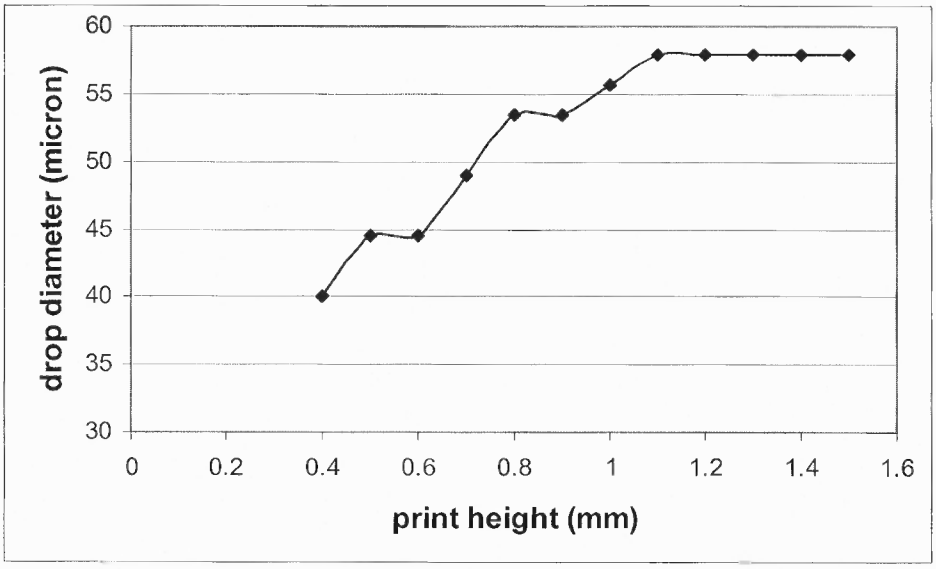

Figure 3.24 Drop diameter versus distance between nozzle and substrate. Data obtained from PEDOT: PSS deposition using 21μm nozzle diameter.

3.7.5 Jetting Condition Variation due to Substrate Heating

When the substrate is heated during deposition, the jetting velocity changes due to heat transfer from the heated substrate to the printhead thus raise the temperature of the nozzle and fluid nearby the nozzle. This temperature rise causes the solvent of the fluidic to evaporate and thus increases the viscosity and surface tension of the fluid near the nozzle. Since the velocity is inversely proportional to the viscosity and surface tension, the ejecting droplet velocity decreases dramatically.

In the case of toluene based fluidic such as DDT-AuNPs, a small raise in temperature would significantly affect the viscosity and surface tension due to the low evaporation temperature of the toluene. Study has elaborated that the 50°C temperature rise from room temperature decreases the viscosity and surface tension by approximately 40% and 10%, respectively, while the ejecting velocity increases about 3-5 times[83]. The increment in the gap distance between the nozzle and the substrate will minimize the rise of temperature at the nozzle. However, the impact velocity of the droplet also decreases and good control on droplet placement cannot be guaranteed, as discuss in Subsection 3.7.1 and 3.7.4.

3.7.6 Incorrect Waveform

When firing a droplet, the drop train tends to break up before it completely leaves the nozzle and form a meniscus of wetted ink over the face of the nozzle. This is because of the pressure applied to the piezo transducer not having enough energy to push the fluid completely out of the nozzle. This leaves the bulk of the ink within the nozzle and effect the jetting performance of next drop. Another problem is the tail of the droplet breaking up, forming a secondary satellite droplet as shown in Figure 3.25 (b). This satellite then

travels in a slightly different direction and speed which is undesirable for the microfludic-jetting technique. Figure 3.25 (c) showed the Fiducial image of the deposition result from the split droplet. The satellite form a secondary small dot next the main drop. To eliminate the satellite, careful manipulation of the jetting waveforms allows satellite droplets to catch up with the main droplet and be reabsorbed to form a single droplet.

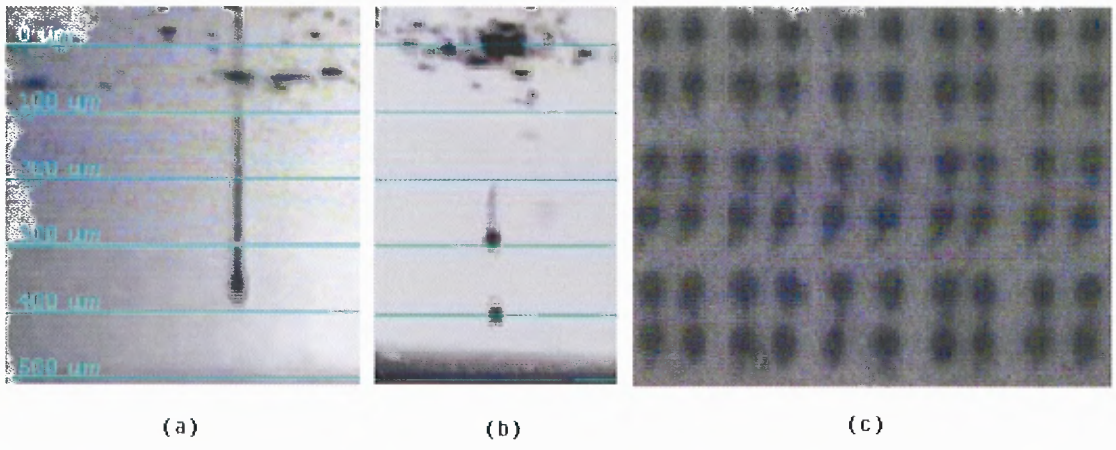

Figure 3.25 Image taken by built-in camera of the deposition system shows the droplet with (a) perfect drop and (b) split of droplet due to the incorrect waveform setting. (c) Image of the deposition result from the split droplet which a secondary small dot is formed next to the main drop.

3.7.7 Non-firing Nozzles

A non-firing nozzle is a nozzle that does not eject a drop under any condition while other adjacent nozzles are firing properly. There are usually only two causes. The first reason is the fluidic dried out near the nozzle and block the fluidic from jetting. The second reason is that the occurrence of debris or air bubble that entirely blocks the nozzle. A fresh cleaning pad is critical to the head performance. If pulsations of the meniscus are observed under drop watcher, then there is a trapped bubble inside the nozzle. To remove the trapped bubble, a purge cycle of 0.5-1.0s may help. If there are no visible pulsations of the meniscus then the nozzle is likely plugged or fluid has not reached the nozzles.

Applying an appropriate solvent to the nozzle plate may dissolve dried jetting fluid. If the nozzle has clogged with foreign debris then the advanced features of the "Cartridge Settings" will be needed.

Another issue is the drying of the ink solvent in the nozzle of the printhead when the jetting work is stopped for certain amount of time. To avoid this, the tickle mode is set in term of frequency for exercising the pumping chamber at low amplitude to rhythmically pulsates the nozzle exit meniscus to keep the nozzle wet. This may be sufficient to keep nozzles "alive" for lower volatility fluids as an alternative to spitting. Other alternative way is set the nozzle to "breath" at its end of printing state. For example the nozzle is set to split for 0.5s in every 2s during its rest time.

Another reason of nozzle clogging is due to high nozzles temperature that cause solvent evaporates leaving the particle to clog the nozzle. In addition, printing and heating the sample at the same time may also cause nozzles to be clogged, since the heat is transferred from platen to the printhead. Therefore, a low temperature is used for curing the sample while printing or curing the sample after printing is an appropriate precaution.

3.7.8 Other Effects

Humidity is a serious issue for microfluidic deposition. The solvent of the fluidic may absorb water vapor near the nozzle. Excessive water will add to the drop and change the viscosity and surface tension thus affect the jetting performance. This problem usually occurs during summer. A dehumidifier is used to solve this problem.

The choice of solvent and substrate are also affect the deposition resolution. As mention in previous section, water based fluidic possess high surface tension thus

forming a small curvature droplet that reduces the diameter of droplet. Toluene based fluidics have low surface tension that tend to smear out and form the larger droplet. The same approach applied to the influence of substrate on drop spread is illustrated in Figure 3.26. Polyimide has extremely smooth and high surface energy that force the droplet to form its maximum surface tension that holds maximum curvature.

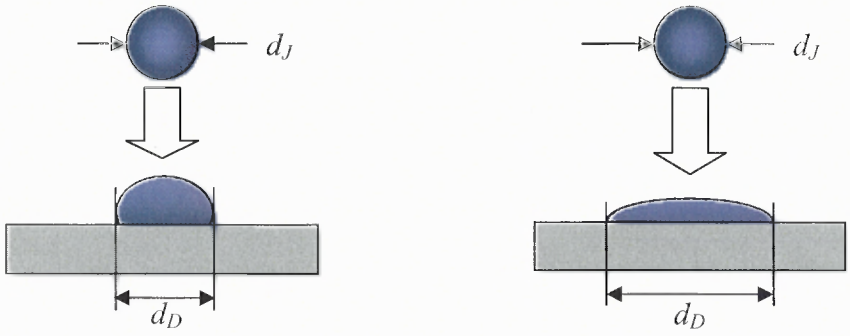

(a) (b)

Figure 3.26 Illustrate of the influence of surface tension of the fluidic used to deposit on the substrate. The fluidic used on (a) is PEDOT: PSS and (b) is DDT-AuNPs which have larger deposited drop diameter d_D.

In addition, the surface of substrate is required to be as clean as possible. Since the structure is in micron size, existing dust (Figure 3.27) will affect the deposited pattern. Therefore, for micro-structure deposition, a clean environment is a needed. When an air bubble and debris present in the nozzle, other then non-firing nozzle and misdirect nozzle, the ejecting drop or more specifically the ligament extension will appear to "swirl" as the drop is being ejected.

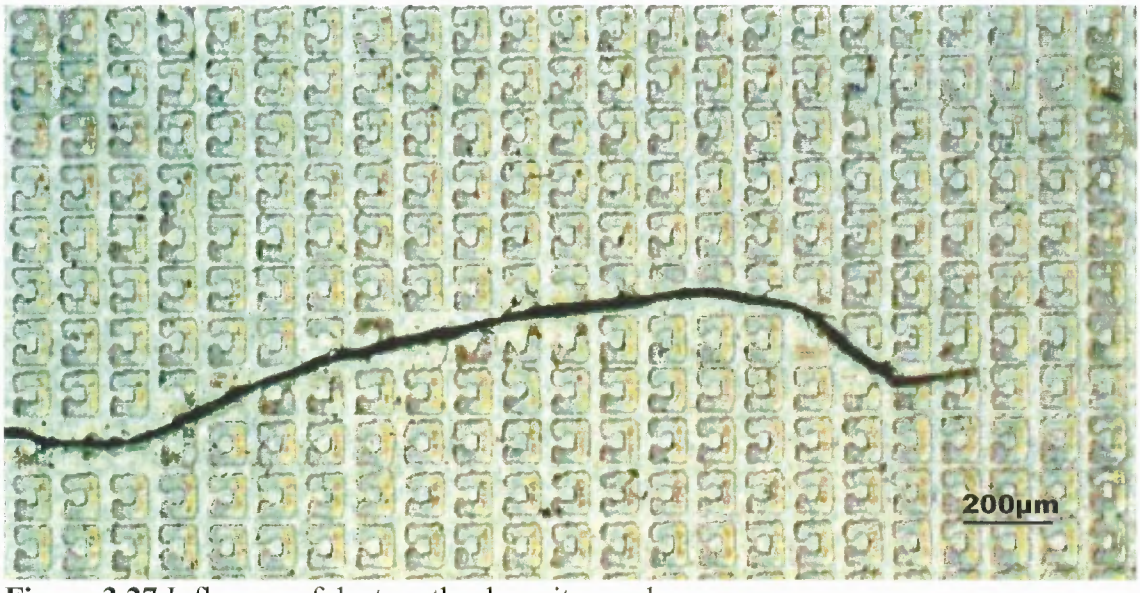

Figure 3.27 Influence of dust on the deposit sample.

3.8 Fabrication Result

The terahertz sensitive MTMs are successfully fabricated using the microfluidic-jetted technique. The fabrication result consists of 2D and 3D MTMs at various ranges for further testing.

Figure 3.28 showed the 3D LH MTMs with a lattice size of 200µm. Figure 3.28 (a) is individual images of the deposit SRR and microstrips of the 3D LH MTMs. This 3D structure consists of alternative stacking of SRR and microstrips sheet as illustrate in Figure 3.28 (b). The based sheet is polyimide substrate with SRR structure deposited in 3 layers of DDT-AuNPs. The DDT-AuNPs was deposit under 13 to 15V cartridge voltage and 4 to 4.5 inch H_2O meniscus pressure with the jetting waveform set to as shown in Figure 3.13 (b). During the deposition, the nozzle temperature was set to 28°C and platen temperature is set to 30°C. Each deposited layer was leaved heated in 60°C for 30min before second layer of DDT-AuNPs was deposited on top of first layer. Three layers of DDT-AuNPs were deposited on each sheet substrate. After three DDT-AuNPs layers

were printed on the sheet, the substrate was continually heat over night for 60°C. Even thought the curing for DDT-AuNPs is about 100-120°C, however heating with 60°C in a long period was enough for removing the dodecanethiol tail and formed a thin shining gold layer. Then second sheet is then stack on top of the deposited sheet and the microstrips is deposited on the second sheet. The material use for second sheet was self adhesive polymer cleaned with acetone. DDT-AuNPs was perfectly deposited on this material. The same deposited setting and curing method is applied. The final fabrication product is up to six stacking sheets which is total of three sets of LH MTMs.

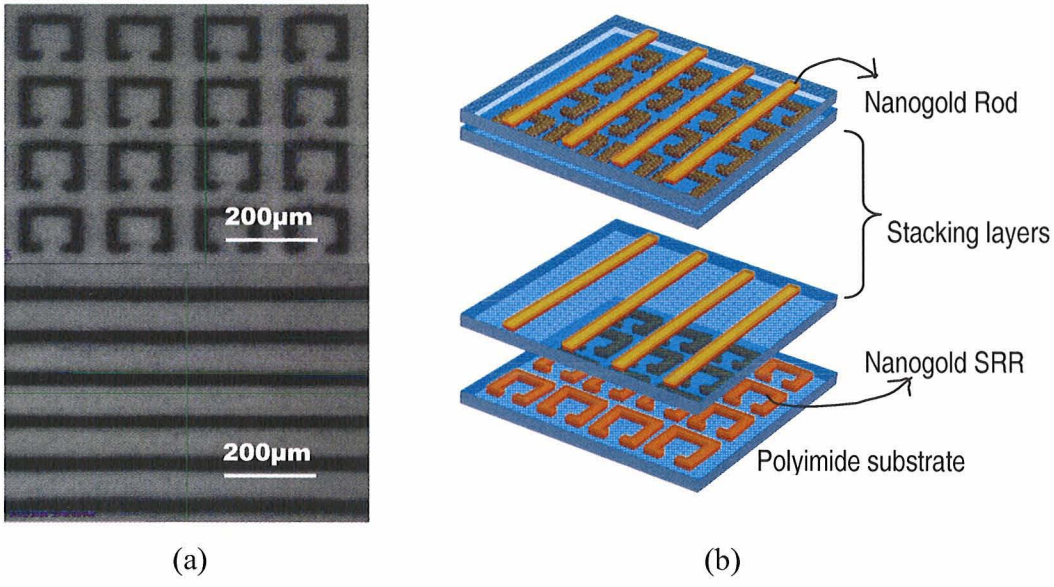

Figure 3.28 (a) Fabricated result of SRR (up) and rod (bottom) and (b) illustration of 3D LH MTMs with structural size of p=180μm deposited on 54μm thick polyimide substrate and ~43μm thick adhesive clear polymer as the stacking layers.

The thickness of one DDT-AuNPs layer is theoretically estimated by the solid contain of the remaining atomic molecular mass of the fluidic. The volume of the deposited drop V_D can be calculated from

$$V_D = \pi\left(\frac{d_D}{2}\right)^2 t \tag{3.3}$$

where d_D is diameter of deposited drop on substrate and t is thickness of the deposited drop. A single droplet volume can be obtained from relation of mass, volume and density. To do this, at least 1000 drops are jetted into the drop holder next to the drop watcher camera and the net weight is measured. But since the fluidic is expensive and the fast evaporated rate of fluidic solvent might contribute to huge percentage of uncertainty, thus there is no exact measure of the droplet volume could be made. Alternatively, the drop volume is possible to calculate form Equation 3.4 by estimated the drop diameter from drop image captured by drop watcher.

$$V_J = \frac{4}{3}\pi \cdot \left(\frac{d_J}{2}\right)^3 \tag{3.4}$$

where V_J is the jetting drop volume and d_J is the diameter of the jetting droplet. Obtained from drop image, the drop diameter is approximately 15±1μm and the drop volume is approximately 1.76pL. Since the image capture is not in high resolution, an uncertainty of ±1μm is estimated which contributed to ~18% of error.

The jetting drop volume and deposited drop volume should be equal. $V_J = V_D$. Then the thickness of the deposited drop is

$$t = \frac{V_J}{\pi\left(\frac{d_D}{2}\right)^2} \tag{3.5}$$

The deposited drop of DDT-AuNPs measured under microscope is 30μm. Thus, the thickness of the deposited drop is 2.482μm. For solid content of the DDT-AuNPs of 2%

weight per volume, the remaining thickness of the each deposited DDT-AuNPs layer is 49.65nm.

Figure 3.29 shows the 2D 80μm lattice size SRR and 80μm lattice size single-dot deposited with PEDOT: PSS on 10mil (127μm) and 4mil (51μm) polyimide substrate. The voltage used for deposition was 11-12V and the jetting waveform used was as shown in Figure 3.13 (a). The nozzle temperature and meniscus pressure was set to 28-30°C and 2-2.5 inches H_2O, respectively. The drop spacing use for this deposition was 10μm and the deposited drop diameter is approximately 18μm. The sample was heated at temperature of 30°C during deposition and left to dry in the same temperature for 30 minutes before the second layer was deposited on top of the first layer. There is total of two layers of PEDOT: PSS deposited for both SRR and single-dot.

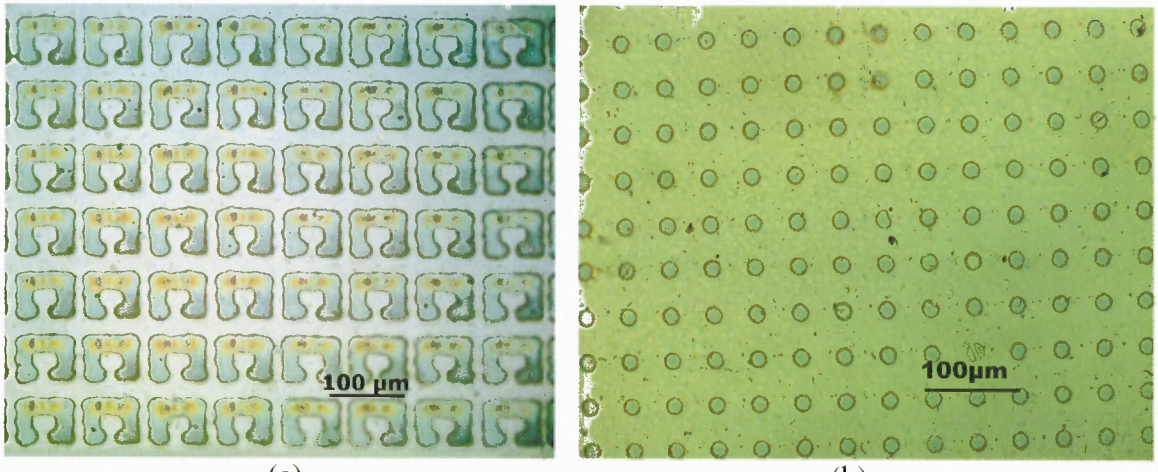

(a) (b)

Figure 3.29 2D MTMs deposited using PEDOT: PSS. (a) 80μm lattice size of SRR on 127μm thick polyimide substrate. (b) 80μm single-dot on 4mil polyimide. Image was taken by bright field microscope with 20x magnification.

Similar to the thickness calculation for DDT-AuNPs, and the jetting drop diameter measured was 12.5μm on average. Therefore, the calculated thickness is approximately 4μm for each layer. There is 20% weight of PEDOT: PSS in the solution, thus the thickness of one layer of PEDOT: PSS is 0.8μm.

Samples deposited using PEDOT: PSS have higher resolution then DDT-AuNPs since it drop diameter is relative small compare to DDT-AuNPs. Also, PEDOT: PSS has many advantages over other conducting polymers, such as high transparency in the visible range, excellent thermal stability, and aqueous solution processibility. However, PEDOT: PSS also suffers the low conductivity which is less than $1x10^7$ S/m. MTMs fabricated using this low-conductivity PEDOT: PSS may exhibit very low performance.

Figure 3.30 shows the result of copper SRR and microstrips that both have lattice size of 180μm. the fabrication of these samples was different then the fabrication of the samples in this thesis. In this fabrication, a conventional 9μm sputtering copper sheet is used as sample structure material and liquid polyimide was used as deposited material. the pattern in Figure 3.10 (b) was deposited on the copper surface with liquid polyimide. The pattern acts as a mask to prevent copper under the pattern etch away by the etchant. The deposited copper sheet was then gone though the etching after before it was annealed in 160°C for 30 minutes.

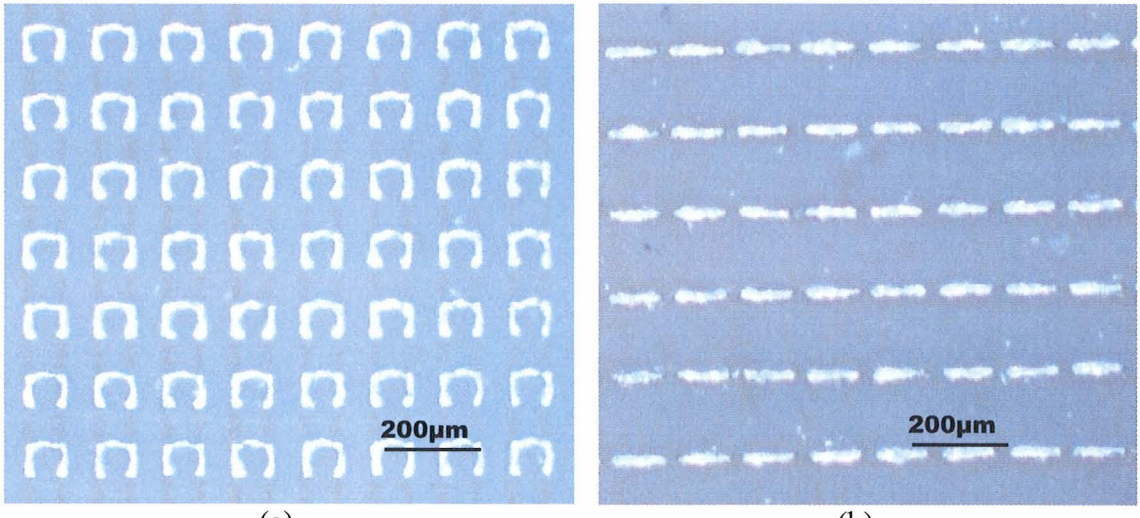

(a) (b)

Figure 3.30 Bright field microscope image of (a) copper SRR (b) and microstrips. Both structures have lattice size of 180μm.

As seen in the figure, the result samples fabricated with this method is not in perfect shape because of the fact that is over etching of the copper from the side of the mask. The deposited polyimide structure of SRR has dimension of (140×120) μm and the width of the structure is approximately 35μm but after the sample etch, the dimension and width have reduced to approximately (120×100) μm and 23μm, respectively. There is an average of ~19% of over etched contributed in this method. However, due to the better material thickness of the structure, the conductivity of the sample is promising.

CHAPTER 4

CHARACTERIZATION

4.1 Terahertz Time Domain Spectroscopy

THz spectroscopy covers the frequencies from 0.3 to 20THz or wave numbers from 10 to 600cm^{-1}. However, most of the work being done is in between 0.1 and 3THz where 1THz is equivalent to 300μm wavelength, 0.004eV photon energy, or 33.33cm^{-1} (wavenumbers). One advantage of THz time-domain spectroscopy (THz-TDS) is that the transient electric field is measured instead of its intensity. This determines the amplitude and phase of the spectral components that make up the pulse. The amplitude and phase can be directly related to the absorption coefficient and index of refraction of the measured sample. Thus, the complex-valued permittivity of the sample can be obtained without carrying out the Kramers-Kronig analysis. Terahertz spectroscopy is widely used to characterize most dry, nonmetallic and nonpolar objects like paper, plastics, and organic substances[84,85]. Polar liquids such as water strongly absorb in this frequency region[86]. In the gas phase, most polar molecules have very sharp and strong absorption lines in this frequency range, which reflect the unique rotational or vibrational spectra of the absorbing species[87].

4.1.1 THz Pulses Generation

THz pulses can be generated by many methods. A typical method for time domain spectroscopy relies on a broadband short-pulse terahertz source consisting of a split antenna which is basically a metal transmission line structure deposited on LTG-GaAs or other semiconductor substrate to create a switch (see Figure 4.1). This method was

pioneered by Auston [88] and later developed into free-space THz spectrometer by Grischkowsky[89]. An AC and DC bias is placed across the antenna to accelerate electron-hole pairs. When the visible laser pulse with energy above the semiconductor bandgap hits the biased gap of the semiconductor, electrons carriers are excited in to the conduction bands, and the resulting current in the antenna produces a terahertz electromagnetic wave. This radiation is collected and collimated with an appropriate optical system to produce a beam.

The generated rate of these free-carriers or electron-hole pairs is proportional to the intensity profile of the incident laser pulse and external bias. The photogenerated carriers then recombine, and the current in the dipole returns to its initial value. This whole process repeats with the arrival of the next optical pulse.

The details of the spectrum can vary significantly depend on the design of the switch and pump-laser power, pulse width, and configuration. Many emitter antenna geometries other than the Auston switch have been evaluated during the last decade. Examples are the bowtie antenna, interdigitated structures, spiral antennas or more sophisticated designs derived from microwave theory. In the experiment here, a bowtie antenna is used in the THz-TDS.

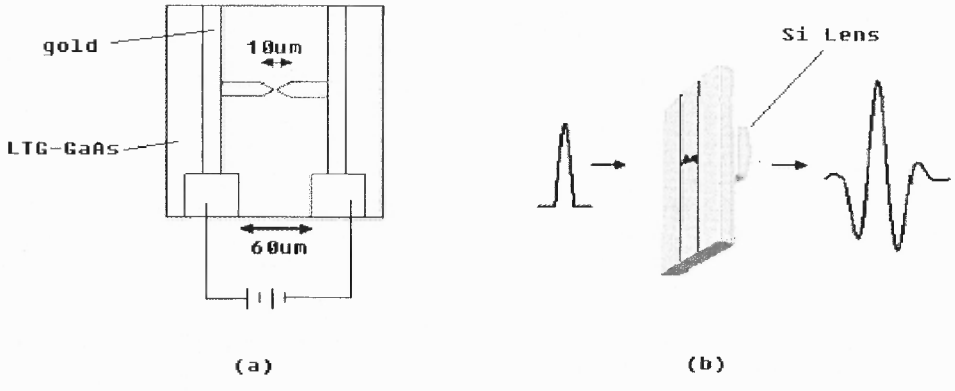

Figure 4.1 (a) Typical diagram and (b) terahertz radiation of bowtie antenna.

4.1.2 THz Pulses Detection

There are two methods for THz pulses detection: electro-optic detection and the photoconductive detection. Electro-optic detection is based on the change in the birefringence of a crystal, (usually ZnTe crystals are used,) in an external electric field. The THz pulse is used as the external electric field while the polarization rotation is measured by passing a linearly polarized sub-picosecond optical pulse collinear with the THz pulse. To measure the small electro-optic effect it is necessary that the optical pulse and the THz pulse are spatially and temporally coincident at the detector. The change in polarization is detected using a polarizing beam splitter and two balanced photo diodes.

Photoconductive detection is the method use for THz-TDS here. The principle of the photoconductive method is very similar but reverse to the generation discussed in Section 4.1. THz radiation propagate from free space is focused with an attached lens and illuminates the photoconductive switch. The electric field of the focused terahertz radiation induces a transient bias voltage across the antenna gap. This produces a measurable average current of the order of several hundred pico-amperes up to tens of nano-amperes and is obtained by measurement of the collected charge versus the time delay between the terahertz pulse and an optical pulse which synchronously gates the receiver. This receiving antenna is directly connected to a low-noise current amplifier.

4.2 Basic Analysis

In a THz-TDS a signal is proportional to the electric field of the THz pulse *E(t)*.

$$E(t) = \frac{1}{\sqrt{2\pi}} \int_{-\infty}^{\infty} E(\omega) \cdot e^{in\omega t} d\omega \tag{4.1}$$

To extract the frequency information, Fourier transform is used for the conversion. Thus,

$$E(\omega) = \frac{1}{\sqrt{2\pi}} \int_{-\infty}^{\infty} E(t) \cdot e^{-in\omega t} dt \tag{4.2}$$

and this complex expressed can be written as,

$$E(\omega) = A(\omega) e^{i\varphi(\omega)} \tag{4.3}$$

where, $A(\omega)$ is the magnitude and $\varphi(\omega)$ is phase of the wave. This states that the spectrum obtained by THz-TDS technique has the advantage of providing phase as well as amplitude information of the propagating pulse. The complex index of the media is given by:

$$\tilde{n} = n + ik \tag{4.4}$$

where n is the real index of refraction and k is imaginary part which relate to absorption, α, of the media.

$$k = \frac{\alpha c}{2\pi\omega}. \tag{4.5}$$

Thus, the THz E-field is modified after traveling a distance, d, through the dispersive medium, which is

$$E(t,d) = \frac{1}{\sqrt{2\pi}} \int_{-\infty}^{\infty} E(\omega) \cdot e^{i\frac{\omega n d}{c}} \cdot e^{-\frac{\omega k d}{c}} \cdot e^{-i\omega t} d\omega. \tag{4.6}$$

In a spectroscopic experiment, two traces of propagating pulse are recorded: through the sample, E_s and a reference pulse, E_r with the sample removed. The ratio of the Fourier transforms is a complex number that we can write as

$$\frac{E_s(\omega)}{E_r(\omega)} = R(\omega) e^{i\Delta\phi(\omega)} \tag{4.7}$$

where $R(\omega)$ is ratio of $A_s(\omega)$ and $A_r(\omega)$ and $\Delta\phi$ is different between ϕ_s and ϕ_r.

From these data, information about the sample, usually absorption and the real index of refraction n, is possible to extract. A model of the sample under study is typically required to extract the optical parameters. The model might include, for example the thicknesses and optical constants of various layers within the sample. For a simple model, the absorption and refractive index can be approximately as

$$\alpha(\omega) = -\frac{1}{2d}\ln(T) \tag{4.8}$$

$$n_S(\omega) = n_R(\omega) + \frac{c}{2\pi\omega d}\Delta\phi \tag{4.9}$$

where $T = \frac{|E_s|}{|E_r|}$ is the electric field transmission referenced to THz spectra with the sample removed. $|E_s|$ and $|E_r|$ are the magnitudes of the THz electric fields for the sample and reference, respectively. For this simplified model, the absorbance is just simply equal to -ln(T). $n_S(\omega)$ and $n_R(\omega)$ are real part of refractive index of sample and reference. Here the reference is the polyimide substrate with the refractive index of 1.8. d is the effective thickness of the sample.

4.2.1 Phase Unwrapping

In signal processing, when the phase is not constrained to an interval of $-\pi$ to π or 0 to 2π due to the periodicity of the arctan function, it is called an "unwrapped" phase. In working with phase delay, it is often necessary to "unwrap" the phase response. Phase unwrapping ensures that all appropriate multiples of 2π have been included in phase response. Phase unwrapping can be done by implementing a numerical algorithm for phase unwrapping. The Labview program has this phase unwrap function under spectral measurement package which implements a numerical algorithm for phase unwrapping.

4.2.2 FFT and Aliasing

To obtain the Fourier ratio from the experiment, the signal at the detector is measured. One sample of data at each position of the delay stage is record and there are N samples in total. This gives discretely sampled signal in time interval Δt.

$$E_n = E(n\Delta t),\ n=1,2,3....N \tag{4.10}$$

The reciprocal of the time interval Δt is called the sampling rate. And it relate to a special frequency called Nyquist critical frequency which is

$$f_c = \frac{1}{2\Delta t} \tag{4.11}$$

The sampling theorem states that if a continuous function $E(t)$ that is sampled at an interval Δt, is known to be bandwidth limited to frequencies smaller than fc then it is completely determined by it's samples E_n. Any frequency component outside the frequency range $(-fc; fc)$ is aliased (falsely translated) into that range. Aliasing refers to an effect that causes different continuous signals to become indistinguishable when sampled.

4.2.3 Spectra Resolution

Frequency resolution is the minimum frequency difference between two sinusoids which allows resolving two distinct peaks in the spectrum. The frequency resolution is determined by the total Scanning length or duration of the signal for the FFT spectrum. The Δf between two neighboring points is

$$\Delta f = \frac{c}{2l} \tag{4.12}$$

where c is speed of light and l is the scanning length. The resolution can in principle be improved by increasing the scanning length.

4.2.4 Dynamic Range

Dynamic range is the signal range above the noise floor in the spectrum. In Figure 4.2 (b), the dynamic range is up to 1.5THz. A flat portion of the spectra above ~1.5THz represents the noise floor of the T-ray 2000 system. In practice, the dynamic range limits the maximal magnitude of the absorption coefficient that can be observed towards higher frequencies. For samples whose absorption rises with growing frequencies, this effect can lead to a roll-off in apparent absorption which can easily be confused with an absorption peak.

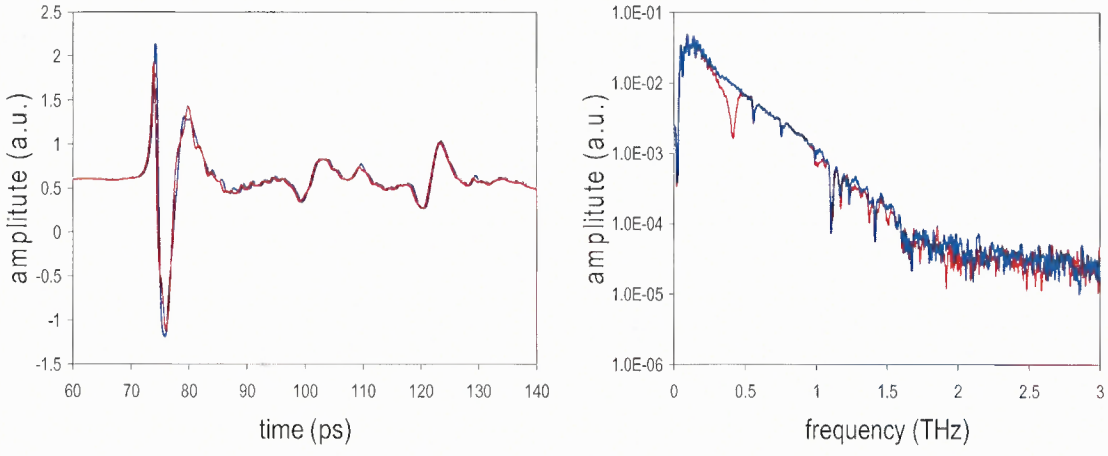

(a) (b)

Figure 4.2 (a) time domain and (b) frequency domain data of polyimide substrate (blue) as reference signal and copper SRR $\theta=0^{o}$ (orange).

4.3 Uncertainty in THz-TDS

This section lists the major experimental errors in THz-TDS and methods of quantifying the errors.

4.3.1 Noise

Noise in the THz-TDS system can be defined as a background or white noise due to instruments and a systematic noise due to the optical pulses from the transmitter and receiver. The dipole antenna is extremely sensitive to charge: a small static spark will damage the source. Therefore, a ground discharge wrist band should wear when touches the transmitter and receiver. The noise will become very large compared to the other noise sources if the antennas are damaged.

In addition, every electric device has 60Hz noise from the power line. The photoconductive THz switch also has 60Hz noise due to the sensitive of photoconductive switch to the room lights. This problem can be reduced by turning off the room light or blocking the room light from the receiver chip.

The stability of optical pulses generated through the Ti: Sapphire laser varies over time. These effects become important when performing measurements that require long time intervals. For better noise reduction, more signal averaging is applied in data acquisition.

4.3.2 Alignment Error

In the THz-TDS system where photoconductive technique is used, the alignment and focusing of the femtosecond laser becomes very important where the laser is needed to focus into a gap between two gold conductors on a LT-GaAs. The detection mechanism is most efficient if the laser focus spot size matches the gap.

In addition, the free space transmitter and receiver alignment is important for broaden the dynamic range of the system. With proper align in the THz-TDS system, the bandwidth can expend to 2.3THz. Also, a narrow time window allows for the detection of

broad spectral peaks and can also be used to eliminate the Fabry-Perot type interference effects that can be incurred from multiple reflections as the pulse propagates through the sample.

4.3.3 Water Vapor

Interaction with ambient water vapor in the air becomes a significant factor in signal quality when THz beam propagates in free space. The propagation of THz beams through water vapor was already discussed in previous papers[90]. Like other spectroscopy systems, to generate a clean output spectrum, the THz system can be located in the airtight dry box free from humidity.

4.4 Experimental Setup

A T-ray 2000 Spectroscopy system (Picometrix, Inc) is used in the transmission mode as shown in Figure 4.3 to measure the THz time-domain waveform. A modelocked Ti: sapphire laser provides 80fs pulses with wavelength of 780nm at a repetition rate of about 80MHz. The pulse beam is directed into grating dispersion compensator which adds negative dispersion to the pulses to compensate for the dispersion of the light pulses as they travel through the optical fibers. A THz pulse is generated by illuminating a biased photoconductive switch with the optical pulses. As elaborate in the section above, the switch is a miniaturized bowtie antenna structure (gold) fabricated on top of low-temperature grown GaAs which acts as a fast photoconductor. When the biased photoconductor is illuminated, a surge of current radiates a THz pulse. The pulse is collimated by a set of silicon lenses in the transmitter module. The THz waveform is detected by a second photoconductive switch.

In the detector, the incoming THz electric field acts as an electronic bias. When the photoconductive switch is activated by an optical pulse, a small current is generated that is proportional to the instantaneous value of the THz electric field. The full THz time-domain waveform is recorded by varying the time delay between the generating and detecting optical pulses from the Ti: Sapphire laser. This is usually done with a retro reflector mounted on a delay stage inside the control unit.

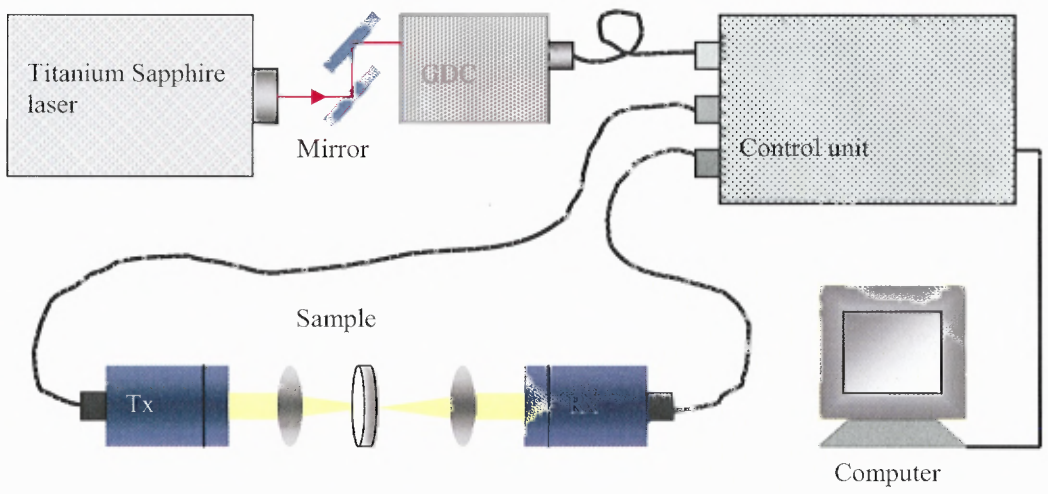

Figure 4.3 T-ray 2000 setup.

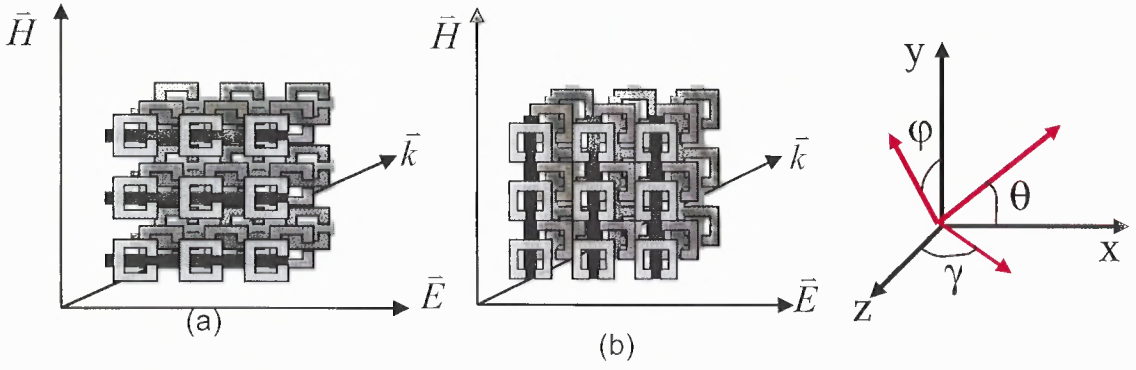

Figure 4.4 Orientation of the sample relative to the incident wave propagation (a) case 1 where the E-field is perpendicular to the open gap of SRR and (b) case 2 is where the E-field is parallel to the open gap of SRR.

The sample is placed in between the terahertz transmitter and detector in two orientations: case 1, the SRR gap is parallel to the E-field and case 2, the SRR gap is perpendicular to the E-field (see Figure 4.3). The THz time domain waveforms are acquired by recording the THz transmitted pulse at each sample orientation. Spectral information as a function of frequency, both phase and amplitude is acquired through a Fourier transform of the time-domain data.

4.5 Characterization Result and Discussion

The samples characterized using THz-TDS were PEDOT: PSS SRR p=80μm, 3D DDT-AuNPs LHM p=180×180×52μm, copper SRR, copper microstrips and 3D copper LHM p=180×180×55μm fabricated using microfludic-jetted method discussed in Chapter 3.

Figure 4.5 shows the result for DEPOT: PSS SRR. Although the PEDOT: PSS fluidic provides smaller drop size for high resolution fabrication, the conductivity of PEDOT: PSS is very low. Thus in Figure 4.5, there is no significant peak observed in the characterized result. Minor distinguishable peaks have observed at around 0.28 and 0.43 THz as compare the result for case 1 and case 2. But since the amplitude different small and the noise is relatively high due to internal reflection of 127μm polyimide substrate, the result is nebulous just by observing the experimental result. Later, to be confirmed in chapter 5, a simulation peak is actually occurred at 0.4 THz for conductivity above 3×10^7 S/m. In addition, THz-TDS does not provide time-resolved dynamical information of PEDOT: PSS. In order to measure the transient electron, a pump probe laser is added to activate the electron-hole pair generation of the PEDOT: PSS bandgap and this discussion is included in the future work.

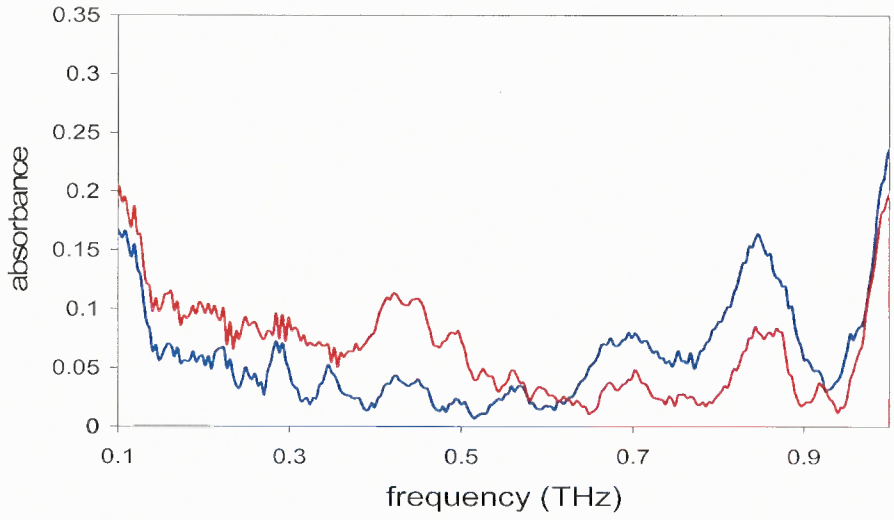

Figure 4.5 Data measured for SRR of lattice size, p=80μm fabricated with PEDOT: PSS on 127μm polyimide substrate. Incident THz wave is propagated perpendicular to the sample plane and sample is oriented in case 1 (blue) and case 2 (orange).

Figure 4.6 shows the result of the sample measured when the THz wave incident normal to the sample plane or xy-plane. The sample is oriented in case 1 or 0°, 30°, 60° and case 2 and 90°. This structure is shown to support a frequency band of 0.15THz for case 2 structure orientation.

Theoretically, electromagnetic waves can couple with SRR and microstrips to produce electromagnetic responses if either the E-vector or H-vector has a component normal to the plane of structure. In the experiment, both the E vector and H vector of the wave are parallel to the plane of the sample which indicates that there would be no induced magnetic resonance. However, this is not always the case[91]; electric coupling to the magnetic resonance should also exist in the SRR. As for case 2; the electric field vector of the terahertz wave is parallel to the gap of SRR, which breaks the symmetry of the electric field configuration on both sides of the SRR. This consequently generates a circular current inside the SRR leading to the magnetic resonance of the structure. Therefore, the absorbance peak in case 2 at about 0.15THz can be interpreted as a

magneto-dipole resonance, for which the energy totally comes from the electric component of the terahertz wave without the influence of the magnetic component. For case 1, where the electric field vector is perpendicular to the gap of SRR, it will only generate current flowing left and right, instead of inducing a circular current, inside the SRR. Thus, there is no magneto-dipole resonance in case 1. Also, since there is no significant peak observed for case 1, this suggests that there is no electric response from microstrips. This perhaps is due to the limitation of sample thickness that results in high resistivity.

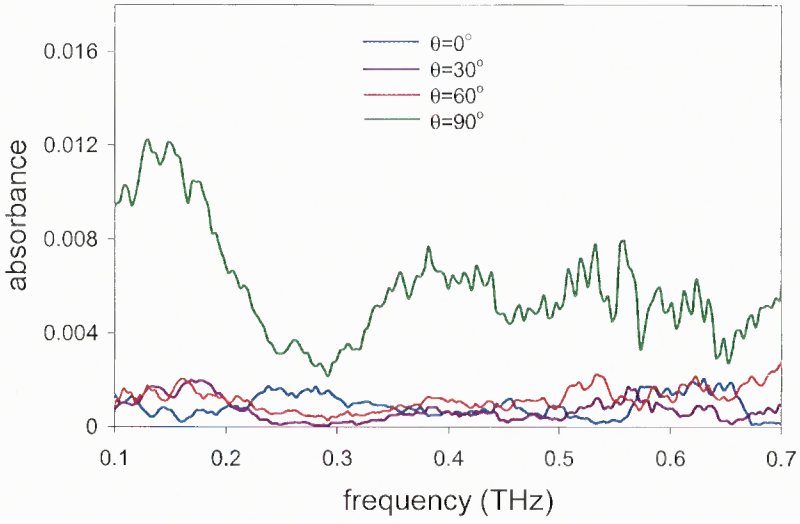

Figure 4.6 Experimental result of 3D DDT-AuNPs LHM with incident wave perpendicular to the sample plane or xy-plane.

Figure 4.7 shows the data obtain from the same sample but this time the angle was rotated in yz-plane where the H-field vector have component in *z*- direction that induces a circular currents in the SRR resulting magnetic resonance. As shown in the experiment result, magnetic resonance is observed at 0.18 THz which matches with the result of Figure 4.6. However, the resonance peak is very weak and also the Fabry-Parot interference due to the total internal reflection of stacking layers is obviously observed

for large φ. Also a sharp peak at 0.55THz in both case 1 (Figure 4.7 (a)) and case 2 (Figure 4.7 (b)) is believed that are signatures of water vapor. In Figure 4.6, exhibit minimum absorbance for case 1 and maximum absorbance for case 2 at 0.15THz. This is equivalent to $\varphi=0^{o}$ of case 1 and case 2 of Figure 4.7, respectively. However, the absorbance amplitude of case 2 $\varphi=0^{o}$ in Figure 4.7 is much lower then case 2 of Figure 4.6. This probably because of the oxidation of nanogold layers since the data was measured after few weeks from the previous experiment.

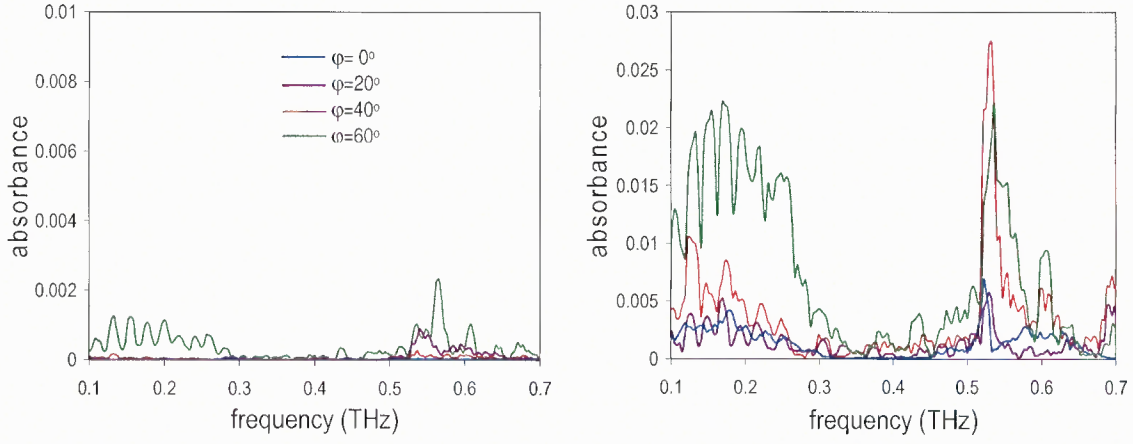

Figure 4.7 Measured data of 3D DDT-AuNPs LHM with angle φ rotate in yz-plane. Sample oriented in (a) case 1 and (b) case 2.

In addition, the sample was investigated in varying angle γ of xz-plane. Figure 4.8 shows the result of the experiment for angle γ rotate from 5^{o} to 40^{o}. The sample orientation is 0^{o} (case 1), 45^{o} and 90^{o} (case 2). In the experiment result, there is no distinguished peak observed. But there is a change in absorbance amplitude for the sample oriented in 45^{o} and 90^{o} while 0^{o} remain in the lowest absorbance. This is because when the sample rotates in angle φ or γ, the lattice dimension relative to the incident wave is varied. By employing the effective-medium theory, the change of the lattice dimension due to the incident wave would affect the macroscopic effective properties.

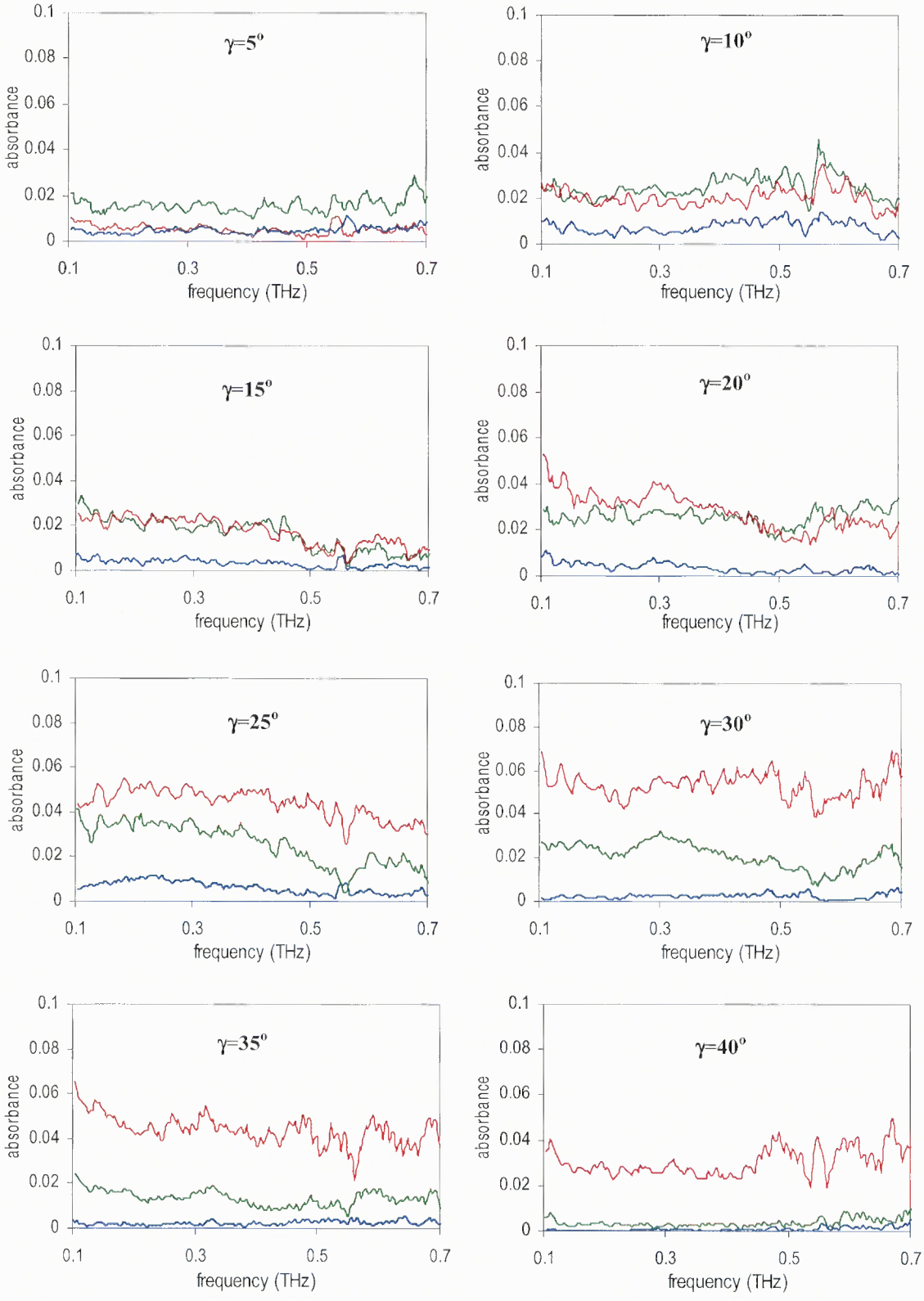

Figure 4.8 The results of 3D LHM measured with sample rotate in xz-plane, γ=0° to 40° and sample oriented in case 1 or 0° (blue), 45° (orange) and case 2 or 90° (green).

Figure 4.9 shows the data obtain from the copper sample both SRR and break-microstrips when the incident wave is perpendicular to the sample plane. The data is measured with sample orientated from $\theta=0^{o}$ (case 1) to 90^{o} (case 2) in the x- and y- plane. Figure 4.9 (a) shows the absorbance spectra of SRR. There are two absorbance maxima in the spectra, one located at 0.42THz and the other located at 0.98THz. For case 1, the absorbance maximum is observed at 0.98THz only. While for case 2, a major peak is observed at 0.43THz and a secondary minor peak is at 0.98THz. The different angular dependences of the two absorbance peak suggested that the SRR should act not only as a magnetic dipole, but also as an electric dipole as discussed in detail by Marqués *et al.*[92] and Chen *et al.*,[93]. So the first resonance comes from the magnetic response, and the second resonance comes from electric response which is known as a plasmonic resonance.

In Figure 4.9 (b) shows the angular dependence of SRR. The blue and green curves indicate the amplitude of the absorbance at 0.43THz and 0.98THz, respectively. These responses are expected to form sine or cosine function as angle rotate in cycle. But in the experiment result, exhibit deviation from simple sine/ cosine function. This maybe explains by the possibility of imperfections in fabricated sample. The changes of the absorbance amplitude relative to the rotated angle in sample plane are due to the fact that E-vector and the SRR gap were changed from parallel to perpendicular.

Figure 4.9 (c) and (d) shows the absorbance spectra and angular dependent of microstrips which indicate a significant absorbance peak at 0.69THz for 0^{o} where the strips parallel to E-field. As discussed by J.Brown, the microstrips have only electric response due to its symmetry nature.

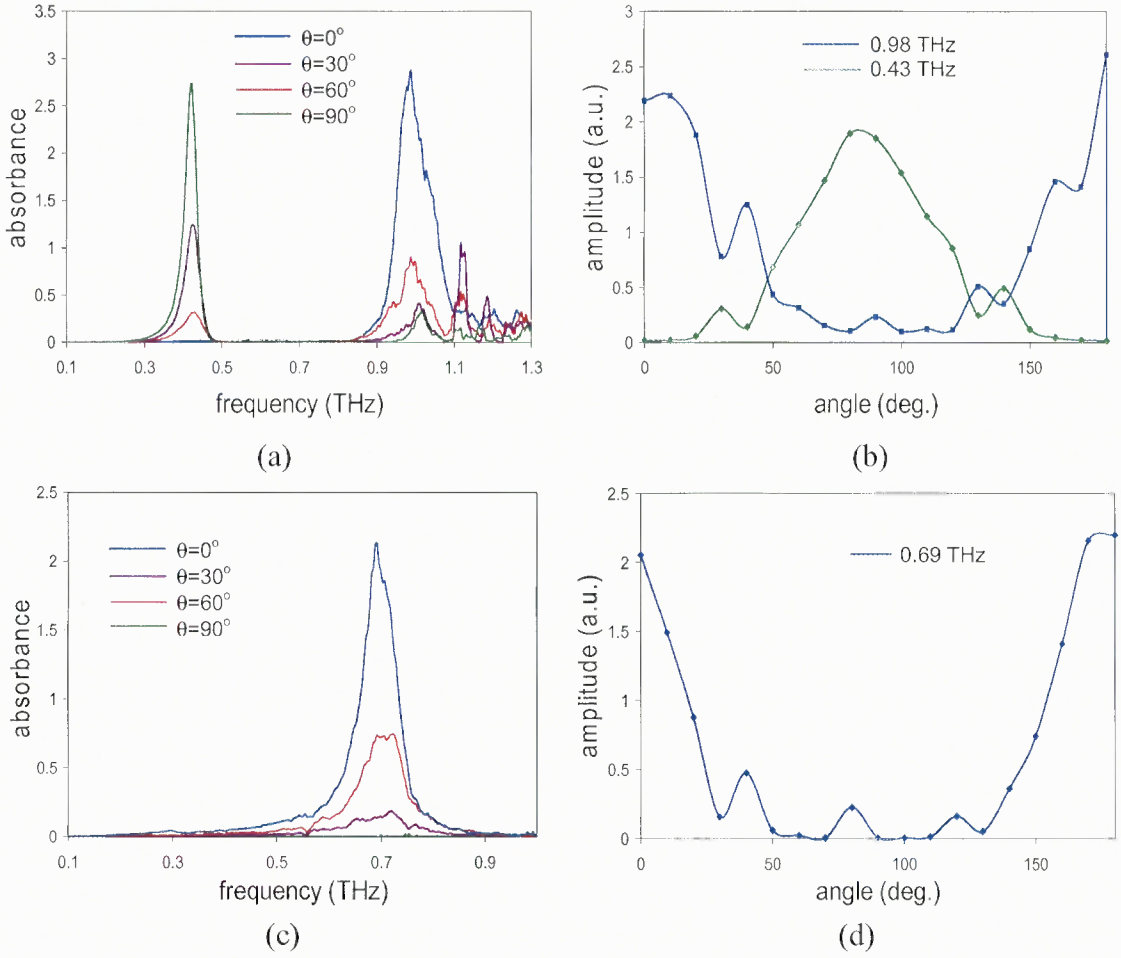

Figure 4.9 Measured data with THz signal propagated into the plane of sample (a) SRR (c) microstrips. Sample is rotated in xy-plane (sample plane) from 0° (blue), 30° (orange), 60° (purple) and 90° (green). The amplitude of the peak due to its rotation angle for (b) SRR at peak 0.43THz (green) and 0.95THz (blue) and (d) microstrips at peak 0.69THz.

Figure 4.10 shows the experiment result of copper SRR measured with sample orientation of case 1 (Figure 4.10 (a)) and case 2 (Figure 4.10 (b)). At each cases, the sample is rotated in yz-plane with angle φ. For φ=0° in case 1 and case 2, the results indicate a perfect match with Figure 4.9 (a) θ=0° and 90°, respectively. For higher φ, the results exhibit obviously shifted of the peak frequency for sample oriented in case 1 but not in case 2. Also in case 1, the secondary peak at lower frequency is observed for φ other then 0° showing that is a secondary resonance occurs owing to the z-component of magnetic coupling in the sample plane where φ is not 0. In case 1, E-field vector induced

back and forth current at each side of SRR, this current would react with H-field vector component and form a secondary resonance. While in case 2, the induced current is in circular form circulating SRR and this would only add amplitude to the resonance along with H-field component added. However, the shifted of peak frequency in case 1 is not linearly depend on θ. The reason of this phenomenon is unclear. A similar explanation can be applied to microstrips result shown in Figure 4.11 (a). And for case 2 (Figure 4.11 (b)), there is no electromagnetic response occurred.

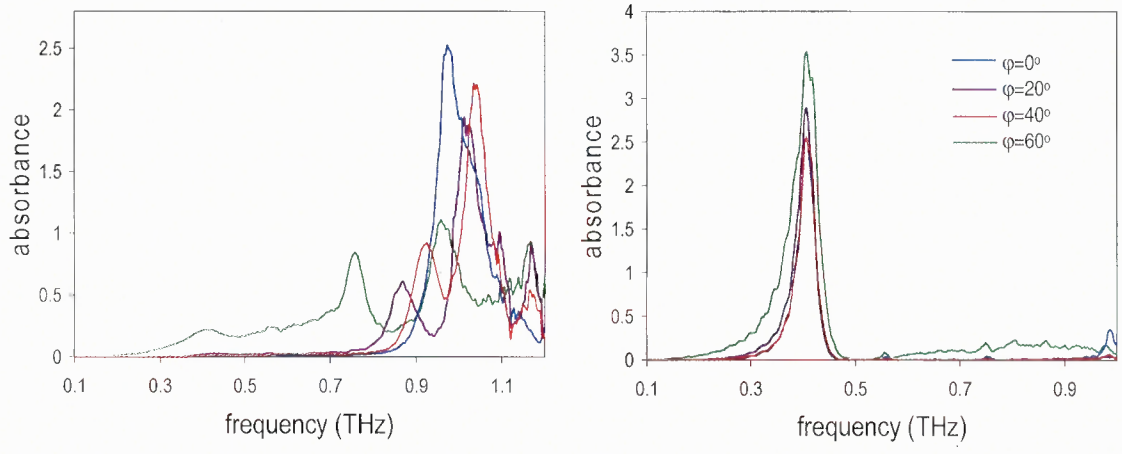

(a) (b)

Figure 4.10 Measured data of SRR, p=180μm, with varying angle in yz-plane. Data measured in two cases which are (a) case 1 (b) case 2 as shown in Figure 4.4.

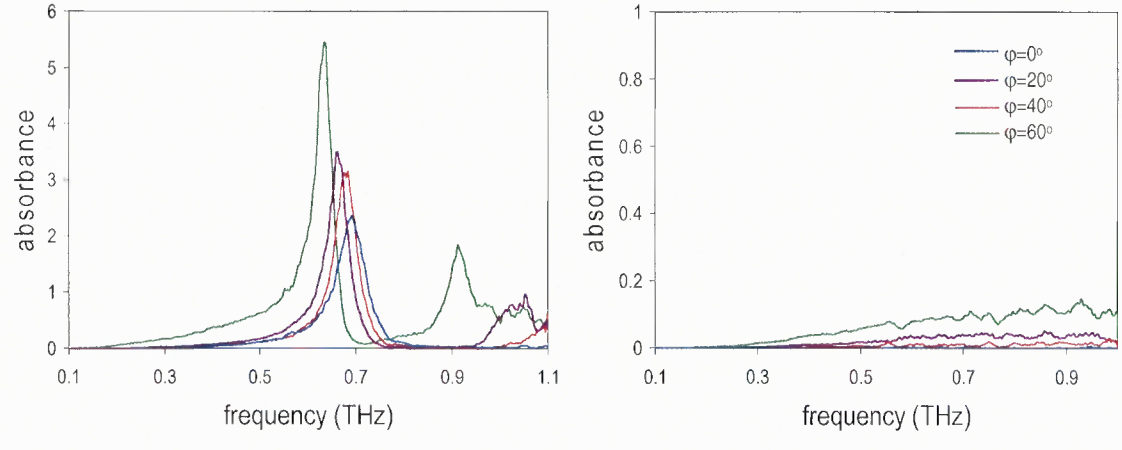

(a) (b)

Figure 4.11 Measured data of micro-strip with varying angle in yz-plane. Data measured in two cases (a) trip orientation parallel to E-field (b) strip perpendicular to E-field.

Figure 4.12 shows the absorbance peak of copper LHM. It obviously shows that the results of LHM exhibit the combination results of individual copper SRR and microstrips (see Figure 4.9). The first and third absorbance peak located at 0.43THz and around 0.98THz, respectively, are consequence from electric coupling magnetic response of SRR structure. The second absorbance peak located at 0.69THz is result from electrical response of microstrips. The major distinguishable phenomenon from results of LHM and individual SRR/ microstrips is the shifting of the second and the third absorbance peak. The third absorbance peak shift to higher frequency for larger θ . The only reason that may explains this phenomenon is the human error in alignment sample to the incident k-vector. The sample maybe has a small angle tilted from xy-plane that causing this shifting peaks. Similar case, as refer to Figure 4.13, the result of LHM exhibits the combination result as in the individual SRR and microstrips (refer Figure 4.10 and Figure 4.11).

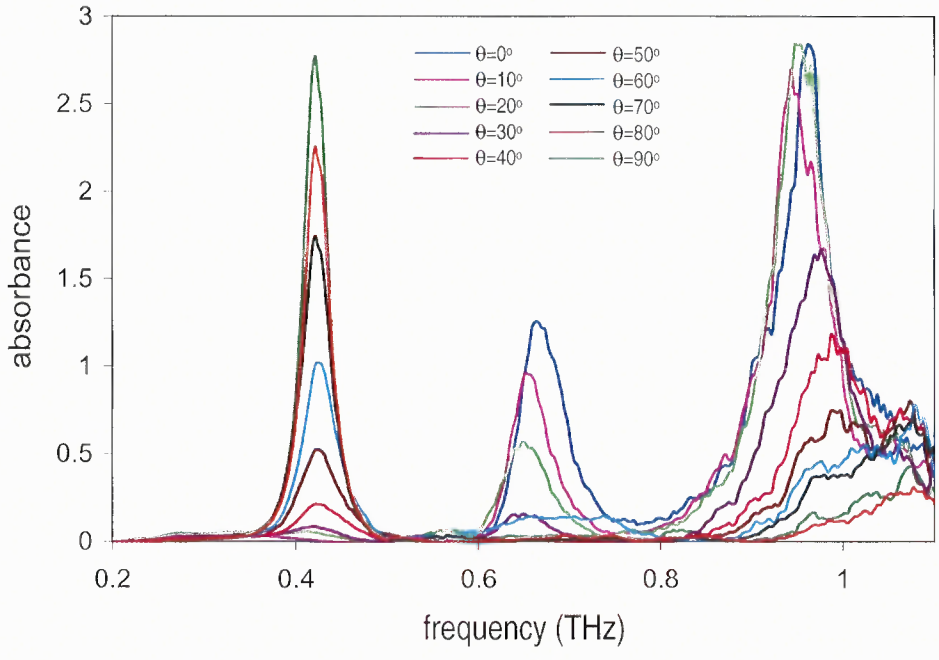

Figure 4.12 The experimental result of copper LHM. The sample measured in THz wave incident to the sample plane and the sample was rotated from θ=0° to 90° in xy-plane.

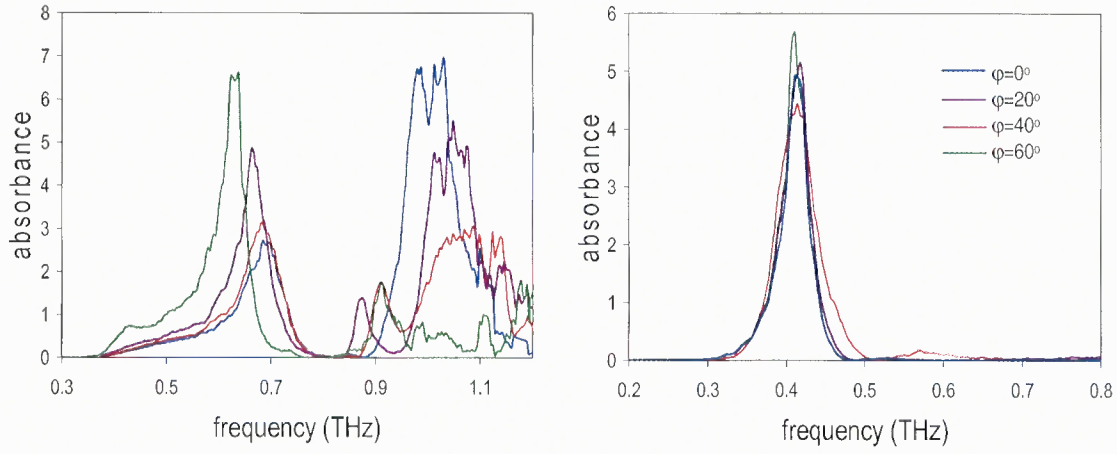

(a) (b)

Figure 4.13 The experiment result of copper LHM. The sample was rotated in yz-plane while the wave propagated in the z-direction. The orientation of sample: (a) case 1 and (b) case 2.

As summary of this chapter, of the three types of samples tested the copper samples have exhibit the best characterization results. DDT-AuNPs exhibits resonance as well but the result from PEDOT: PSS did not exhibit any SRR interaction with the THz field. Copper LHM has exhibit the characteristic of combination individual SRR and microstrips. In addition, the fabrication of the copper samples is relatively easy then fabrication of DDT-AuNPs and PEDOT: PSS samples thus adding potential for future device innovation. The DDT-AuNPs LHM sample have distinguishable result from case 1 and 2, even though the amplitude of the absorbance is extremely low compare to copper sample, this is due to the limited of conductivity in deposited layers of the sample. Plus, the stacking layers of the sample cause the Fabry-Perot effect that broadens the magnetic resonance peak. PEDOT: PSS sample has failed to produce a distinguish result of case 1 and case 2 since the conductivity is extremely low.

CHAPTER 5

SIMULATION

The procedure for extracting the negative index of MTMs based on THz-TDS measurements of samples is presented simply using an Excel add-in program. In order to corroborate the experimental extraction, a frequency domain finite element method (FEM) simulation with several typical assumptions is used for verification.

5.1 Properties Retrieval

It is known from fundamental electromagnetism theory that a magnetic dipole can be realized by the circulating current of a closed metallic loop which leads to a magnetic moment. The magnitude of the magnetic moment is given by the product of the current and the area of the loop and its direction is perpendicular to the plane of the loop contributed to stored magnetic energy which related to the self-inductance, L, of the loop. If the cut is made in the loop, then its acts like a capacitor, with capacitance C. One obtains an LC circuit, with a resonance frequency

$$\omega_{LC} = \frac{1}{2\pi\sqrt{LC}} \tag{5.1}$$

Thus, a SRR acts like an electromagnetic resonator (see Figure 5.1 (b)), producing at ω_{LC} resonant circular currents and a resonant magnetization, i.e. resonant effective permeability.

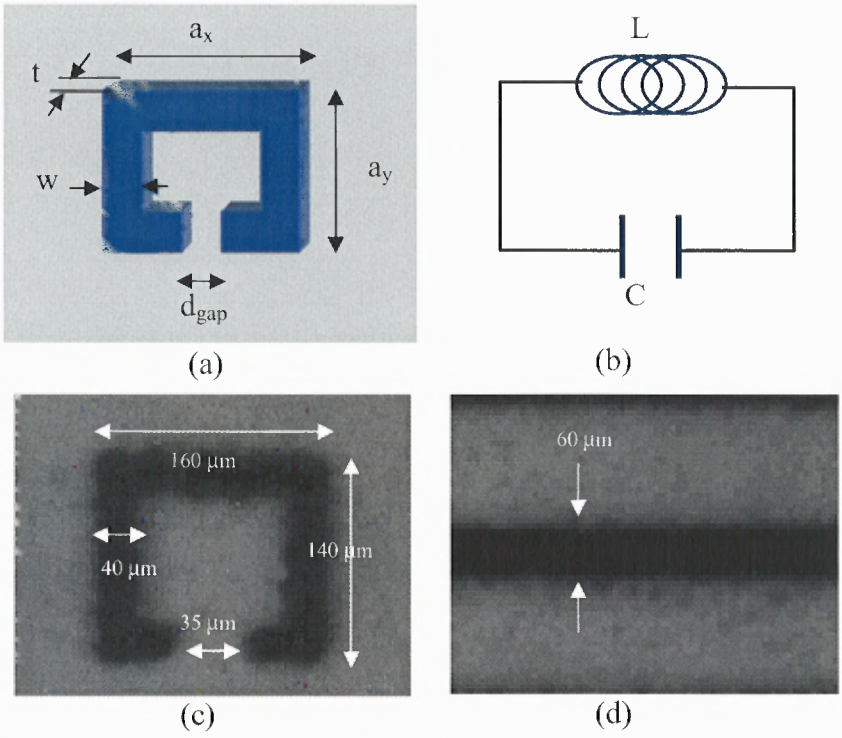

Figure 5.1 (a) and (c) shows the geometry of SRR element (b) the analogeuos circuit of SRR and (d) shows geometry of microstrips.

The order of magnitude of the resonance frequency for such an SRR can be estimate by considering the SRR capacitance in the area of its gap, treating the gap as a parallel plate capacitor with

$$C_{SRR} = \varepsilon_o \varepsilon_C \frac{wt}{d_{gap}} \tag{5.2}$$

where w is width of the SRR side, d_{gap} is the width of the gap, t is the thickness of the structure, and ε_c is the relative permittivity of the material in the gap of the capacitor. The inductance formula of the SRR is

$$L_{SRR} = \mu_o \frac{a_x a_y}{t} \tag{5.3}$$

where a_x and a_y are the length of SRR in x and y, respectively. By Applying Drude theory in effective permittivity and permeability, the generic frequency dependence of the effective permeability that Pendry *et al*[1]. calculated was showed in Equation 2.5.

Also, by applying the Kirchoff rule, the effective permeability is obtain[94] as

$$\mu_{eff}(\omega) = 1 + \frac{F\omega^2}{\omega_{LC}^2 - \omega^2 + i\varsigma\omega} \tag{5.4}$$

By comparing these equations, one can conclude ω_{LC} is analog to ω_{om} in Equation 2.5. The filling factor, F, and damping constant, ζ, are constants relates to the geometry and materials composing the artificial medium. In SRR, the filling factor is simply equal to

$$F = \frac{a_x a_y}{p^2} \tag{5.5}$$

And the damping constant of SRR is defined in Equation 2.7.

The infinite microstrips medium alone can be characterized by an effective permittivity having the same form as a dilute, collisionless plasma, which is define in Equation 2.2. Inductance and capacitance for infinite microstrips are

$$L_{\inf MS} = \frac{\mu_o l}{2\pi} \ln\left(\frac{2l}{w}\right) \tag{5.6}$$

$$C_{\inf MS} = \varepsilon_o \varepsilon_r l \tag{5.7}$$

For which l is the length of the microstrips In this case, l is equal to lattice length, p. Thus, by applying Equation 5.1, the plasma resonance of infinite microstrips is

$$\omega_{pe} = \frac{2\pi \cdot c}{p} \sqrt{\frac{1}{\ln\left(\frac{p}{w}\right)}} \tag{5.8}$$

Typically, in the quasi-static regime, the effective permittivity of infinite lattices of unloaded wires is described using the Drude model as shown in Equation 2.2. However, for semi-finite microstrips medium, effective permittivity is deduced to[95]

$$\varepsilon_{eff}(\omega) = 1 - \frac{\omega_{LC}^2}{\omega^2 - \omega_{LC}^2 + i\omega\varsigma} \tag{5.9}$$

By applying Equations 5.1 to 5.8 and structure parameter listed in Table 5.1, the effective ε and μ parameter of DDT-AuNPs is retrieved and shown in Figure 5.2. The simulated absorbance at 0.15 THz (Figure 5.2 (d)) has showed that it is match with the experimental result although the amplitude different is not same. The extracted index of refraction (Figure 5.2 (c)) has negative value below cutoff and the peak is −1.6 occurs at peak 0.14THz.

The simulation of PEDOT: PSS SRR shows (Figure 5.3) there should have an absorbance peak located at 0.48THz if highly conductivity material were used. However, since the conductivity of PEDOT: PSS for the experiment was low, there are no shows of absorbance peak as predicted in the simulation result.

Table 5.1 List of Structure Parameters of the Samples

DDT-AuNPs, $\sigma = 5\times10^7$ S/m							
	p (μm)	l (μm)	a_x (μm)	a_y (μm)	W (μm)	t (μm)	d_{gap}(μm)
SRR	180		160	160	35	1	40
Infinite-microstrips	180	180	-	-	60	1	-
PEDOT: PSS, $\sigma = 1\times10^7$S/m, 3×10^7S/m, 5×10^7S/m							
SRR	80	-	65	60	20		10
Copper, $\sigma = 1\times10^{16}$ S/m							
SRR	180	-	120	100	23	9	50
Break-microstrips	180	140	-	-	45	9	20

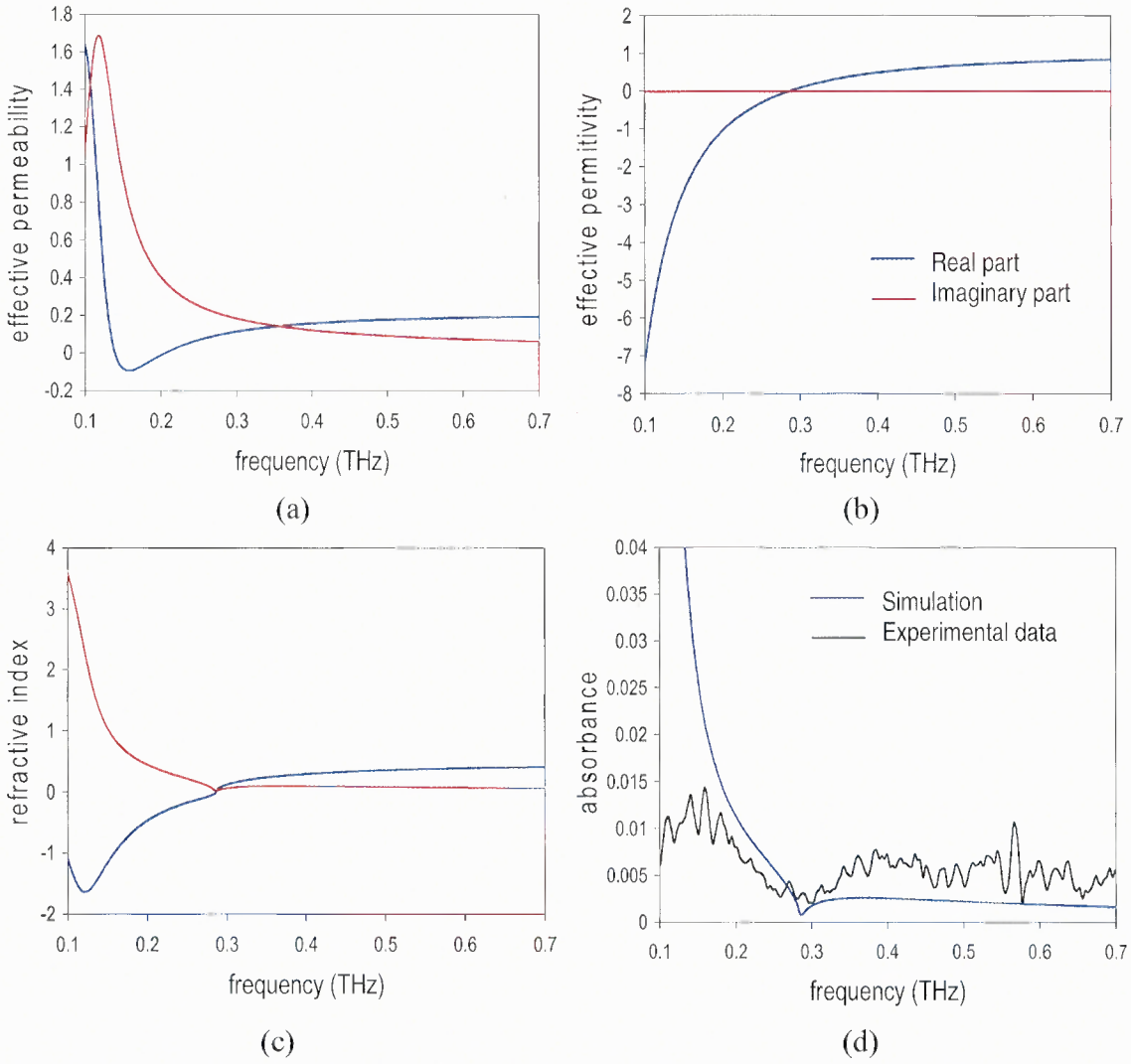

Figure 5.2 Simulation results for 3D DDT-AuNPs LHM (a) effective permeability plot, (b) effective permittivity plot, (c) refractive index, and (d) simulation absorbance compare to measured absorbance data.

Figure 5.4 and Figure 5.5 show both the simulation and experimental results for copper SRR and break-microstrips. The simulation and experimental result for the copper and SRR and break-microstrips are closely match. However, the results also show that is no negative index of refraction occurs in this sample since the effective permittivity resonance of the break-microstrips is too far away from the SRR magnetic resonance.

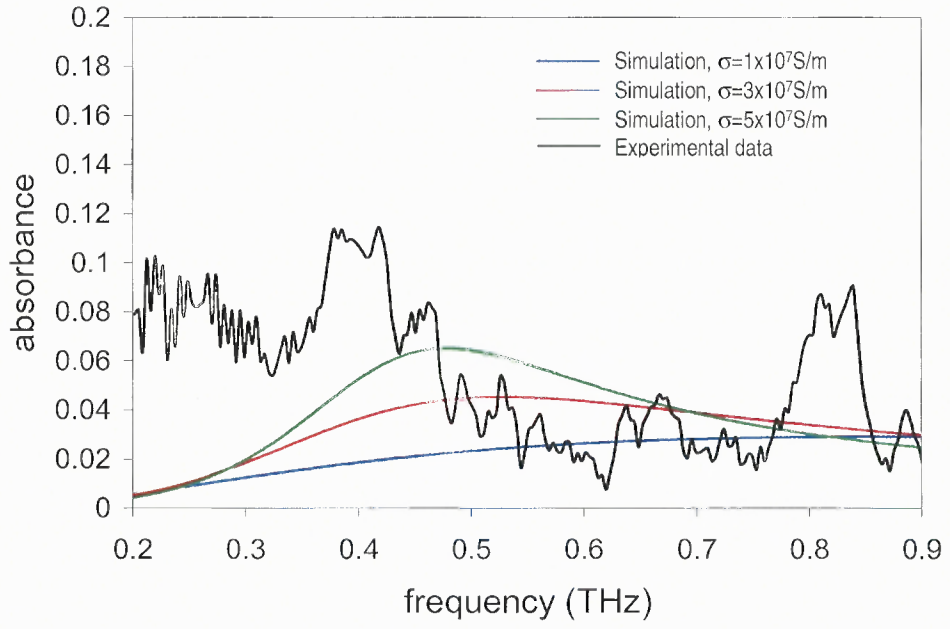

Figure 5.3 Simulation results for DEPOT: PSS SRR in increasing conductivity compared to measured absorbance.

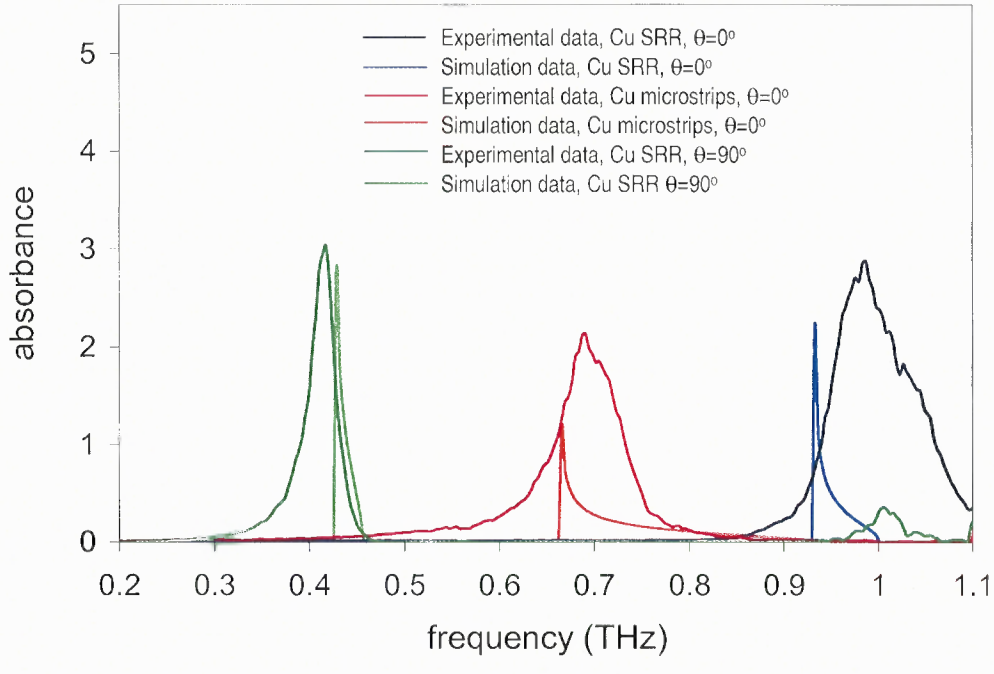

Figure 5.4 The comparison of simulation and experimental absorbance of copper SRR and break-microstrips.

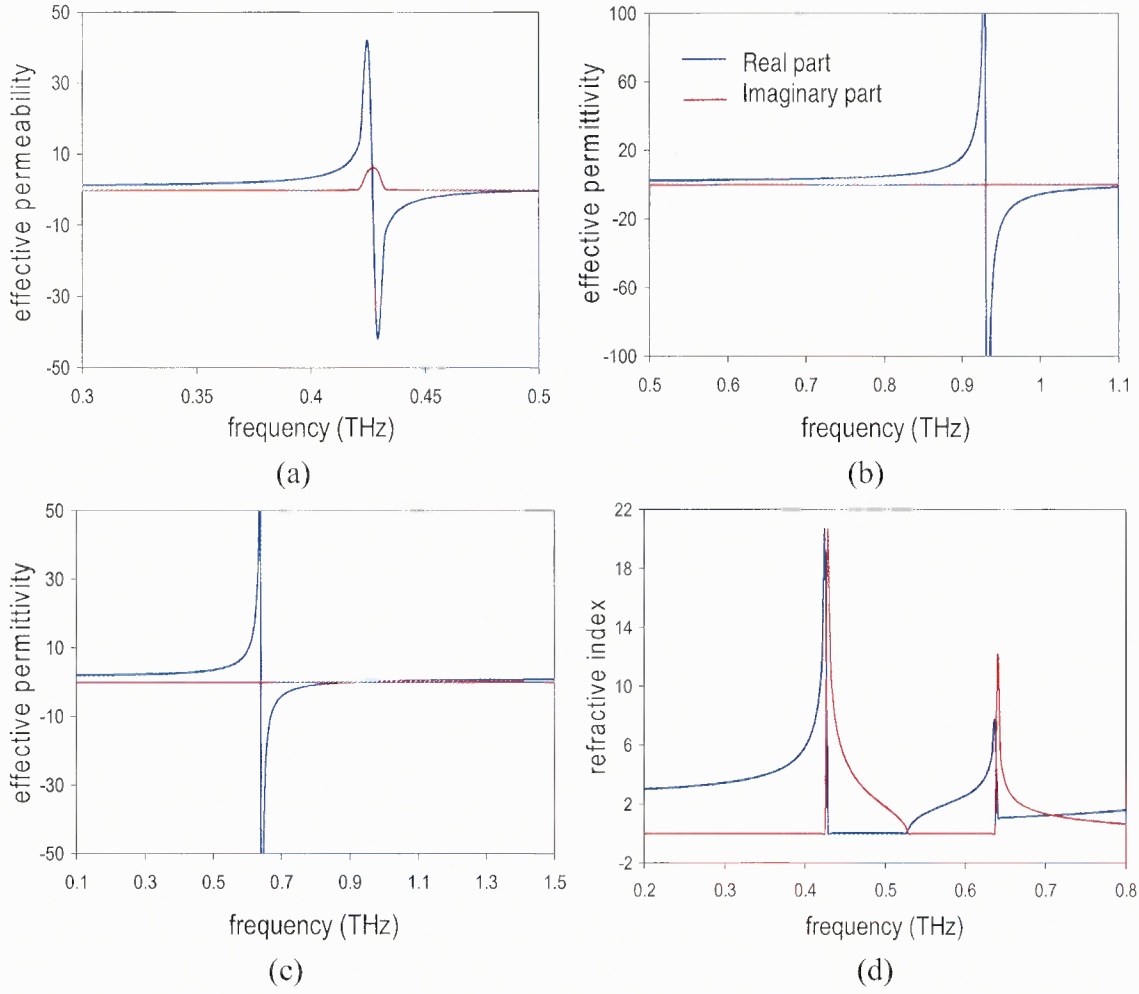

Figure 5.5 The simulation result of (a) effective permeability and (b) effective permittivity of SRR, (c) effective permittivity of break microstrips and (d) refractive index of 3D copper LHM.

5.2 FEMLAB's RF Module

The FEM has been increasingly used for numerical computation of electromagnetic propagation and scattering simulation in the terahertz region[96] as well as on the optical region[97]. The use of unstructured meshes and isoparametric triangular elements offer superior versatility in modeling complex geometries and allows the user to accurately model curvilinear geometries. Several approaches for the analysis of dispersive medium using FEM have been proposed[98,99,100].

In this section, the simulation is performed using a commercial finite element solver, FEMLAB's RF module. The RF Module is a COMSOL Multiphysics™ package for analysis and solve problem of general field electromagnetics waves such as RF and microwave applications, optics, and photonics using FEM methods. The application modes included in the package are fully multiphysics enabled which extends the modeling environment with customized interfaces and functionality optimized. The underlying equations for electromagnetics are available in the application modes adding unique feature to COMSOL Multiphysics, making nonstandard modeling easily accessible.

The Figure 5.6 shows 3D pattern of the electric field norm distribution of resonance mode for the 2D composite structure of 10 ×10 copper SRR obtains from RF module FEMLAB. For simplicity, the simulation was performed in 2D approach where the copper SRR array, with element parameter as shown in Table 5.1, was laid on the xy-plane. The result shows there is a resonance peak fall at 0.6THz. This value, however, does not match with both previous calculation using Excel add-on and experimental data. This is perhaps due to large tolerance error occurred when the coarse mesh parameter was applied in the simulation works. The accuracy is expected to increase when finer meshes are exploited.

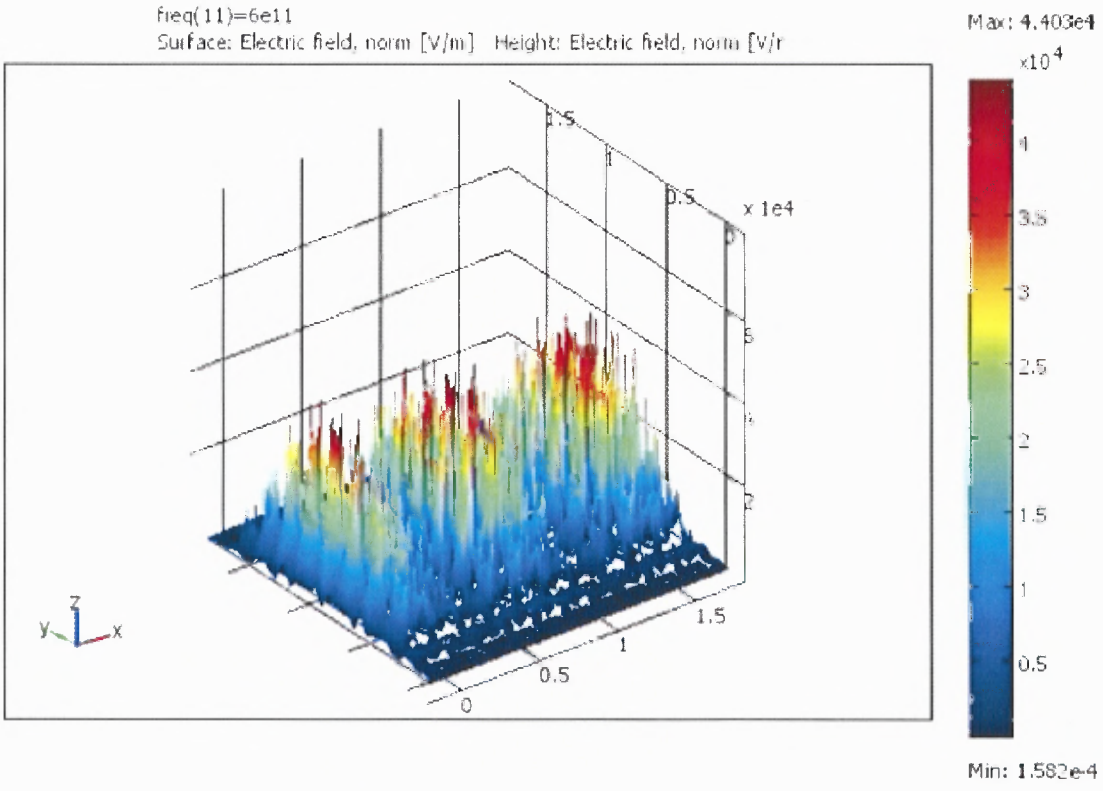

Figure 5.6 3D pattern of the electric field norm distribution of resonance mode for the 2D composite structure of 10×10 copper SRR obtains from RF module FEMLAB. The color bar indicates the normalized scale in V/m.

Figure 5.7 shows the simulation of copper SRR in 3D approach. The result shows that there is a major resonance peak fall at 0.4THz and a small resonance peak 0.8THz. The simulation result in this model has proven to match with the experimental and previous calculation using Excel add-in. However, since the run time in this simulation is very large and also consumes large RAM and cache memory, simulation in fine step size of frequencies and fine meshes size are unable to perform. A better machine is needed for accurate simulation.

freq(1)=1e11
Slice: Electric field, norm [V/m]

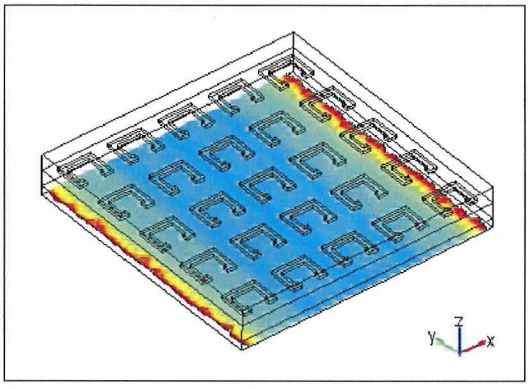

freq(2)=2e11
Slice: Electric field, norm [V/m]

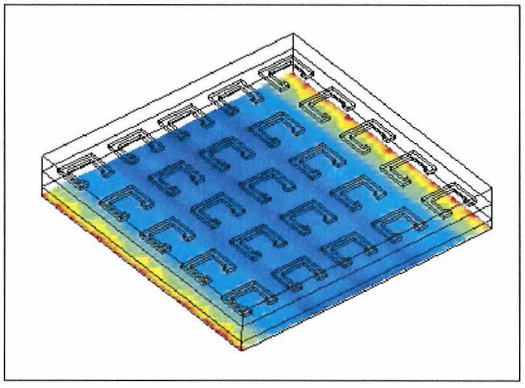

Max: 5.40
5
4.5
4
3.5
3
2.5
2
1.5
1
0.5
0
Min: 0

freq(3)=3e11
Slice: Electric field, norm [V/m]

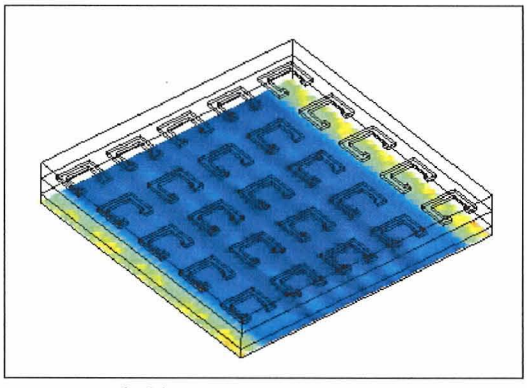

freq(4)=4e11
Slice: Electric field, norm [V/m]

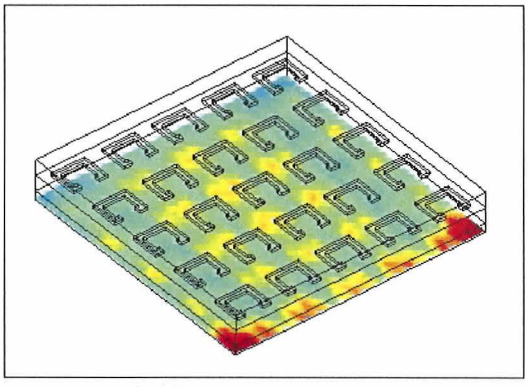

freq(5)=5e11
Slice: Electric field, norm [V/m]

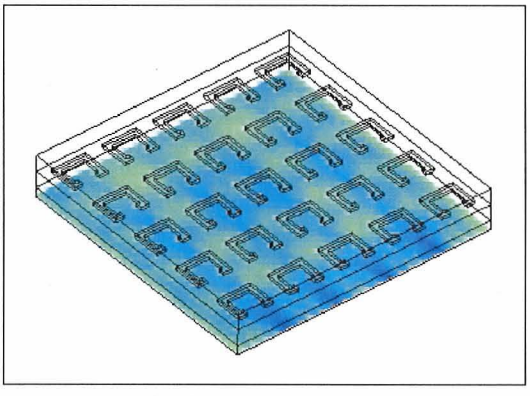

freq(6)=6e11
Slice: Electric field, norm [V/m]

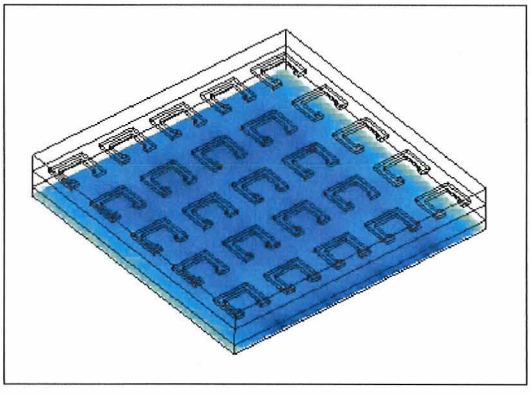

freq(7)=7e11
Slice: Electric field, norm [V/m]

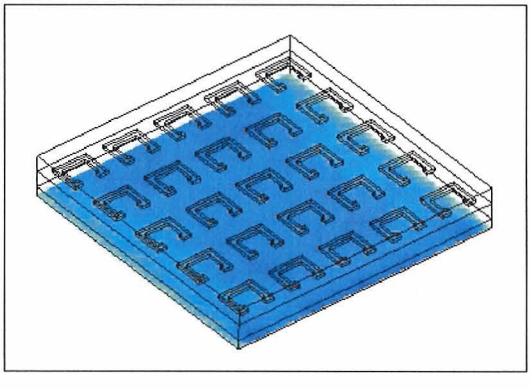

freq(8)=8e11
Slice: Electric field, norm [V/m]

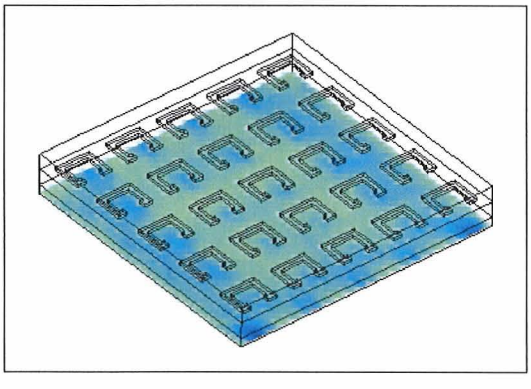

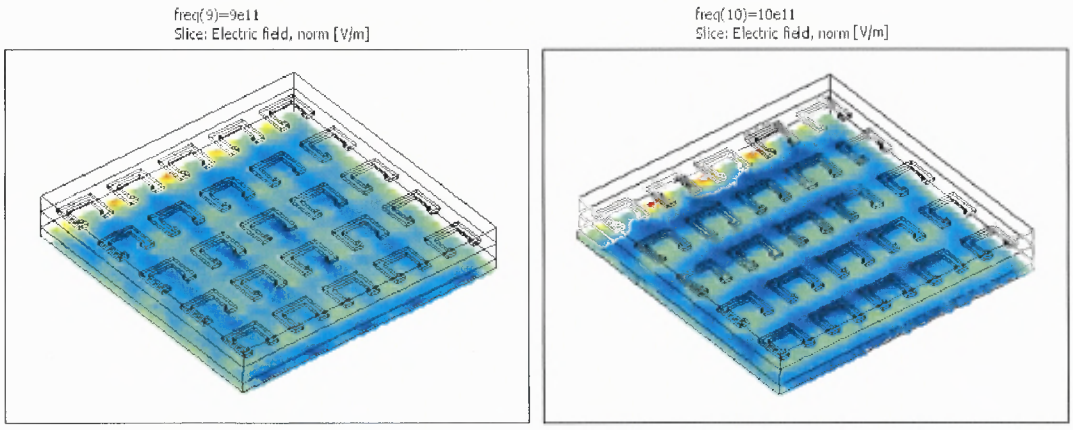

Figure 5.7 Surface plot of normalized Electric field from frequencies 0.1 to 1THz. Resonance frequencies is showed at 0.4 and 0.8THz. The color bar indicates the scale in V/m.

All the simulations were performed on an Intel Centrino Coretm 2 Duo Processor at frequency 1.66GHz, 1.99GB of RAM memory. The total simulation process time for 2D model was approximately 90 minutes for frequency of 0.1 to 1 THz with steps size of 0.05THz. For 3D model, the run time is approximately 2 hours with frequencies in step size 0.1THz. Also, due to the limitation of the machine, the LHM structure with both combination of SRR and microstrips are unable to perform. Both simulation codes are listed in Appendix B.

CHAPTER 6

CONCLUSION AND FUTURE WORK

6.1 Conclusion

The concept of MTMs is based on the effective-medium assumption. The unit cell of a periodic structure has dimensions significantly smaller than the probing wavelength so the medium is described as homogeneous medium. In our experimental condition, the frequency range is from 0.1 THz to 1 THz is equivalent to 3000μm to 300μm where our sample lattice size is satisfying this restriction.

The fabrication of 2D and 3D THz MTMs are successfully fabricated using microfluidic-jetted fabrication. The size of the 2D sample is approximately 80μm with thickness of 2.4 μm fabricated using PEDOT: PSS. However, this sample showed no significant absorbance peak in the characterization result under investigation using THz-TDS in frequencies range of 0.1 to 2.3 THz. This is mainly due to the low conductivity of the sample, as proved in the simulation result. Conductivity may increase by increasing the number of deposited layers, which in other words, increase the thickness of the sample. However, increasing deposited thickness caused fluidic smear and the feature was unable to recognizable. So far, sample thickness of 2.4μm is the maximum fabrication thickness for this PEDOT: PSS sample. As conclusion, although the feature size of 1/8 of the incident wavelength was clearly achieved, the transmission effects are relatively diffuse, and consequently difficult to characterize.

In using the DDT-AuNPs as fabrication medium, obviously, the conductivity is far better then PEDOT: PSS. But structure fabricated in this fluidic suffered poor

resolution. Only with lattice size up to 180μm of SRR structure was successfully fabricated. The idea of stacking layers not only increases the conductivity of the sample but also reduces the lattice length in z-direction thereby making 3D LH MTMs feasible. Thus, for this sample, an absorbance peak is observed near 0.18THz under investigate of THz-TDS, although the amplitude of absorbance peak is relatively low. The low absorbance amplitude can be explained: in this structure range of p/λ=1/5 to 1/8, although refraction is dominating, diffraction/scattering effects tend to alter the purity of refractive effects and increase the transmission losses. In addition, simulation results are not exact but are consider closed to the experimental results and the retrieved refraction index is −1.6 at 0.15THz.

The copper samples were fabricated by a combination of a microfluidic-jetted technique and a typical PCB etching technique. MTMs fabricated using this combination technique was first discover and realized by the author. These samples gave promisingly high conductivity thus consequently to very sharp absorbance peaks under characterization of THz-TDS. Copper SRR sample exhibited magnetic resonance leading to negative permeability at 0.43THz and plasmonic resonances leading to negative permittivity at 0.98THz while copper break-microstrips exhibited plasmonic resonances at 0.68THz. The simulation results have successfully given a good agreement with the experimental results. But unfortunately, due to the geometry parameters of the break-microstrips structure, the combination of the copper SRR and break-microstrips does not yield a negative refractive index. Extra work is needed to solve this problem in the future as well as improving the sample feature resolution.

6.2 Future Work

MTMs have rapidly developed in these past few years. It is not possible to report on all of their current developments or to predict all of their future directions and applications. However in this chapter, a few idea and research will discuss and added to important challenges and potential future work for MTMs.

6.2.1 Improve Resolution of the Structure

The average lattice size p in the fabricated samples is still electromagnetically too large for high-quality refraction. As mention in the section above, the diffraction/scattering effects tend to alter the purity of refractive effects and increase the transmission losses for structure size of 1/4 to 1/8 although the refraction is dominant. In order to obtain pure refractive phenomena without order losses, it is necessary to decrease the structure feature by one order of magnitude or more. Once that challenge is met, MTMs will behave as atoms in natural materials to produce a perfectly homogeneous macroscopic response., The atomic lattice constant of natural material such as water is in the order of a few angstroms, therefore, it is in order of one thousand of millions smaller then the incident terahertz wavelength ($p/\lambda \sim 10^{-8}$), which ensures a perfectly homogeneous response to electromagnetic waves. A decrease of p/λ in MTMs from ~1/10 to 1/100 would be sufficient to obtain good refraction, since scattering would become completely negligible. This seems to represent a real challenge as much more electric and magnetic energy needs to be stored in a much smaller volume.

PEDOT: PSS is a perfect fluidic for fine spot size deposition but it is suffer from low conductivity. However, a 3D structure with reduce lattice constant is can be

fabricated using this fluidic and the conductivity can be increased by stacking more dielectric layers with SRR or microstrips deposited on each layers.

6.2.2 Conductivity Improve

The PEDOT: PSS 2D MTMs that are fabricated using microfluidic-jetted techniques discussed in Chapter 3 have low conductivity (below 1 S/cm) even though the size has met the 1/10 of incident wavelength. Toluene based DDT-AuNPs has higher conductivity then PEDOT: PSS. However, since the deposited drop diameter is relatively large compare to PEDOT: PSS, it is failed to fabricate small features lower then 180μm.

Alternative material needs to be explored for better conductivity as well as able to minimize the drop spot. Recent development of water based DDT-AuNPs in has found to match these conditions, it has the same conductivity and a larger surface tension for fine size deposition. Thus, this water based DDT-AuNPs is expected as a potential fluidic for THz MTMs fabrication.

Mixing CNT in PEDOT: PSS has proved to enhance the conductivity of the fluidic[101]. Also, recently research observed that the conductivity of PEDOT: PSS films can be enhanced by adding polyalcohols (alcohols with more than two OH groups on the molecule) or high dielectric solvents, such as methyl sulfoxide (DMSO) and N,Ndimethylformamide into the PEDOT: PSS solution.

6.2.3 Active Metamaterials

Active MTMs is an unexplored field to date. It is predicted that novel active applications will soon emerge from the new paradigm of MTMs. My future exploration, active MTMs will be fabricated with semiconductor polymers as a light active media for MTMs fabrication.

Fluidic semiconductor polymers act as conductors when exposed to light by electron-hole pair excitation. PEDOT: PSS is originally a conducting material without excitation light due to the surface charge of the polymer. However, the conductivity is increase when photo-excited electron-hole pairs optically injected into the semiconductor polymer[102].

THz-TDS pump probe technique[103] was carried out on active MTM sample to demonstrate the active charge response of the medium. This method is no different from typical THz-TDS unless an argon laser is added to the system as an excitation source as shown in Figure 6.1.

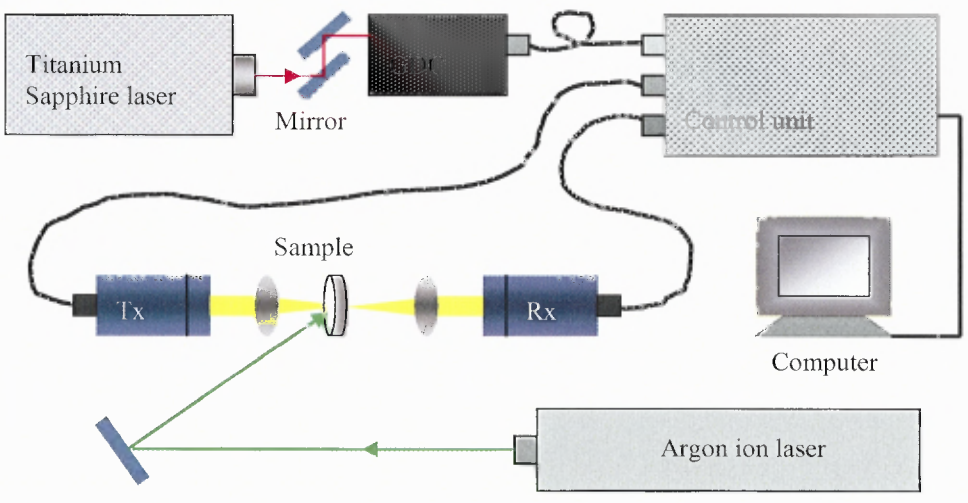

Figure 6.1: THz-TDS pump probe technique setup.

Another active MTMs propose is the voltage active MTMs. The structure is LHM MTMs with microstrips connect to the AC or DC voltage as shown in Figure 6.2. The SRR structure is deposited using high conductivity material such as gold or carbon nanotube fluidic whereas the microstrips are deposited using semiconductor polymer fluidic. When current apply to the rod wire, semiconductor material will act as conductor and the overall structure forms a LH medium due to the incident waves. In the case with

no current apply; the structure will act as SRR since the semiconductor has low absorption to the THz waves.

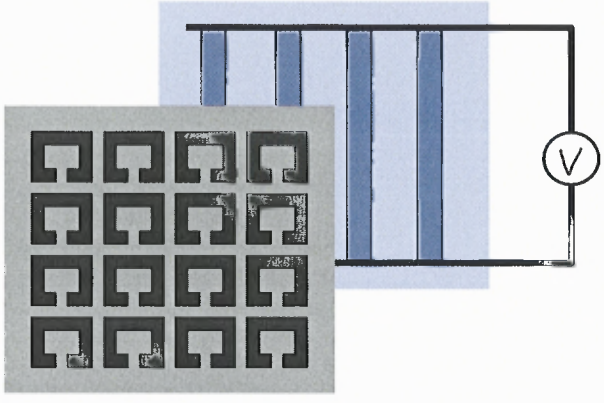

Figure 6.2 The illustrated diagram of future active LH MTMs with both end of the rod connect to the AC or DC voltage.

6.2.4 Gradient or Step Negative Refraction Index THz MTMs

SRR exhibit a magnetic response that increases linearly as a function of inverse gap spacing where capacitance $C \propto \frac{1}{d_g}$, d_g is gap spacing. This idea of varying SRR gap spacing would be a precursor to the design gradient or step index MTMs. In addition, since the microfluidic-jetted technique provides a relatively easy procedure for material fabrication added potential for this device to be fabricated. The gradient or step negative refraction material is feasible using the idea of stacking layers to form 3D structure. The experiment to confirm the gradient negative refraction index is observing the refracted beam on the planer slab of MTMs. The beams will acquire different phase advances as they propagated through the slab.

APPENDIX A

FABRICATION SUMMARY

The following appendix includes the summary of the fabrication steps of the samples.

1. Substrate Preparation

1. Cut into size.
2. Pre-cleaned with acetone, followed with isopropanol rinses.
3. Boiled with distilled water mix with three drops of cleaning agent D-91 for 60 minutes.
4. Followed with 60 minutes ultrasonic bath.

2. Deposited Fluidic Preparation

Table A.1 List of Solvent, Manufactures, Formulation for Deposited Fluidic

Fluidic	PEDOT: PSS	DDT-AuNPs	Liquid polyimide
solvent	Water based	Toluene based	Pyralin thinner
manufacturer	H. C. Starck	Sigma-Aldrich	HD MicroSystems
Formulation	1	1	2
Filtration (μm)	0.2	none	none
Ultrasonic time (min)	15	15	30

1. Original from manufacturer
2. Ratio of fluidic to solvent =1:8 parts.

3. Design Layout

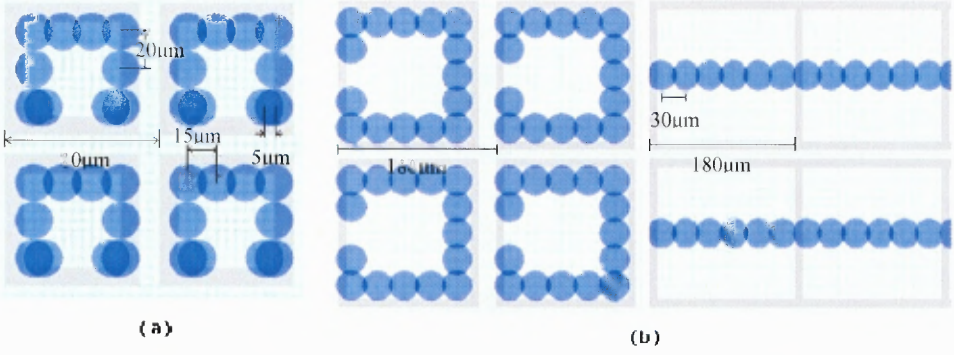

Figure A.1 deposited pattern for (a) 80μm lattice size SRR for PEDOT: PSS samples. And, (b) LHM with lattice size of 180μm for DDT-AuNPs and Cu samples.

4. Cartridge Setting

Table A.2 List of Cartridge Setting of Fluidic Used

Fluidic	PEDOT: PSS	DDT-AuNPs	Liquid polyimide
Jetting voltage (V)	11-13	15-17	19-21
Meniscus pressure (inchesH_2O)	1-2	4-4.5	3
Print height (mm)	0.6	0.6	0.6
Nozzle temperature (^oC)	30	28	28

Table A.3 Cleaning Cycle and Idle Setting for Microfluidic Deposition

	Task	Time	Frequency (kHz)	Delay (s)
Cleaning cycle	Spit	100-200ms	2	1
	Purge	2-4s	-	1
	Spit	300-500ms	2	1
	blot	1-2s	-	-
Idle	Spit	100ms	1.5	2

5. Waveform Setting

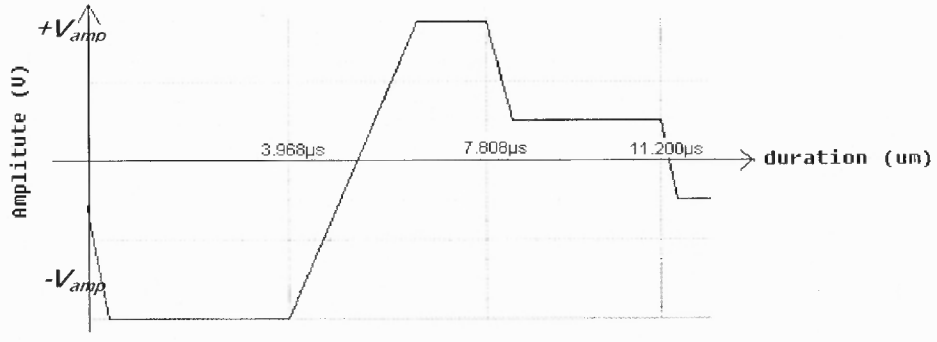

(a)

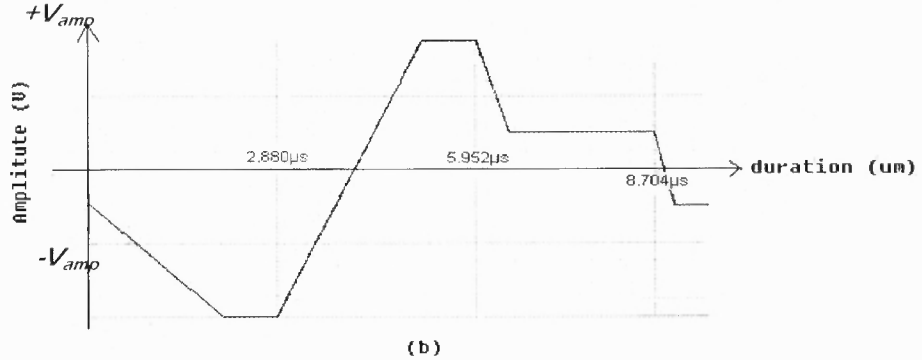

(b)

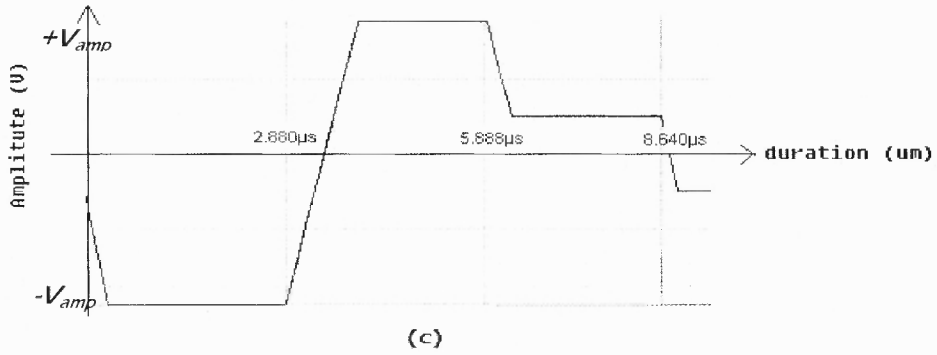

Figure A.2 Waveform setting of (a) PEDOT: PSS and (b) DDT-AuNPs solution. (c) Liquid polyimide. V_{amp} for PEDOT: PSS was 11-13V, DDT-AuNPs was 15-17V and for polyimide was 19-21V.

7. Curing

Table A.4 List of Curing Properties of Fluidic Used

Fluidic	PEDOT: PSS	DDT-AuNPs	Liquid polyimide
Temperature (°C)	100-120	30-60	160
Time (minutes)	30	20-30	15-30

8. Etching (Copper Samples only)

Samples were etched under commercial etchant for ~4 minutes.

APPENDIX B

COMSOL MODEL REPORT I

The following appendix includes the generated reports of COMSOL Multiphysics™ package FEMLAB's RF module simulation of 2D model Copper SRR sample and 3D model Copper SRR.

2D model Cu SRR

1. Table of Contents

2. Model Properties

Property	Value
Model name	2D model Cu SRR
Author	Yew Li Hor
Company	
Department	
Reference	
URL	
Saved date	Oct 28, 2008 10:57:33 AM
Creation date	Oct 28, 2008 9:41:29 AM
COMSOL version	COMSOL 3.3.0.511

Application modes and modules used in this model: Geom1 (2D)
In-Plane TM Waves (RF Module)

3. Geometry

Number of geometries: 1

3.1. Geom1

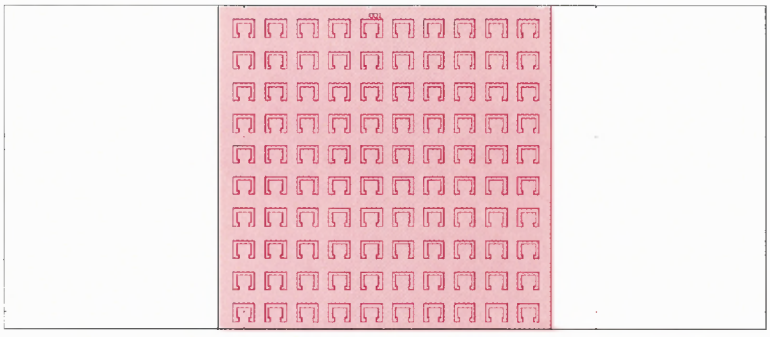

3.1.1. Point mode

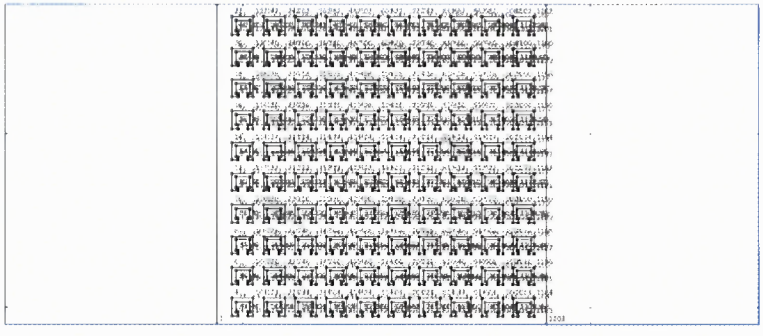

3.1.2. Boundary mode

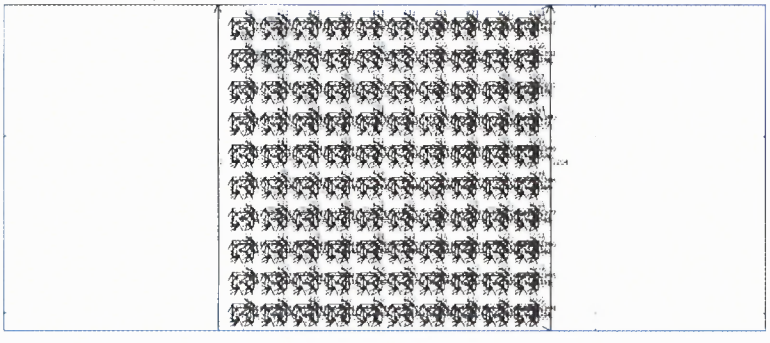

3.1.3. Subdomain mode

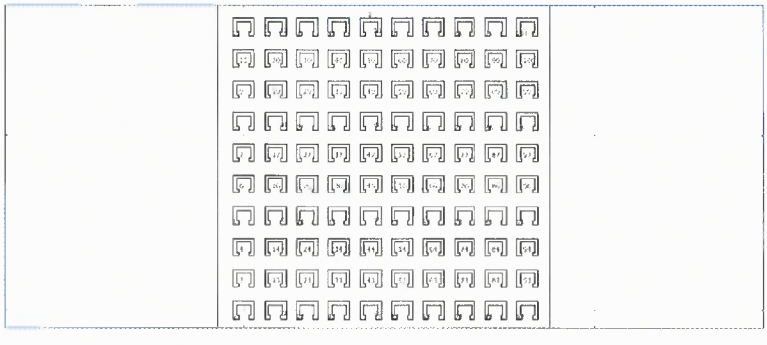

4. Geom1

Space dimensions: 2D
Independent variables: x, y, z

4.1. Mesh

4.1.1. Mesh Statistics

Number of degrees of freedom	78689
Number of mesh points	19713
Number of elements	39264
Triangular	39264
Quadrilateral	0
Number of boundary elements	3860
Number of vertex elements	1204
Minimum element quality	0.55
Element area ratio	0.002

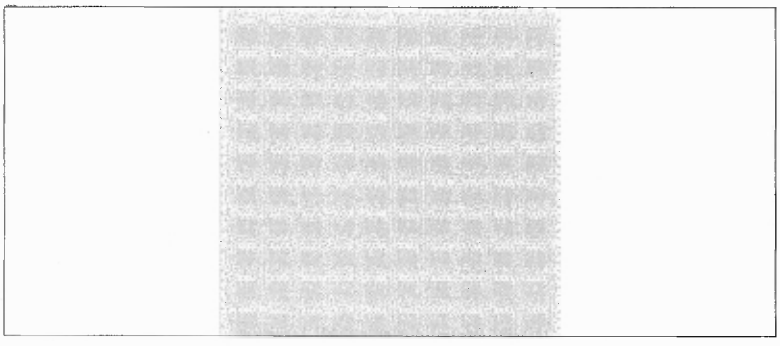

4.2. Application Mode: In-Plane TM Waves (rfweh)
Application mode type: In-Plane TM Waves (RF Module)
Application mode name: rfweh

4.2.1. Scalar Variables

Name	Variable	Value	Description
epsilon0	epsilon0_rfweh	8.854187817e-12	Permittivity of vacuum
mu0	mu0_rfweh	4*pi*1e-7	Permeability of vacuum
nu	nu_rfweh	freq	Frequency
H0iz	H0iz_rfweh	exp(-j*k0_rfweh*x)	Incident magnetic field, z component

4.2.2. Application Mode Properties

Property	Value
Default element type	Lagrange - Quadratic
Analysis type	Harmonic propagation
Field type	Scattered TM waves
Specify wave using	Frequency
Specify eigenvalues using	Eigenfrequency
Divergence condition	Off
Symmetry plane x=0	Off
Symmetry type for x=0	Symmetry
Symmetry plane y=0	Off
Symmetry type for y=0	Symmetry
Frame	Frame (ref)
Weak constraints	Off
Vector element constraint	Off

4.2.3. Variables
Dependent variables: Ez, Hz, Ax, Ay, Az, scEz, scHz, psi
Shape functions: shlag(2,'scHz')
Interior boundaries not active

5. Materials / Coefficients Library

5.1. Cu

Parameter	Value
Heat capacity (C)	384[J/(kg*K)]
Young's modulus (E)	120e9[Pa]
Thermal expansion coeff. (alpha)	16.5e-6[1/K]
Thermal conductivity (k)	401[W/(m*K)]
Poisson's ratio (nu)	0.34
Density (rho)	8960[kg/m^3]
Electrical conductivity (sigma)	58.1e6[S/m]

6. Solver Settings

Solve using a script: off

Analysis type	Harmonic_propagation
Auto select solver	On
Solver	Parametric
Solution form	Automatic
Symmetric	auto
Adaption	Off

6.1. Direct (UMFPACK). Solver type: Linear system solver

Parameter	Value
Pivot threshold	0.1
Memory allocation factor	0.7

6.2. Advanced

Parameter	Value
Constraint handling method	Elimination
Null-space function	Automatic
Assembly block size	5000
Use Hermitian transpose of constraint matrix and in symmetry detection	Off
Use complex functions with real input	Off
Stop if error due to undefined operation	On
Type of scaling	Automatic
Manual scaling	
Row equilibration	On
Manual control of reassembly	Off
Load constant	On
Constraint constant	On
Mass constant	On
Damping (mass) constant	On
Jacobian constant	On
Constraint Jacobian constant	On

7. Postprocessing

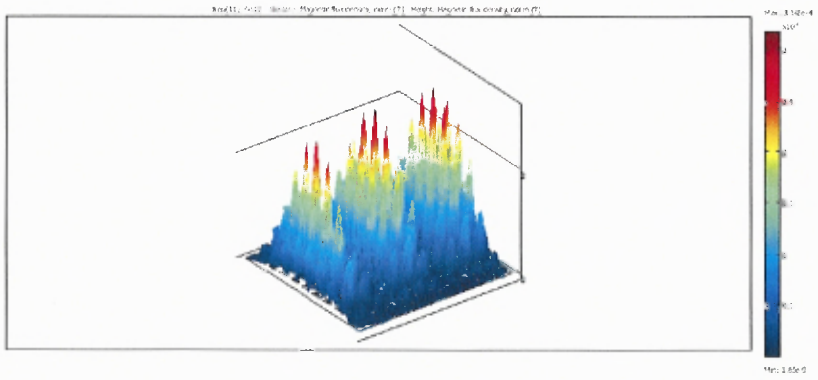

8. Variables

8.1. Boundary

Name	Description	Expression
Hiz_rfweh	Incident magnetic field	H0iz_rfweh
dVolbnd_rfweh	Area integration contribution	1
Qsj1_rfweh	Surface current source_term	0
nPoav_rfweh	Power outflow, time average	nx_rfweh * Poxav_rfweh+ny_rfweh * Poyav_rfweh
tHscz_rfweh	H-field in Stratton-Chu formula, z component	scHz
tEscx_rfweh	E-field in Stratton-Chu formula, x component	scEx_rfweh
tEscy_rfweh	E-field in Stratton-Chu formula, y component	scEy_rfweh
Z_TE_rfweh	Wave impedance, TE waves	omega_rfweh * mu_rfweh/betaport_rfweh
Z_TM_rfweh	Wave impedance, TM waves	betaport_rfweh/(omega_rfweh * epsilon_rfweh)
Z_TEM_rfweh	Wave impedance, TEM waves	sqrt(mu_rfweh/epsilon_rfweh)
Pin_port_rfweh	Port power level for the inport	Pport_rfweh

8.2. Subdomain

8.2.1. Subdomain 1

Name	Description	Expression
dr_guess_rfweh	Width in radial direction default guess	0
R0_guess_rfweh	Inner radius default guess	0
SR_rfweh	PML radial coordinate	
Sx_rfweh	PML x coordinate	x
Sdx_guess_rfweh	Width in x direction default guess	0
rCylx_rfweh	PML r cylindrical vector, x component	
srcpntx_guess_rfweh	Source point default guess, x component	0

Sy_rfweh	PML y coordinate	y
Sdy_guess_rfweh	Width in y direction default guess	0
rCyly_rfweh	PML r cylindrical vector, y component	
srcpnty_guess_rfweh	Source point default guess, y component	0
detJ_rfweh	PML transformation matrix determinant	1
Jxx_rfweh	PML transformation matrix, element xx	1
invJxx_rfweh	PML inverse transformation matrix, element xx	1
Jxy_rfweh	PML transformation matrix, element xy	0
invJxy_rfweh	PML inverse transformation matrix, element xy	0
Jyx_rfweh	PML transformation matrix, element yx	0
invJyx_rfweh	PML inverse transformation matrix, element yx	0
Jyy_rfweh	PML transformation matrix, element yy	1
invJyy_rfweh	PML inverse transformation matrix, element yy	1
k_rfweh	Wave number	k0_rfweh * sqrt(mur_rfweh * (epsilonr_rfweh+sigma_rfweh/(jomega_rfweh * epsilon0_rfweh)))
c_rfweh	Phase velocity	c0_rfweh/sqrt(epsilonr_rfweh * mur_rfweh)
Z_wave_rfweh	Wave impedance	c_rfweh * mu0_rfweh * mur_rfweh
delta_rfweh	Skin depth	1/(omega_rfweh * sqrt(0.5 * mu0_rfweh * mur_rfweh * epsilon0_rfweh * epsilonr_rfweh * (-1+sqrt(1+(sigma_rfweh/(omega_rfweh * epsilon0_rfweh * epsilonr_rfweh))^2))))
dVol_rfweh	Volume integration contribution	detJ_rfweh
Hiz_rfweh	Incident magnetic field	H0iz_rfweh
curlHx_rfweh	Curl of magnetic field, x component	scHzy
curlHy_rfweh	Curl of magnetic field, y component	diff(-scHz,x)
depHz_rfweh	Magnetic field test variable, z component	scHz
Hz	Magnetic field, z component	scHz+Hiz_rfweh
epsilon_rfweh	Permittivity	epsilon0_rfweh * epsilonr_rfweh
epsilonxx_rfweh	Permittivity, xx component	epsilon0_rfweh * epsilonrxx_rfweh

epsilonxy_rfweh	Permittivity, xy component	epsilon0_rfweh * epsilonrxy_rfweh
epsilonyx_rfweh	Permittivity, yx component	epsilon0_rfweh * epsilonryx_rfweh
epsilonyy_rfweh	Permittivity, yy component	epsilon0_rfweh * epsilonryy_rfweh
mu_rfweh	Permeability	mu0_rfweh * mur_rfweh
Dx_rfweh	Electric displacement, x component	epsilonxx_rfweh * Ex_rfweh+epsilonxy_rfweh * Ey_rfweh
scDx_rfweh	Scattered electric displacement, x component	epsilonxx_rfweh * scEx_rfweh+epsilonxy_rfweh * scEy_rfweh
Jdx_rfweh	Displacement current density, x component	jomega_rfweh * Dx_rfweh
Jix_rfweh	Induced current density, x component	sigmaxx_rfweh * Ex_rfweh+sigmaxy_rfweh * Ey_rfweh
Ex_rfweh	Electric field, x component	jwEx_rfweh/jomega_rfweh
jwEx_rfweh	Electric field, x component, times jω	(curlHx_rfweh+diff(Hiz_rfweh,y))/(epsilonr_rfweh * epsilon0_rfweh)
scEx_rfweh	Scattered electric field, x component	scHzy/(epsilonr_rfweh * epsilon0_rfweh * jomega_rfweh)
Eix_rfweh	Incident electric field, x component	diff(Hiz_rfweh,y)/(epsilonr_rfweh * jomega_rfweh * epsilon0_rfweh)
Dy_rfweh	Electric displacement, y component	epsilonyx_rfweh * Ex_rfweh+epsilonyy_rfweh * Ey_rfweh
scDy_rfweh	Scattered electric displacement, y component	epsilonyx_rfweh * scEx_rfweh+epsilonyy_rfweh * scEy_rfweh
Jdy_rfweh	Displacement current density, y component	jomega_rfweh * Dy_rfweh
Jiy_rfweh	Induced current density, y component	sigmayx_rfweh * Ex_rfweh+sigmayy_rfweh * Ey_rfweh
Ey_rfweh	Electric field, y component	jwEy_rfweh/jomega_rfweh
jwEy_rfweh	Electric field, y component, times jω	(curlHy_rfweh+diff(-Hiz_rfweh,x))/(epsilonr_rfweh * epsilon0_rfweh)
scEy_rfweh	Scattered electric field, y component	-scHzx/(epsilonr_rfweh * epsilon0_rfweh * jomega_rfweh)
Eiy_rfweh	Incident electric field, y component	diff(-Hiz_rfweh,x)/(epsilonr_rfweh * jomega_rfweh * epsilon0_rfweh)
Bz_rfweh	Magnetic flux density, z component	mu_rfweh * Hz
scBz_rfweh	Scattered magnetic flux density, z component	mu_rfweh * scHz
normH_rfweh	Magnetic field, norm	abs(Hz)
normB_rfweh	Magnetic flux density, norm	abs(Bz_rfweh)
normscH_rfweh	Scattered magnetic field, norm	abs(scHz)
normscB_rfweh	Scattered magnetic	abs(scBz_rfweh)

	flux density, norm	
normE_rfweh	Electric field, norm	sqrt(abs(Ex_rfweh)^2+abs(Ey_rfweh)^2)
normD_rfweh	Electric displacement, norm	sqrt(abs(Dx_rfweh)^2+abs(Dy_rfweh)^2)
normscE_rfweh	Scattered electric field, norm	sqrt(abs(scEx_rfweh)^2+abs(scEy_rfweh)^2)
normscD_rfweh	Scattered electric displacement, norm	sqrt(abs(scDx_rfweh)^2+abs(scDy_rfweh)^2)
normPoav_rfweh	Power flow, time average, norm	sqrt(abs(Poxav_rfweh)^2+abs(Poyav_rfweh)^2)
Wmav_rfweh	Magnetic energy density, time average	0.25 * real(Hz * conj(Bz_rfweh))
Weav_rfweh	Electric energy density, time average	0.25 * real(Ex_rfweh * conj(Dx_rfweh)+Ey_rfweh * conj(Dy_rfweh))
Wav_rfweh	Total energy density, time average	Wmav_rfweh+Weav_rfweh
Qav_rfweh	Resistive heating, time average	0.5 * real(sigmaxx_rfweh * Ex_rfweh * conj(Ex_rfweh)+sigmaxy_rfweh * Ey_rfweh * conj(Ex_rfweh)-j * real(omega_rfweh) * Ex_rfweh * conj(Dx_rfweh)+sigmayx_rfweh * Ex_rfweh * conj(Ey_rfweh)+sigmayy_rfweh * Ey_rfweh * conj(Ey_rfweh)-j * real(omega_rfweh) * Ey_rfweh * conj(Dy_rfweh))
Poxav_rfweh	Power flow, time average, x component	0.5 * real(Ey_rfweh * conj(Hz))
Poyav_rfweh	Power flow, time average, y component	0.5 * real(-Ex_rfweh * conj(Hz))

8.2.2. Subdomain 2-101

Name	Description	Expression
dr_guess_rfweh	Width in radial direction default guess	0
R0_guess_rfweh	Inner radius default guess	0
SR_rfweh	PML radial coordinate	
Sx_rfweh	PML x coordinate	x
Sdx_guess_rfweh	Width in x direction default guess	0
rCylx_rfweh	PML r cylindrical vector, x component	
srcpntx_guess_rfweh	Source point default guess, x component	0
Sy_rfweh	PML y coordinate	y
Sdy_guess_rfweh	Width in y direction default guess	0
rCyly_rfweh	PML r cylindrical vector, y component	
srcpnty_guess_rfweh	Source point default guess, y component	0
detJ_rfweh	PML transformation matrix determinant	1
Jxx_rfweh	PML transformation matrix, element xx	1

invJxx_rfweh	PML inverse transformation matrix, element xx	1
Jxy_rfweh	PML transformation matrix, element xy	0
invJxy_rfweh	PML inverse transformation matrix, element xy	0
Jyx_rfweh	PML transformation matrix, element yx	0
invJyx_rfweh	PML inverse transformation matrix, element yx	0
Jyy_rfweh	PML transformation matrix, element yy	1
invJyy_rfweh	PML inverse transformation matrix, element yy	1
k_rfweh	Wave number	k0_rfweh * sqrt(mur_rfweh * (epsilonr_rfweh+sigma_rfweh/(jomega_rfweh * epsilon0_rfweh)))
c_rfweh	Phase velocity	c0_rfweh/sqrt(epsilonr_rfweh * mur_rfweh)
Z_wave_rfweh	Wave impedance	c_rfweh * mu0_rfweh * mur_rfweh
delta_rfweh	Skin depth	1/(omega_rfweh * sqrt(0.5 * mu0_rfweh * mur_rfweh * epsilon0_rfweh * epsilonr_rfweh * (-1+sqrt(1+(sigma_rfweh/(omega_rfweh * epsilon0_rfweh * epsilonr_rfweh))^2))))
dVol_rfweh	Volume integration contribution	detJ_rfweh
Hiz_rfweh	Incident magnetic field	H0iz_rfweh
curlHx_rfweh	Curl of magnetic field, x component	scHzy
curlHy_rfweh	Curl of magnetic field, y component	diff(-scHz,x)
depHz_rfweh	Magnetic field test variable, z component	scHz
Hz	Magnetic field, z component	scHz+Hiz_rfweh
epsilon_rfweh	Permittivity	epsilon0_rfweh * epsilonr_rfweh
epsilonxx_rfweh	Permittivity, xx component	epsilon0_rfweh * epsilonrxx_rfweh
epsilonxy_rfweh	Permittivity, xy component	epsilon0_rfweh * epsilonrxy_rfweh
epsilonyx_rfweh	Permittivity, yx component	epsilon0_rfweh * epsilonryx_rfweh
epsilonyy_rfweh	Permittivity, yy component	epsilon0_rfweh * epsilonryy_rfweh
mu_rfweh	Permeability	mu0_rfweh * mur_rfweh
Dx_rfweh	Electric displacement, x component	epsilonxx_rfweh * Ex_rfweh+epsilonxy_rfweh * Ey_rfweh
scDx_rfweh	Scattered electric displacement, x component	epsilonxx_rfweh * scEx_rfweh+epsilonxy_rfweh * scEy_rfweh
Jdx_rfweh	Displacement current density, x component	jomega_rfweh * Dx_rfweh
Jix_rfweh	Induced current density, x component	sigmaxx_rfweh * Ex_rfweh+sigmaxy_rfweh * Ey_rfweh

Ex_rfweh	Electric field, x component	jwEx_rfweh/jomega_rfweh
jwEx_rfweh	Electric field, x component, times jω	(curlHx_rfweh+diff(Hiz_rfweh,y))/((epsilonr_rfweh+sigma_rfweh/(jomega_rfweh * epsilon0_rfweh)) * epsilon0_rfweh)
scEx_rfweh	Scattered electric field, x component	scHzy/((epsilonr_rfweh+sigma_rfweh/(jomega_rfweh * epsilon0_rfweh)) * epsilon0_rfweh * jomega_rfweh)
Eix_rfweh	Incident electric field, x component	diff(Hiz_rfweh,y)/((epsilonr_rfweh+sigma_rfweh/(jomega_rfweh * epsilon0_rfweh)) * jomega_rfweh * epsilon0_rfweh)
Dy_rfweh	Electric displacement, y component	epsilonyx_rfweh * Ex_rfweh+epsilonyy_rfweh * Ey_rfweh
scDy_rfweh	Scattered electric displacement, y component	epsilonyx_rfweh * scEx_rfweh+epsilonyy_rfweh * scEy_rfweh
Jdy_rfweh	Displacement current density, y component	jomega_rfweh * Dy_rfweh
Jiy_rfweh	Induced current density, y component	sigmayx_rfweh * Ex_rfweh+sigmayy_rfweh * Ey_rfweh
Ey_rfweh	Electric field, y component	jwEy_rfweh/jomega_rfweh
jwEy_rfweh	Electric field, y component, times jω	(curlHy_rfweh+diff(-Hiz_rfweh,x))/((epsilonr_rfweh+sigma_rfweh/(jomega_rfweh * epsilon0_rfweh)) * epsilon0_rfweh)
scEy_rfweh	Scattered electric field, y component	-scHzx/((epsilonr_rfweh+sigma_rfweh/(jomega_rfweh * epsilon0_rfweh)) * epsilon0_rfweh * jomega_rfweh)
Eiy_rfweh	Incident electric field, y component	diff(-Hiz_rfweh,x)/((epsilonr_rfweh+sigma_rfweh/(jomega_rfweh * epsilon0_rfweh)) * jomega_rfweh * epsilon0_rfweh)
Bz_rfweh	Magnetic flux density, z component	mu_rfweh * Hz
scBz_rfweh	Scattered magnetic flux density, z component	mu_rfweh * scHz
normH_rfweh	Magnetic field, norm	abs(Hz)
normB_rfweh	Magnetic flux density, norm	abs(Bz_rfweh)
normscH_rfweh	Scattered magnetic field, norm	abs(scHz)
normscB_rfweh	Scattered magnetic flux density, norm	abs(scBz_rfweh)
normE_rfweh	Electric field, norm	sqrt(abs(Ex_rfweh)^2+abs(Ey_rfweh)^2)
normD_rfweh	Electric displacement, norm	sqrt(abs(Dx_rfweh)^2+abs(Dy_rfweh)^2)
normscE_rfweh	Scattered electric field, norm	sqrt(abs(scEx_rfweh)^2+abs(scEy_rfweh)^2)
normscD_rfweh	Scattered electric displacement, norm	sqrt(abs(scDx_rfweh)^2+abs(scDy_rfweh)^2)
normPoav_rfweh	Power flow, time average, norm	sqrt(abs(Poxav_rfweh)^2+abs(Poyav_rfweh)^2)
Wmav_rfweh	Magnetic energy density, time average	0.25 * real(Hz * conj(Bz_rfweh))
Weav_rfweh	Electric energy density, time average	0.25 * real(Ex_rfweh * conj(Dx_rfweh)+Ey_rfweh * conj(Dy_rfweh))
Wav_rfweh	Total energy density, time	Wmav_rfweh+Weav_rfweh

	average	
Qav_rfweh	Resistive heating, time average	0.5 * real(sigmaxx_rfweh * Ex_rfweh * conj(Ex_rfweh) +sigmaxy_rfweh * Ey_rfweh * conj(Ex_rfweh)-j * real(omega_rfweh) * Ex_rfweh * conj(Dx_rfweh) +sigmayx_rfweh * Ex_rfweh * conj(Ey_rfweh) +sigmayy_rfweh * Ey_rfweh * conj(Ey_rfweh)-j * real(omega_rfweh) * Ey_rfweh * conj(Dy_rfweh))
Poxav_rfweh	Power flow, time average, x component	0.5 * real(Ey_rfweh * conj(Hz))
Poyav_rfweh	Power flow, time average, y component	0.5 * real(-Ex_rfweh * conj(Hz))

COMSOL MODEL REPORT II

3D model Cu SRR

1. Table of Contents

2. Model Properties

Property	Value
Model name	3D model Cu SRR
Author	Yew Li Hor
Company	
Department	
Reference	
URL	
Saved date	Nov 5, 2008 4:57:38 PM
Creation date	Nov 4, 2008 1:16:29 PM
COMSOL version	COMSOL 3.3.0.511

Application modes and modules used in this model:Geom1 (3D)
Electromagnetic Waves (RF Module):Geom2 (2D)

3. Geometry

Number of geometries: 2

3.1. Geom1

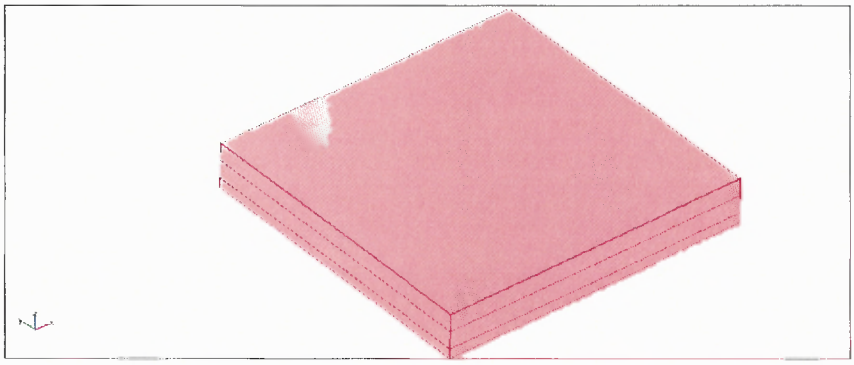

3.1.1. Point mode

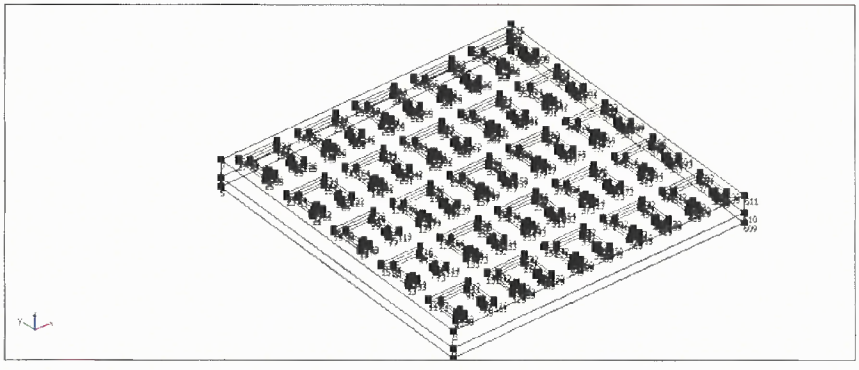

3.1.2. Edge mode

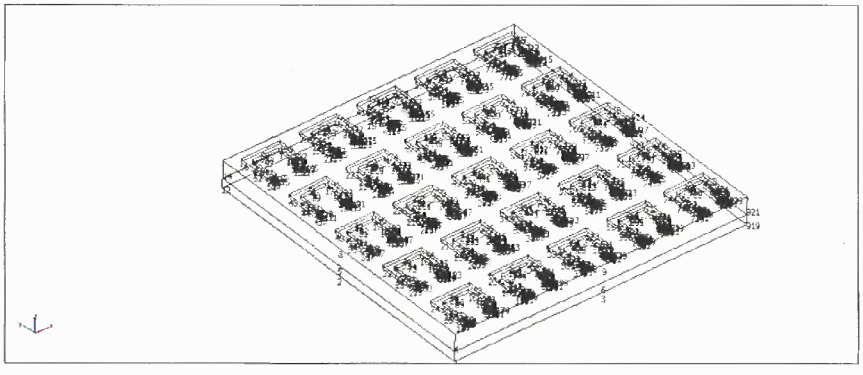

3.1.3. Boundary mode

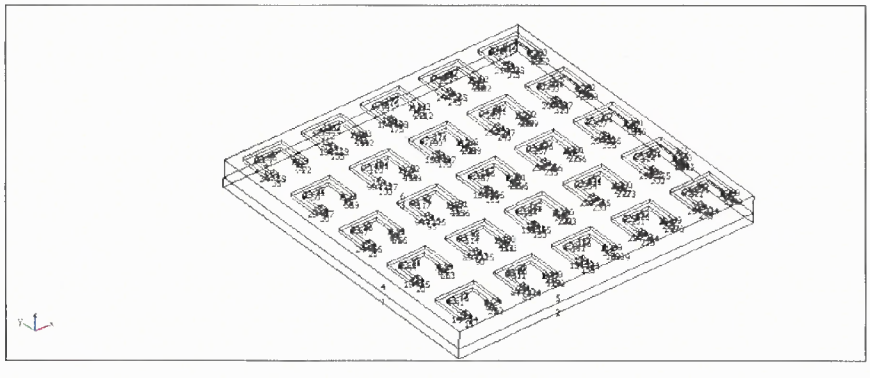

3.1.4. Subdomain mode

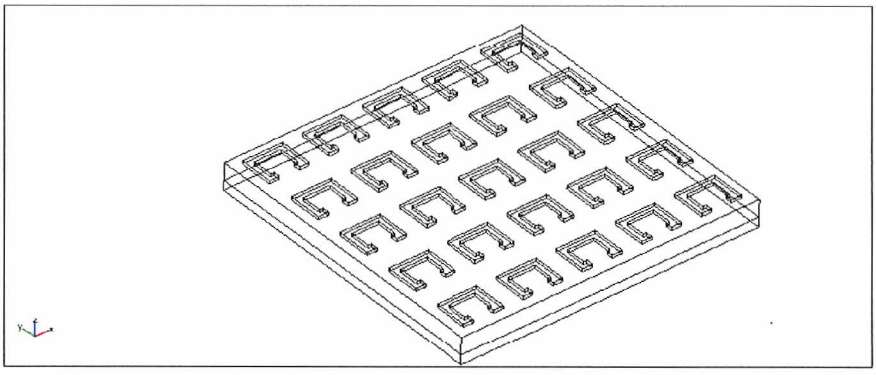

3.2 Geom2

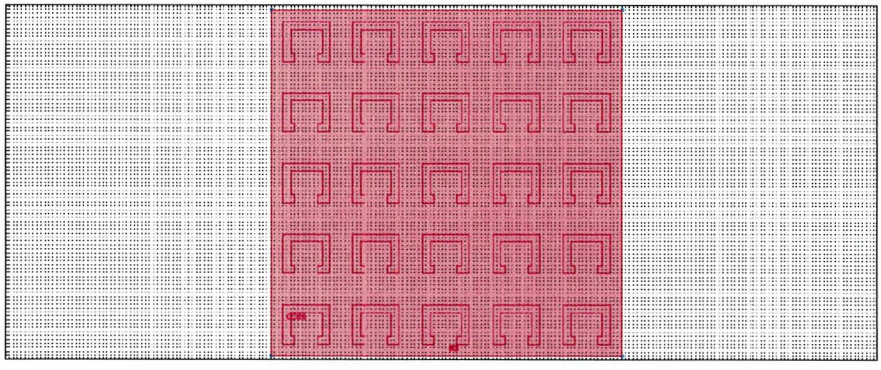

4. Geom1

Space dimensions: 3D
Independent variables: x, y, z

4.1. Mesh

4.1.1. Mesh Statistics

Number of degrees of freedom	288432
Number of mesh points	8114
Number of elements	44595
Tetrahedral	44595
Prism	0
Hexahedral	0
Number of boundary elements	10948
Triangular	10948
Quadrilateral	0
Number of edge elements	2230
Number of vertex elements	616
Minimum element quality	0.166
Element volume ratio	0.002

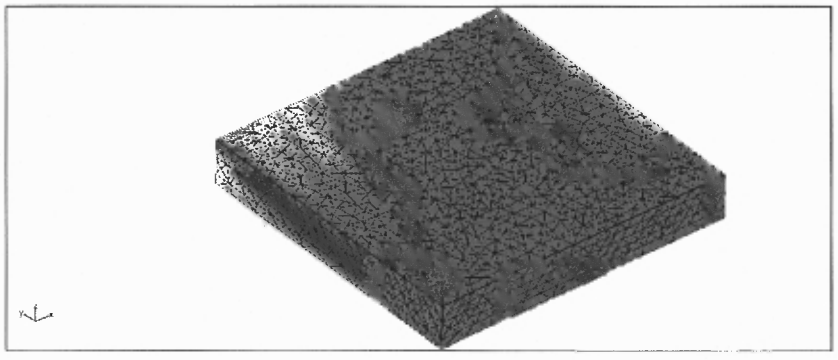

4.2. Application Mode: Electromagnetic Waves (rfw)
Application mode type: Electromagnetic Waves (RF Module)
Application mode name: rfw

4.2.1. Scalar Variables

Name	Variable	Value	Description
epsilon0	epsilon0_rfw	8.854187817e-12	Permittivity of vacuum
mu0	mu0_rfw	4*pi*1e-7	Permeability of vacuum
nu	nu_rfw	freq	Frequency
E0ix	E0ix_rfw	exp(-j*k0_rfw*z)	Incident electric field, x component
E0iy	E0iy_rfw	0	Incident electric field, y component
E0iz	E0iz_rfw	0	Incident electric field, z component
psi0	psi0_rfw	psi0_guess_rfw	Gauge fixing variable scaling

4.2.2. Application Mode Properties

Property	Value
Default element type	Vector - Quadratic
Analysis type	Harmonic propagation
Solve for	Scattered electric field
Specify wave using	Frequency
Specify eigenvalues using	Eigenfrequency
Divergence condition	Off
Symmetry plane x=0	Off
Symmetry type for x=0	Symmetry
Symmetry plane y=0	Off
Symmetry type for y=0	Symmetry
Symmetry plane z=0	Off
Symmetry type for z=0	Symmetry
Frame	Frame (ref)
Weak constraints	Off

4.2.3. Variables
Dependent variables: Ex, Ey, Ez, Hx, Hy, Hz, Ax, Ay, Az, scEx, scEy, scEz, scHx, scHy, scHz, psi
Shape functions: shcurl(2,{'scEx','scEy','scEz'}), shlag(2,'psi')
Interior boundaries not active

5. Geom2

Space dimensions: 2D
Independent variables: x, y, z

6. Materials/Coefficients Library

6.1. Cu

Parameter	Value
Heat capacity (C)	384[J/(kg*K)]
Young's modulus (E)	120e9[Pa]
Thermal expansion coeff. (alpha)	16.5e-6[1/K]
Thermal conductivity (k)	401[W/(m*K)]
Poisson's ratio (nu)	0.34
Density (rho)	8960[kg/m^3]
Electrical conductivity (sigma)	1e16[S/m]

7. Solver Settings

Solve using a script: off

Analysis type	Harmonic_propagation
Auto select solver	On
Solver	Parametric
Solution form	Automatic
Symmetric	auto
Adaption	Off

7.1. GMRES. Solver type: Linear system solver

Parameter	Value
Relative tolerance	1.0E-6
Factor in error estimate	400.0
Maximum number of iterations	10000
Number of iterations before restart	50
Preconditioning	Left

7.1.1. Geometric multigrid. Solver type: Preconditioner

Parameter	Value
Number of iterations	2
Multigrid cycle	V-cycle

7.1.1.1. SOR vector. Solver type: Presmoother

Parameter	Value
Number of iterations	2
Relaxation factor (omega)	1.0
Number of secondary iterations	2

7.1.1.2. SORU vector. Solver type: Postsmoother

Parameter	Value
Number of iterations	2
Relaxation factor (omega)	1.0
Number of secondary iterations	2

7.1.1.3. SPOOLES. Solver type: Coarse solver

Parameter	Value
Drop tolerance	0.0
Pivot threshold	0.1
Preordering algorithm	Minimum degree

7.2. Advanced

Parameter	Value
Constraint handling method	Elimination
Null-space function	Automatic
Assembly block size	5000
Use Hermitian transpose of constraint matrix and in symmetry detection	Off
Use complex functions with real input	Off
Stop if error due to undefined operation	On
Type of scaling	Automatic
Manual scaling	
Row equilibration	On
Manual control of reassembly	Off
Load constant	On
Constraint constant	On
Mass constant	On
Damping (mass) constant	On
Jacobian constant	On
Constraint Jacobian constant	On

8. Postprocessing

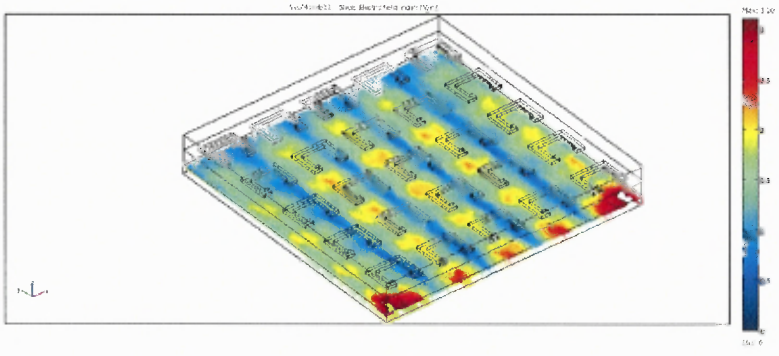

9. Variables

9.1. Boundary

Name	Description	Expression
Eix_rfw	Incident electric field	E0ix_rfw
Eiy_rfw	Incident electric field	E0iy_rfw
Eiz_rfw	Incident electric field	E0iz_rfw
tHx	Tangential magnetic field, x component	Hx-(nx_rfw * Hx+ny_rfw * Hy+nz_rfw * Hz) * nx_rfw
tscHx	Tangential scattered magnetic field, x component	scHx-(nx_rfw * scHx+ny_rfw * scHy+nz_rfw * scHz) * nx_rfw

tEx	Tangential electric field, x component	tscEx+Eix_rfw-(nx_rfw * Eix_rfw+ny_rfw * Eiy_rfw+nz_rfw * Eiz_rfw) * nx_rfw
tHy	Tangential magnetic field, y component	Hy-(nx_rfw * Hx+ny_rfw * Hy+nz_rfw * Hz) * ny_rfw
tscHy	Tangential scattered magnetic field, y component	scHy-(nx_rfw * scHx+ny_rfw * scHy+nz_rfw * scHz) * ny_rfw
tEy	Tangential electric field, y component	tscEy+Eiy_rfw-(nx_rfw * Eix_rfw+ny_rfw * Eiy_rfw+nz_rfw * Eiz_rfw) * ny_rfw
tHz	Tangential magnetic field, z component	Hz-(nx_rfw * Hx+ny_rfw * Hy+nz_rfw * Hz) * nz_rfw
tscHz	Tangential scattered magnetic field, z component	scHz-(nx_rfw * scHx+ny_rfw * scHy+nz_rfw * scHz) * nz_rfw
tEz	Tangential electric field, z component	tscEz+Eiz_rfw-(nx_rfw * Eix_rfw+ny_rfw * Eiy_rfw+nz_rfw * Eiz_rfw) * nz_rfw
dVolbnd_rfw	Area integration contribution	1
Qsj1_rfw	Surface current source_term	0
Qsj2_rfw	Surface current source_term	0
Qsj3_rfw	Surface current source_term	0
Jsx_rfw	Surface current density, x component	uny * (Hz_down-Hz_up)-unz * (Hy_down-Hy_up)
Jsy_rfw	Surface current density, y component	unz * (Hx_down-Hx_up)-unx * (Hz_down-Hz_up)
Jsz_rfw	Surface current density, z component	unx * (Hy_down-Hy_up)-uny * (Hx_down-Hx_up)
nPoav_rfw	Power outflow, time average	nx_rfw * Poxav_rfw+ny_rfw * Poyav_rfw+nz_rfw * Pozav_rfw
normJs_rfw	Surface current density, norm	sqrt(abs(Jsx_rfw)^2+abs(Jsy_rfw)^2+abs(Jsz_rfw)^2)
normtE_rfw	Tangential electric field, norm	sqrt(abs(tEx)^2+abs(tEy)^2+abs(tEz)^2)
normtH_rfw	Tangential magnetic field, norm	sqrt(abs(tHx)^2+abs(tHy)^2+abs(tHz)^2)
normtscE_rfw	Tangential scattered electric field, norm	sqrt(abs(tscEx)^2+abs(tscEy)^2+abs(tscEz)^2)
Qsav_rfw	Surface resistive heating, time average	0.5 * real(Jsx_rfw * conj(tEx)+Jsy_rfw * conj(tEy)+Jsz_rfw * conj(tEz))
tEscx_rfw	E-field in Stratton-Chu formula, x component	tscEx
tHscx_rfw	H-field in Stratton-Chu formula, x component	tscHx
tEscy_rfw	E-field in Stratton-Chu formula, y component	tscEy
tHscy_rfw	H-field in Stratton-Chu formula, y component	tscHy
tEscz_rfw	E-field in Stratton-Chu formula, z component	tscEz
tHscz_rfw	H-field in Stratton-Chu formula, z component	tscHz
Z_TE_rfw	Wave impedance, TE waves	omega_rfw * mu_rfw/beta_rfw
Z_TM_rfw	Wave impedance, TM waves	beta_rfw/(omega_rfw * epsilon_rfw)
Z_TEM_rfw	Wave impedance, TEM waves	sqrt(mu_rfw/epsilon_rfw)
Pin_port_rfw	Port power level for the inport	Pport_rfw

9.2. Subdomain
9.2.1. Subdomain 1-3

Name	Description	Expression
dr_guess_rfw	Width in radial direction default guess	0
R0_guess_rfw	Inner radius default guess	0
SR_rfw	PML radial coordinate	
Sx_rfw	PML x coordinate	x
Sdx_guess_rfw	Width in x direction default guess	0
rCylx_rfw	PML r cylindrical vector, x component	
srcpntx_guess_rfw	Source point default guess, x component	0
Sy_rfw	PML y coordinate	y
Sdy_guess_rfw	Width in y direction default guess	0
rCyly_rfw	PML r cylindrical vector, y component	
srcpnty_guess_rfw	Source point default guess, y component	0
Sz_rfw	PML z coordinate	z
Sdz_guess_rfw	Width in z direction default guess	0
rCylz_rfw	PML r cylindrical vector, z component	
srcpntz_guess_rfw	Source point default guess, z component	0
detJ_rfw	PML transformation matrix determinant	1
Jxx_rfw	PML transformation matrix, element xx	1
invJxx_rfw	PML inverse transformation matrix, element xx	1
Jxy_rfw	PML transformation matrix, element xy	0
invJxy_rfw	PML inverse transformation matrix, element xy	0
Jxz_rfw	PML transformation matrix, element xz	0
invJxz_rfw	PML inverse transformation matrix, element xz	0
Jyx_rfw	PML transformation matrix, element yx	0
invJyx_rfw	PML inverse transformation matrix, element yx	0
Jyy_rfw	PML transformation matrix, element yy	1
invJyy_rfw	PML inverse transformation matrix, element yy	1
Jyz_rfw	PML transformation matrix, element yz	0
invJyz_rfw	PML inverse transformation matrix, element yz	0

Jzx_rfw	PML transformation matrix, element zx	0
invJzx_rfw	PML inverse transformation matrix, element zx	0
Jzy_rfw	PML transformation matrix, element zy	0
invJzy_rfw	PML inverse transformation matrix, element zy	0
Jzz_rfw	PML transformation matrix, element zz	1
invJzz_rfw	PML inverse transformation matrix, element zz	1
k_rfw	Wave number	k0_rfw * sqrt(mur_rfw * (epsilonr_rfw+sigma_rfw/(jomega_rfw * epsilon0_rfw)))
c_rfw	Phase velocity	c0_rfw/sqrt(epsilonr_rfw * mur_rfw)
Z_wave_rfw	Wave impedance	c_rfw * mu0_rfw * mur_rfw
delta_rfw	Skin depth	1/(omega_rfw * sqrt(0.5 * mu0_rfw * mur_rfw * epsilon0_rfw * epsilonr_rfw * (-1+sqrt(1+(sigma_rfw/(omega_rfw * epsilon0_rfw * epsilonr_rfw))^2))))
dVol_rfw	Volume integration contribution	detJ_rfw
Eix_rfw	Incident electric field	E0ix_rfw
Eiy_rfw	Incident electric field	E0iy_rfw
Eiz_rfw	Incident electric field	E0iz_rfw
epsilon_rfw	Permittivity	epsilon0_rfw * epsilonr_rfw
epsilonxx_rfw	Permittivity, xx component	epsilon0_rfw * epsilonrxx_rfw
epsilonxy_rfw	Permittivity, xy component	epsilon0_rfw * epsilonrxy_rfw
epsilonxz_rfw	Permittivity, xz component	epsilon0_rfw * epsilonrxz_rfw
epsilonyx_rfw	Permittivity, yx component	epsilon0_rfw * epsilonryx_rfw
epsilonyy_rfw	Permittivity, yy component	epsilon0_rfw * epsilonryy_rfw
epsilonyz_rfw	Permittivity, yz component	epsilon0_rfw * epsilonryz_rfw
epsilonzx_rfw	Permittivity, zx component	epsilon0_rfw * epsilonrzx_rfw
epsilonzy_rfw	Permittivity, zy component	epsilon0_rfw * epsilonrzy_rfw
epsilonzz_rfw	Permittivity, zz component	epsilon0_rfw * epsilonrzz_rfw
mu_rfw	Permeability	mu0_rfw * mur_rfw
muxx_rfw	Permeability, xx component	mu0_rfw * murxx_rfw
muxy_rfw	Permeability, xy component	mu0_rfw * murxy_rfw
muxz_rfw	Permeability, xz component	mu0_rfw * murxz_rfw
muyx_rfw	Permeability, yx component	mu0_rfw * muryx_rfw
muyy_rfw	Permeability, yy component	mu0_rfw * muryy_rfw
muyz_rfw	Permeability, yz component	mu0_rfw * muryz_rfw
muzx_rfw	Permeability, zx component	mu0_rfw * murzx_rfw
muzy_rfw	Permeability, zy component	mu0_rfw * murzy_rfw
muzz_rfw	Permeability, zz component	mu0_rfw * murzz_rfw
curlEx_rfw	Curl of electric field, x component	scEzyscEyz
depEx_rfw	Electric field test variable, x component	scEx
Dx_rfw	Electric displacement, x component	epsilonxx_rfw * Ex

scDx_rfw	Scattered electric displacement, x component	epsilonxx_rfw * scEx
Jdx_rfw	Displacement current density, x component	jomega_rfw * Dx_rfw
Jix_rfw	Induced current density, x component	0
Gfx_rfw	Gauge fixed field, x component	Bx_rfw/mu0_rfw
jwHx_rfw	Magnetic field, x component, times jω	jwBx_rfw/mu_rfw
Ex	Electric field, x component	scEx+Eix_rfw
Hx	Magnetic field, x component	jwHx_rfw/jomega_rfw
Hix_rfw	Incident magnetic field, x component	-(diff(Eiz_rfw,y)-diff(Eiy_rfw,z))/(jomega_rfw * mu_rfw)
scHx	Scattered magnetic field, x component	scBx_rfw/mu_rfw
jwBx_rfw	Magnetic flux density, x component, times jω	-curlEx_rfw-diff(Eiz_rfw,y)+diff(Eiy_rfw,z)
Bx_rfw	Magnetic flux density, x component	jwBx_rfw/jomega_rfw
scBx_rfw	Scattered magnetic flux density, x component	-scEzyscEyz/jomega_rfw
curlEy_rfw	Curl of electric field, y component	scExzscEzx
depEy_rfw	Electric field test variable, y component	scEy
Dy_rfw	Electric displacement, y component	epsilonyy_rfw * Ey
scDy_rfw	Scattered electric displacement, y component	epsilonyy_rfw * scEy
Jdy_rfw	Displacement current density, y component	jomega_rfw * Dy_rfw
Jiy_rfw	Induced current density, y component	0
Gfy_rfw	Gauge fixed field, y component	By_rfw/mu0_rfw
jwHy_rfw	Magnetic field, y component, times jω	jwBy_rfw/mu_rfw
Ey	Electric field, y component	scEy+Eiy_rfw
Hy	Magnetic field, y component	jwHy_rfw/jomega_rfw
Hiy_rfw	Incident magnetic field, y component	-(diff(Eix_rfw,z)-diff(Eiz_rfw,x))/(jomega_rfw * mu_rfw)
scHy	Scattered magnetic field, y component	scBy_rfw/mu_rfw
jwBy_rfw	Magnetic flux density, y component, times jω	-curlEy_rfw-diff(Eix_rfw,z)+diff(Eiz_rfw,x)
By_rfw	Magnetic flux density, y component	jwBy_rfw/jomega_rfw
scBy_rfw	Scattered magnetic flux density, y component	-scExzscEzx/jomega_rfw
curlEz_rfw	Curl of electric field, z component	scEyxscExy
depEz_rfw	Electric field test variable, z component	scEz
Dz_rfw	Electric displacement, z component	epsilonzz_rfw * Ez
scDz_rfw	Scattered electric displacement, z component	epsilonzz_rfw * scEz
Jdz_rfw	Displacement current density, z	jomega_rfw * Dz_rfw

	component	
Jiz_rfw	Induced current density, z component	0
Gfz_rfw	Gauge fixed field, z component	Bz_rfw/mu0_rfw
jwHz_rfw	Magnetic field, z component, times jω	jwBz_rfw/mu_rfw
Ez	Electric field, z component	scEz+Eiz_rfw
Hz	Magnetic field, z component	jwHz_rfw/jomega_rfw
Hiz_rfw	Incident magnetic field, z component	-(diff(Eiy_rfw,x)-diff(Eix_rfw,y))/(jomega_rfw * mu_rfw)
scHz	Scattered magnetic field, z component	scBz_rfw/mu_rfw
jwBz_rfw	Magnetic flux density, z component, times jω	-curlEz_rfw-diff(Eiy_rfw,x)+diff(Eix_rfw,y)
Bz_rfw	Magnetic flux density, z component	jwBz_rfw/jomega_rfw
scBz_rfw	Scattered magnetic flux density, z component	-scEyxscExy/jomega_rfw
normE_rfw	Electric field, norm	sqrt(abs(Ex)^2+abs(Ey)^2+abs(Ez)^2)
normD_rfw	Electric displacement, norm	sqrt(abs(Dx_rfw)^2+abs(Dy_rfw)^2+abs(Dz_rfw)^2)
normB_rfw	Magnetic flux density, norm	sqrt(abs(Bx_rfw)^2+abs(By_rfw)^2+abs(Bz_rfw)^2)
normH_rfw	Magnetic field, norm	sqrt(abs(Hx)^2+abs(Hy)^2+abs(Hz)^2)
normPoav_rfw	Power flow, time average, norm	sqrt(abs(Poxav_rfw)^2+abs(Poyav_rfw)^2+abs(Pozav_rfw)^2)
normscE_rfw	Scattered electric field, norm	sqrt(abs(scEx)^2+abs(scEy)^2+abs(scEz)^2)
normscD_rfw	Scattered electric displacement, norm	sqrt(abs(scDx_rfw)^2+abs(scDy_rfw)^2+abs(scDz_rfw)^2)
normscB_rfw	Scattered magnetic flux density, norm	sqrt(abs(scBx_rfw)^2+abs(scBy_rfw)^2+abs(scBz_rfw)^2)
normscH_rfw	Scattered magnetic field, norm	sqrt(abs(scHx)^2+abs(scHy)^2+abs(scHz)^2)
Wmav_rfw	Magnetic energy density, time average	0.25 * real(Hx * conj(Bx_rfw)+Hy * conj(By_rfw)+Hz * conj(Bz_rfw))
Weav_rfw	Electric energy density, time average	0.25 * real(Ex * conj(Dx_rfw)+Ey * conj(Dy_rfw)+Ez * conj(Dz_rfw))
Wav_rfw	Total energy density, time average	Wmav_rfw+Weav_rfw
Qav_rfw	Resistive heating, time average	0.5 * real(Jix_rfw * conj(Ex)-j * real(omega_rfw) * Ex * conj(Dx_rfw)+Jiy_rfw * conj(Ey)-j * real(omega_rfw) * Ey * conj(Dy_rfw)+Jiz_rfw * conj(Ez)-j * real(omega_rfw) * Ez * conj(Dz_rfw))
Poxav_rfw	Power flow, time average, x component	0.5 * real(Ey * conj(Hz)-Ez * conj(Hy))
Poyav_rfw	Power flow, time average, y component	0.5 * real(Ez * conj(Hx)-Ex * conj(Hz))
Pozav_rfw	Power flow, time average, z component	0.5 * real(Ex * conj(Hy)-Ey * conj(Hx))

9.2.2. Subdomain 4-28

Name	Description	Expression
dr_guess_rfw	Width in radial direction default guess	0
R0_guess_rfw	Inner radius default guess	0
SR_rfw	PML radial coordinate	
Sx_rfw	PML x coordinate	x

Sdx_guess_rfw	Width in x direction default guess	0
rCylx_rfw	PML r cylindrical vector, x component	
srcpntx_guess_rfw	Source point default guess, x component	0
Sy_rfw	PML y coordinate	y
Sdy_guess_rfw	Width in y direction default guess	0
rCyly_rfw	PML r cylindrical vector, y component	
srcpnty_guess_rfw	Source point default guess, y component	0
Sz_rfw	PML z coordinate	z
Sdz_guess_rfw	Width in z direction default guess	0
rCylz_rfw	PML r cylindrical vector, z component	
srcpntz_guess_rfw	Source point default guess, z component	0
detJ_rfw	PML transformation matrix determinant	1
Jxx_rfw	PML transformation matrix, element xx	1
invJxx_rfw	PML inverse transformation matrix, element xx	1
Jxy_rfw	PML transformation matrix, element xy	0
invJxy_rfw	PML inverse transformation matrix, element xy	0
Jxz_rfw	PML transformation matrix, element xz	0
invJxz_rfw	PML inverse transformation matrix, element xz	0
Jyx_rfw	PML transformation matrix, element yx	0
invJyx_rfw	PML inverse transformation matrix, element yx	0
Jyy_rfw	PML transformation matrix, element yy	1
invJyy_rfw	PML inverse transformation matrix, element yy	1
Jyz_rfw	PML transformation matrix, element yz	0
invJyz_rfw	PML inverse transformation matrix, element yz	0
Jzx_rfw	PML transformation matrix, element zx	0
invJzx_rfw	PML inverse transformation matrix, element zx	0
Jzy_rfw	PML transformation matrix, element zy	0
invJzy_rfw	PML inverse transformation matrix, element zy	0

Jzz_rfw	PML transformation matrix, element zz	1
invJzz_rfw	PML inverse transformation matrix, element zz	1
k_rfw	Wave number	k0_rfw * sqrt(mur_rfw * (epsilonr_rfw+sigma_rfw/(jomega_rfw * epsilon0_rfw)))
c_rfw	Phase velocity	c0_rfw/sqrt(epsilonr_rfw * mur_rfw)
Z_wave_rfw	Wave impedance	c_rfw * mu0_rfw * mur_rfw
delta_rfw	Skin depth	1/(omega_rfw * sqrt(0.5 * mu0_rfw * mur_rfw * epsilon0_rfw * epsilonr_rfw * (-1+sqrt(1+(sigma_rfw/(omega_rfw * epsilon0_rfw * epsilonr_rfw))^2))))
dVol_rfw	Volume integration contribution	detJ_rfw
Eix_rfw	Incident electric field	E0ix_rfw
Eiy_rfw	Incident electric field	E0iy_rfw
Eiz_rfw	Incident electric field	E0iz_rfw
epsilon_rfw	Permittivity	epsilon0_rfw * epsilonr_rfw
epsilonxx_rfw	Permittivity, xx component	epsilon0_rfw * epsilonrxx_rfw
epsilonxy_rfw	Permittivity, xy component	epsilon0_rfw * epsilonrxy_rfw
epsilonxz_rfw	Permittivity, xz component	epsilon0_rfw * epsilonrxz_rfw
epsilonyx_rfw	Permittivity, yx component	epsilon0_rfw * epsilonryx_rfw
epsilonyy_rfw	Permittivity, yy component	epsilon0_rfw * epsilonryy_rfw
epsilonyz_rfw	Permittivity, yz component	epsilon0_rfw * epsilonryz_rfw
epsilonzx_rfw	Permittivity, zx component	epsilon0_rfw * epsilonrzx_rfw
epsilonzy_rfw	Permittivity, zy component	epsilon0_rfw * epsilonrzy_rfw
epsilonzz_rfw	Permittivity, zz component	epsilon0_rfw * epsilonrzz_rfw
mu_rfw	Permeability	mu0_rfw * mur_rfw
muxx_rfw	Permeability, xx component	mu0_rfw * murxx_rfw
muxy_rfw	Permeability, xy component	mu0_rfw * murxy_rfw
muxz_rfw	Permeability, xz component	mu0_rfw * murxz_rfw
muyx_rfw	Permeability, yx component	mu0_rfw * muryx_rfw
muyy_rfw	Permeability, yy component	mu0_rfw * muryy_rfw
muyz_rfw	Permeability, yz component	mu0_rfw * muryz_rfw
muzx_rfw	Permeability, zx component	mu0_rfw * murzx_rfw
muzy_rfw	Permeability, zy component	mu0_rfw * murzy_rfw
muzz_rfw	Permeability, zz component	mu0_rfw * murzz_rfw
curlEx_rfw	Curl of electric field, x component	scEzyscEyz
depEx_rfw	Electric field test variable, x component	scEx
Dx_rfw	Electric displacement, x component	epsilonxx_rfw * Ex
scDx_rfw	Scattered electric displacement, x component	epsilonxx_rfw * scEx
Jdx_rfw	Displacement current density, x component	jomega_rfw * Dx_rfw
Jix_rfw	Induced current density, x component	sigmaxx_rfw * Ex
Gfx_rfw	Gauge fixed field, x component	Bx_rfw/mu0_rfw
jwHx_rfw	Magnetic field, x component, times jω	jwBx_rfw/mu_rfw
Ex	Electric field, x component	scEx+Eix_rfw

Hx	Magnetic field, x component	jwHx_rfw/jomega_rfw
Hix_rfw	Incident magnetic field, x component	-(diff(Eiz_rfw,y)-diff(Eiy_rfw,z))/(jomega_rfw * mu_rfw)
scHx	Scattered magnetic field, x component	scBx_rfw/mu_rfw
jwBx_rfw	Magnetic flux density, x component, times jω	-curlEx_rfw-diff(Eiz_rfw,y)+diff(Eiy_rfw,z)
Bx_rfw	Magnetic flux density, x component	jwBx_rfw/jomega_rfw
scBx_rfw	Scattered magnetic flux density, x component	-scEzyscEyz/jomega_rfw
curlEy_rfw	Curl of electric field, y component	scExzscEzx
depEy_rfw	Electric field test variable, y component	scEy
Dy_rfw	Electric displacement, y component	epsilonyy_rfw * Ey
scDy_rfw	Scattered electric displacement, y component	epsilonyy_rfw * scEy
Jdy_rfw	Displacement current density, y component	jomega_rfw * Dy_rfw
Jiy_rfw	Induced current density, y component	sigmayy_rfw * Ey
Gfy_rfw	Gauge fixed field, y component	By_rfw/mu0_rfw
jwHy_rfw	Magnetic field, y component, times jω	jwBy_rfw/mu_rfw
Ey	Electric field, y component	scEy+Eiy_rfw
Hy	Magnetic field, y component	jwHy_rfw/jomega_rfw
Hiy_rfw	Incident magnetic field, y component	-(diff(Eix_rfw,z)-diff(Eiz_rfw,x))/(jomega_rfw * mu_rfw)
scHy	Scattered magnetic field, y component	scBy_rfw/mu_rfw
jwBy_rfw	Magnetic flux density, y component, times jω	-curlEy_rfw-diff(Eix_rfw,z)+diff(Eiz_rfw,x)
By_rfw	Magnetic flux density, y component	jwBy_rfw/jomega_rfw
scBy_rfw	Scattered magnetic flux density, y component	-scExzscEzx/jomega_rfw
curlEz_rfw	Curl of electric field, z component	scEyxscExy
depEz_rfw	Electric field test variable, z component	scEz
Dz_rfw	Electric displacement, z component	epsilonzz_rfw * Ez
scDz_rfw	Scattered electric displacement, z component	epsilonzz_rfw * scEz
Jdz_rfw	Displacement current density, z component	jomega_rfw * Dz_rfw
Jiz_rfw	Induced current density, z component	sigmazz_rfw * Ez
Gfz_rfw	Gauge fixed field, z component	Bz_rfw/mu0_rfw
jwHz_rfw	Magnetic field, z component, times jω	jwBz_rfw/mu_rfw
Ez	Electric field, z component	scEz+Eiz_rfw
Hz	Magnetic field, z component	jwHz_rfw/jomega_rfw
Hiz_rfw	Incident magnetic field, z component	-(diff(Eiy_rfw,x)-diff(Eix_rfw,y))/(jomega_rfw * mu_rfw)
scHz	Scattered magnetic field, z component	scBz_rfw/mu_rfw
jwBz_rfw	Magnetic flux density, z component, times jω	-curlEz_rfw-diff(Eiy_rfw,x)+diff(Eix_rfw,y)
Bz_rfw	Magnetic flux density, z component	jwBz_rfw/jomega_rfw

scBz_rfw	Scattered magnetic flux density, z component	-scEyxscExy/jomega_rfw
normE_rfw	Electric field, norm	sqrt(abs(Ex)^2+abs(Ey)^2+abs(Ez)^2)
normD_rfw	Electric displacement, norm	sqrt(abs(Dx_rfw)^2+abs(Dy_rfw)^2+abs(Dz_rfw)^2)
normB_rfw	Magnetic flux density, norm	sqrt(abs(Bx_rfw)^2+abs(By_rfw)^2+abs(Bz_rfw)^2)
normH_rfw	Magnetic field, norm	sqrt(abs(Hx)^2+abs(Hy)^2+abs(Hz)^2)
normPoav_rfw	Power flow, time average, norm	sqrt(abs(Poxav_rfw)^2+abs(Poyav_rfw)^2+abs(Pozav_rfw)^2)
normscE_rfw	Scattered electric field, norm	sqrt(abs(scEx)^2+abs(scEy)^2+abs(scEz)^2)
normscD_rfw	Scattered electric displacement, norm	sqrt(abs(scDx_rfw)^2+abs(scDy_rfw)^2+abs(scDz_rfw)^2)
normscB_rfw	Scattered magnetic flux density, norm	sqrt(abs(scBx_rfw)^2+abs(scBy_rfw)^2+abs(scBz_rfw)^2)
normscH_rfw	Scattered magnetic field, norm	sqrt(abs(scHx)^2+abs(scHy)^2+abs(scHz)^2)
Wmav_rfw	Magnetic energy density, time average	0.25 * real(Hx * conj(Bx_rfw)+Hy * conj(By_rfw)+Hz * conj(Bz_rfw))
Weav_rfw	Electric energy density, time average	0.25 * real(Ex * conj(Dx_rfw)+Ey * conj(Dy_rfw)+Ez * conj(Dz_rfw))
Wav_rfw	Total energy density, time average	Wmav_rfw+Weav_rfw
Qav_rfw	Resistive heating, time average	0.5 * real(Jix_rfw * conj(Ex)-j * real(omega_rfw) * Ex * conj(Dx_rfw)+Jiy_rfw * conj(Ey)-j * real(omega_rfw) * Ey * conj(Dy_rfw)+Jiz_rfw * conj(Ez)-j * real(omega_rfw) * Ez * conj(Dz_rfw))
Poxav_rfw	Power flow, time average, x component	0.5 * real(Ey * conj(Hz)-Ez * conj(Hy))
Poyav_rfw	Power flow, time average, y component	0.5 * real(Ez * conj(Hx)-Ex * conj(Hz))
Pozav_rfw	Power flow, time average, z component	0.5 * real(Ex * conj(Hy)-Ey * conj(Hx))

REFERENCES

1. J. B. Pendry, A. J. Holden, D. J. Robbins, W. J. Stewart, "Magnetism from conductors and enhanced nonlinear phenomena," *IEEE Trans. Microwave Theory and Techniques,* 47 (11), pp. 2075-2084, (1999).

2. C. Caloz, Tatsuo Itoh, "Electromagnetic Metamaterials - Transmission Line Theory and Microwave Applications," *Wiley-Interscience,* (2006).

3. N. Engheta, R. W. Ziolkowski, "Metamaterials- physics and engineering explorations," *Wiley-Interscience,* (2006).

4. G. V. Eleftheriades, K. G. Balmain, "Negative-refraction metamaterials-fundamental principles and application," *Wiley-Interscience,* (2006).

5. Sergei Tretyako, "Analytical Modeling in Applied Electromagnetic," *Artech House Publisher,* (2006).

6. T. J. Yen, W. J. Padilla, N. Fang, D. C. Vier, D. R. Smith, J. B. Pendry, D. N. Basov, and X. Zhang, "Terahertz magnetic response from artificial materials," *Science,* 303, pp. 1494-1496, (2004).

7. X-L. Xu, B-G. Quan, C-Z. Gu, L. Wang, "Bianisotropic response of microfabricated metamaterials in the terahertz region," *J. Opt Soc. Am. B,* 23 (6), pp. 1174-1180, (2006).

8. W. J. Padilla, A. J. Taylor, C. Highstrete, M. Lee, R.D. Averitt, "Dynamical electric and magnetic metamaterial response at terahertz frequencies," *Phys. Rev. Lett.,* 96 (10), pp. 1-4, (2006).

9. B. G. Quan, X. L. Xu, H. F. Yang, X. X. Xia, Q. Wang, L. Wang, C.Z. Gu, F. Li, "Time-resolved broadband analysis of split ring resonators in terahertz region," *App. Phys. Lett.,* 89 (4), pp. 0411011-0411014, (2006).

10. J. C. Sturm, F. Pschenitzka, T. R. Hebner, M. H. Lu, S. Troian, "Printing approaches for large-area color organic LED displays," *Proc. of SPIE - The International Society for Optical Engineering,* 3797, p. 266-274, (1999).

11. S.-C. Chang, J. Liu, J. Bharathan, Y. Yang, J. Onohara, J. Kido, "Multicolor organic light-emitting diodes processed by hybrid inkjet printing," *Adv. Materials,* 11 (9), pp. 734-737, (1999).

12. V. G. Veselago, "The electrodynamics of substances with simultaneously negative values of ε and μ," *Sov. Phys. Usp.,* 10, pp. 509-514, (1968).

13. R. A. Shelby, D. R. Smith, S. Schultz, "Experimental verification of a negative index of refraction," *Science,* 292 (5514), pp. 77-79, (2001).

14. J. Han, "Probing negative refractive index of metamaterials by terahertz time domain spectroscopy," *Opt. Exp.,* 16 (2), pp. 1356, (2008).

15. D. Zimdars, J. S. White, G. Stuk, A. Chernovsky, G. Fichter, S. Williamson, "Large area terahertz imaging and non-destructive evaluation applications," *Insight-Non-Destructive Testing and Condition Monitoring,* 48, pp. 537-539, (2006).

16. H. S. Chua, J. Obradovic, A. D. Haigh, P. C. Upadhya, O. Hirsch, D. Crawley, A.A.P. Gibson, E.H. Linfield, "Terahertz time-domain spectroscopy of crushed wheat grain," *IEEE MTT-S International Microwave Symposium,* pp. 4, (2005).

17. M. Reid and, R. Fedosejevs, "Terahertz birefringence and attenuation properties of wood and paper," *Appl. Opt.,* 45, pp. 2766-2772, (2006).

18. C. J. Strachan, T. Rades, D. A. Newnham, K. C. Gordon, M. Pepper, P. F. Taday, "Using terahertz pulsed spectroscopy to study crystallinity of pharmaceutical materials," *Chem. Phys. Lett.,* 390, pp. 20-24, (2004).

19. D. S. Venables, C. A. Schmuttenmaer, "Spectroscopy and dynamics of mixtures of water with acetone, acetonitrile, and methanol," *J. Chem. Phys.,* 113, pp. 11222-11236, (2000).

20. J. F. Federici, B. Schulkin, F. Huang, D. E. Gary, R. B. Barat, F. Oliveira, and D. Zimdars, "THz imaging and sensing for security applications - Explosives, weapons, and drugs," Semicond. *Sci. Technol.,* 20, pp.266-280, (2005).

21. M. V. K. Chari, S. J. Salon, "Numerical Methods in Electromagnetism," *Elsevier Inc,* (2000).

22. R. M. Walser, W. S. Weiglhofer, A. Lakhtakia, "Introduction to complex mediums for electromagnetics and optics," *SPIE Press,* Bellingham, WA, USA, (2003).

23. J. Brown, "Artificial dielectrics," *Progress in Dielectrics,* 2, pp. 195-225, (1960).

24. W. J. Padilla, M. T. Aronsson, C. Highstrete, M. Lee, A.J. Taylor, R. D. Averitt, "Electrically resonant terahertz metamaterials: Theoretical and experimental investigations," *Phys. Rev. B-Condensed Matter and Materials Physics,* 75 (4), pp. 041102-041105, (2007).

25. D. R. Smith, W. J. Padilla, D. C. Vier, S. C. Nemat-Nasser, S. Schultz, "Composite medium with simultaneously negative permeability and permittivity," *Phys. Rev. Lett.,* 84 (18), pp. 4184-4189, (2000).

26. H. O. Moser, B. D. F. Casse, O. Wilhelmi, B. T. Saw, "Terahertz response of a microfabricated rod-split-ring-resonator electromagnetic metamaterials," *Phys. Rev. Lett.,* 94 (6), pp. 1-4, (2005).

27. W. Kock, "Metallic delay lenses," *Bell Syst. Tech. J.,* 27, pp. 58-82, (1948).

28. J. Pendry, A. Holden, D. Robbins, and W. Stewart, "Magnetism from conductors and enhanced nonlinear phenomena," *IEEE Trans. Microwave Theory Techn.,* 47 (11), pp. 195-225, (1999).

29. S. Schelkuno, H. Friis, "Antennas: Theory and Practice," *John Wiley and Sons,* New York, (1952).

30. A. A. Houck, J. B. Brock, I. L. Chuang, "Experimental observations of a left-handed material that obeys Snell's law," *Phys. Rev. Lett.,* 90 (13), pp. 1374011-1374014, (2003).

31. J. Huangfu, L. Ran, H. Chen, X.-M. Zhang, K. Chen, T. M. Grzegorczyk, J.A. Kong, "Experimental confirmation of negative refractive index of a metamaterial composed of Ω-like metallic patterns," *Appl. Phys. Lett.,* 84 (9), pp.1537, (2004).

32. T. J. Yen, W. J. Padilla, N. Fang, D. C. Vier, D. R. Smith, J. B. Pendry, D. N. Basov, X. Zhang, "Terahertz magnetic response from artificial materials," *Science,* 303 (5663), pp. 1494-1496, (2004).

33. A. K. Azad, J. Dai, W. Zhang, "Transmission properties of terahertz pulses through subwavelength double split-ring resonators," *Opt. Lett.,* 31 (5), pp. 634-636, (2006).

34. H.-T. Chen, W. J. Padilla, J. M. O. Zide, A. C. Gossard, A. J. Taylor, R. D. Averitt, "Active terahertz metamaterial devices," *Nature,* 444 (7119), pp. 597-600, (2006).

35. T. F. Gundogdu, I. Tsiapa, A. Kostopoulos, G. Konstantinidis, N. Katsarakis, R. S. Penciu, M. Kafesaki, C. M. Soukoulis, "Experimental demonstration of negative magnetic permeability in the far-infrared frequency regime," *Appl. Phys. Lett.,* 89 (8), pp. 084103, (2006).

36. Z. Jakšić, D. Vasiljević-Radović, M. Maksimović, M. Sarajlić, Z. Djurić, "Nanofabrication of planar split ring resonators for negative refractive index metamaterials in the infrared range," *J. Serbian Chem. Soc.,* 71 (6), pp. 695-703; (2006).

37. S. Linden, C. Enkrich, G. Dolling, M. W. Klein, J. Zhou, T. Koschny, C. M. Soukoulis, M. Wegener, "Photonic metamaterials: Magnetism at optical frequencies," *IEEE- J. Selected Topics in Quantum Electronics,* 12 (6), pp. 1097-1104, (2006).

38. J. D. Jackson. "Classical Electrodynamics," 3rd ed, *Wiley, Inc.,* (1998).

39. D. R. Smith, D. Schurig, W. J. Padilla, "Negative refraction of modulated electromagnetic waves," *Appl. Phys. Lett.,* 81, pp. 2713-2715, (2002).

40. J. Lu, T. M. Grzegorczyk, Y. Zhang, J. Pacheo, B. I. Wu, J. A. Kong, and M. Chen, "Cerenkov radiation in materials with negative permittivity and permeability"; *Optics Exp.,* 11 (7), pp. 723-734, (2003).

41. I. V. Shadrivov, R. W. Ziolkowski, A. A. Zharov, and Y. S. Kivshar, "Excitation of guided waves in layered structures with negative refraction," *Optics Exp.,* 13 (2), pp. 481-492, (2003).

42. A. Grbic, G .V. Eleftheriades, "Overcoming the diffraction limit with a planar left-handed transmission-line lens," *Phys. Rev. Lett.,* 92 (11), pp. 117403, (2004).

43. N. Fang, H. Lee, C. Sun, X. Zhang, "Sub-diffraction-limited optical imaging with a silver superlens," *Science,* 308 (5721), p. 534-537, (2005).

44. A. Alu, N. Engheta, "Achieving transparency with plasmonic and metamaterial coatings," *Phys. Rev. E,* 72, pp. 016623, (2005).

45. U. Leonhardt, "Optical conformal mapping," *Science,* 312, pp. 1777-1780, (2006).

46. J. B. Pendry, D. Schurig, D. R. Smith, "Controlling electromagnetic fields," *Science,* 312, pp. 1780-1782, (2006).

47. X. M. Zhou, G. K. Hu, "Design for electromagnetic wave transparency with metamaterials," *Phys. Rev. E,* 74 (2), p. 026607, (2006).

48. D. Schurig, J. J. Mock, B. J. Justice, S. A. Cummer, J. B. Pendry, A. F. Starr, D. R. Smith, "Metamaterial electromagnetic cloak at microwave frequencies," *Science Exp.,* 314, pp. 977-980, (2006).

49. W. Cai, U. K. Chettiar, A. V. Kildishev, V. M. Shalaev, "Optical cloaking with metamaterials," *Nature Photonics,* 1 (4), pp. 224-227, (2007).

50. S. A. Cummer, B. I. Popa, D. Schurig, D. R. Smith, "Full-wave simulations of electromagnetic cloaking structures," *Phys. Rev. E,* 74 (3), pp. 036621, (2006).

51. G. W. Milton and N.-A. P. Nicorovici, "On the cloaking effects associated with anomalous localized resonance," *Proc. of the Royal Society A,* 462 (2074), pp. 3027-3059, (2006).

52. B. Temelkuran, E. Ozbay, "Experimental demonstration of photonic crystal based waveguides," *Appl. Phys. Lett.,* 74 (4), pp. 486-488, (1999).

53. P. de Maagt, "BG components and applications at microwave and (sub) millimeter waves," *European Microwave Week Workshop, EuMC05,* Amsterdam, (2004).

54. Y. Horii, C. Caloz, and T. Itoh, "Super-compact multilayered left-handed transmission line and diplexer application," *IEEE Trans. Microw. Theory Techn.,* 53 (4), pp. 1527-1533, (2005).

55. M. Bayindir, B. Temelkuran, E. Ozbay, "Propagation of photons by hopping: A waveguiding mechanism through localized coupled cavities in three-dimensional photonic crystals," *Phys. Rev. B,* 61 (18), pp. 11855-11858, (2000).

56. A. K. Iyer and G. Eleftheriades, "Negative refractive index transmission line metamaterials and applications," *Proceedings of the Workshop on Metamaterials for Microwave and Optical Technologies,* p. 52, San Sebastian, Spain, (2005).

57. A. Lai, C. Caloz, and T. Itoh, "Composite left-/right-handed transmission line metamaterials," *IEEE Magazine,* p.14, (2004).

58. I. S. Nefedov, S. A. Tretyakov, J. Säily, Xu Liangge, T. Mynttinen, and M. Kaunisto, "Application of wire media layers for coupling reduction in antenna arrays and microwave devices," *Loughborough Antennas and Propagation Conference,* pp. 39-44, Loughborough, UK, (2007).

59. C. Caloz, T. Itoh, "Array factor approach of leaky-wave antennas and application to 1-D/2-D composite right/left-handed (CRLH) structures," *IEEE Microw. Wireless Compon. Lett.,* 14, p. 274, (2004).

60. C. Caloz, "Novel metamaterial antennas and reflectors," *Proceedings of the Workshop on Metamaterials for Microwave and Optical Technologies,* p. 41, San Sebastian, Spain, (2005).

61. J. Sun, W. Sun, T. Jiang, and Y. Feng, "Directive electromagnetic radiation of a line source scattered by a conducting cylinder coated with left-handed metamaterial," *Microw. and Opt. Technol. Lett.,* 47, p. 274, (2005).

62. M. Born, E. Wolf, "Principle of Optics," 7th ed, *Cambridge University Press,* (1999).

63. C. F. Coombs, "Printed Circuits Handbook," 6th ed, *McGraw-Hill,* (2007).

64. Thick film technology, Retrieved July 31, 2008 from the World Wide Web: http://en.wikipedia.org/wiki/Thick_film_technology

65. C. Mack, "Semiconductor Lithography - The Basic Process," Retrieved July 22, 2008 from the World Wide Web: http://www.lithoguru.com/scientist/lithobasics.html

66. B. Quan, X. Xu, X. Xia, H. Yang, L. W, Z. Cui, C. Gu, "Microfabrication and properties of the meta-materials," *Microelectronic Engineering,* 83, pp. 1364-1366, (2006).

67. G. L.-T. Chiu, J. M. Shaw, "Optical lithography: Introduction," Retrieved June 2, 2008 from the World Wide Web: http://www.research.ibm.com/journal/rd/411/chiu.html

68. W. Wong, "Inkjet printer draws the line in manufacturing technology," *Electronic Design,* 53 (25), pp. 25, (2005).

69. J. Chung, S. Ko, C. P. Grigoropoulos, N.R. Bieri, C. Dockendorf, D. Poulikakos, "Damage-free low temperature pulsed laser printing of gold nanoinks on polymers," *Journal of Heat Transfer,* 127 (7), pp. 724-732, (2005).

70. I. Koltover, "Material Matter- Chemistry Driving Performance," *Sigma- Aldrich handbook,* 2 (3), (2007).

71. S. Kirchmeyer, K. Reuter, "Scientific importance, properties and growing applications of poly(3,4-ethylenedioxythiophene)," *J. Mater. Chem.,* 15, pp. 2077-2088, (2005).

72. L. B. Groenendaal, F. Jonas, D. Freitag, H. Pielartzik, J. R. Reynolds, "Poly(3,4-ethylenedioxythiophene) and its derivatives: past, present, and future," *Adv. Materials,* 12 (7), pp. 481, (2000).

73. L. Groenendaal, G. Zotti, F. Jonas, "Optical, conductive and magnetic properties of electrochemically prepared alkylated poly(3,4-ethylenedioxythiophene)," *Synthetic Metals,* 118, p. 105, (2001).

74. T. P. Nyuyen, P. Le Rendu, P. D. Long, S. A. De Vos, "Chemical and thermal treatment of PEDOT:PSS thin films for use in organic light emitting diodes," *Surface and Coatings Technology,* 180-181, pp. 646-649, (2004).

75. H. Yan, T. Kagata, Y. Mori, Y. Harashina, Y. Hara, H. Okuzaki, "Micrometer-scaled channel lengths of organic field-effect transistors patterned by using PEDOT/PSS microfibers," *Chemistry Lett.,* 37 (1), pp. 44-45, (2008).

76. R. Bayon, R. Musembi, A. Belaidi, M. Bar, T. Guminskaya, M.-Ch. Lux-Steiner, Th. Dittrich, "Highly structured TiO2/In(OH)xSy/PbS/ PEDOT:PSS for photovoltaic applications," *Solar Energy Materials and Solar Cells,* 89 (1), pp. 13-25, (2005).

77. U. Lang, P. Rust, J. Dual, "Towards fully polymeric MEMS: Fabrication and testing of PEDOT/PSS strain gauges," *Microelectronic Engineering,*,85 (5-6), pp. 1050-1053, (2008).

78. F. Vitale, L. Mirenghi, E. Piscopiello, G. Pellegrini, E. Trave, G. Mattei, I. Fratoddi, M.V. Russo, L. Tapfer, P. Mazzoldi, "Gold nanoclusters-organometallic polymer nanocomposites: Synthesis and characterization," *Materials Science and Engineering C,* 27 (5-8), pp.1300-1304, (2007).

79. D. Shaloma, R. C. R. Wootton, R. F. Winklea, B. F. Cottama, R. Vilara, A. J. de Melloa, C. P. Wilde, "Synthesis of thiol functionalized gold nanoparticles using a continuous flow microfluidic reactor," *Materials Lett.,* 61 (4-5), pp. 1146-1150, (2007).

80. "Nanogold conducting inks," NanoMas Technologies, Inc, Vestal, NY.

81. W. Letendre, A. Brady, "Advances in piezoelectric Ink Jet Micropumps for precision deposition," *International Conference on Digital Printing Technologies*, pp. 859-862, (2004).

82. W. Letendre, "Challenges in jetting OLED fluidic in the manufacturing of FPD using piezoelectric micro-pumps," Spectra, Inc., Tech. Rep., Lebanon, NH, USA.

83. J. Chung, S. Ko, C. P. Grigoropoulos, N. R. Bieri, C. Dockendorf, D. Poulikakos, "Damage-free low temperature pulsed laser printing of gold nanoinks on polymers," *Transactions of the ASME.,* 127, pp. 724-731,(2005).

84. Y. L. Hor, H. C. Lim, J. F. Federici, E. Moore, J. W. Bozzelli, "Terahertz study of trichloroanisole by time-domain spectroscopy," *Chem. Phys.,* 353 (1-3), pp. 185-188, (2008).

85. Y. L. Hor, J. F. Federici, R. L. Wample, "Non-destructive evaluation of cork enclosures using terahertz/ millimeter wave spectroscopy and imaging," *Appl. Optics,* 47(1), pp. 72-78, (2008).

86. J. T. Kindt, C. A. Schmuttenmaer, "Far-infrared dielectric properties of polar liquids probed by femtosecond terahertz pulse spectroscopy," *J. of Phys. Chem.,* 100 (24), pp. 10373-10379, (1996).

87. D. M. Mittleman, R. H. Jacobsen, R. Neelamani, R. G. Baraniuk, M. C. Nuss, "Gas sensing using terahertz time-domain spectroscopy," *Appl. Phys. B,* 67 (3), pp. 379-390, (1998).

88. D. H. Auston, K. P. Cheung, P. R. Smith, "Picosecond photoconducting Hertzian dipoles," *Appl. Phys. Lett.,* 45 (3), pp. 284-286, (1984).

89. Ch. Fattinger, D. Grischkowsky, "Point source terahertz optics," *Appl. Phys. Lett.,* 53 (16), pp. 1480-1482, (1988).

90. M. van Exter, Ch. Fattinger, D. Grischkowsky, "Terahertz time-domain spectroscopy of water vapor," *Optics Lett.,* 14 (20), pp. 1128-1130, (1989).

91. N. Katsarakis, T. Koschny, E. N. Economou, C. M. Soukoulis, and M. Kafesaki, "Electric coupling to the magnetic resonance of split ring resonators," *Appl. Phys. Lett.,* 84, p. 2943, (2004).

92. R. Marqués, J. D. Baena, M. Beruete, F. Falcone, T. Lopetegi, M. Sorolla, F. Martín, J. Garcia, "Ab initio analysis of frequency selective surfaces based on conventional and complementary split ring resonators," *J. Opt. A,* 7 (2), pp. 38-43, (2005).

93. C-Y. Chen, S-C. Wu, T-J. Yen, "Experimental verification of standing-wave plasmonic resonances in split-ring resonators," *Appl. Phys. Lett.,* 93 (3), p. 034110, (2008).

94. C. M. Soukoulis, M. Kafesaki, E. N. Economou, "Negative index materials: New frontiers in optics," *Adv. Materials,* 18 (15), pp. 1941-1952, (2006).

95. P. Ikonen, E. Saenz, R. Gonzalo, C. Simovski, S. Tretyakov, "Mesoscopic effective material parameters for thin layers modeled as single and double grids of interacting loaded wires," *Metamaterials,* 1 (2), pp. 89-105, (2007).

96. D. P. Starinshak, N. D. Smith, J. D. Wilson, "Using COMSOL multiphysics software to model anisotropic dielectric and metamaterial effects in folded-waveguide traveling-wave tube slow-wave circuits," *IEEE International Vacuum Electron Sources Conference, IVESC,* pp. 162-163, (2008).

97. F. Gadot, B. Belier, A. Aassime, J. Mangeney, A. De Lustrac, J.-M. Lourtioz, "Infrared response of a metamaterial made of gold wires and split ring resonators deposited on silicon," *Optical and Quantum Electronics,* 39 (4-6), pp. 273-284, (2007).

98. J. Li, A. Wood, "Finite element analysis for wave propagation in double negative metamaterials," *J. Sci. Comp.,* 32 (2), pp. 263-286, (2007).

99. O. Ozgun, M. Kuzuoglu, "Efficient finite element solution of low-frequency scattering problem via anisotropic metamaterial layers," *Microwave and Opts. Techn. Lett.,* 50 (3), pp. 639-646, (2008).

100. G. Cevini, M. Raffetto, "Performance evaluation of 3D FEM-based simulators in modeling scattering problems with metamaterials," *35th European Microwave Conference - Conference Proceedings 2,* pp. 857-860, (2005).

101. T. Mustonen, K. Kordás, S. Saukko, G. Tóth, J. S. Penttilä, P. Helistö, H. Seppä, H. Jantunen, "Inkjet printing of transparent and conductive patterns of single-walled carbon nanotubes and PEDOT-PSS composites," *Phys. Stat. Sol. B,* 244 (11), pp. 4336-4340 (2007).

102. J. Lu, N. J. Pinto, A. G. MacDiarmid, "Apparent dependence of conductivity of a conducting polymer on an electric field in a field effect transistor configuration," *J. Appl. Phys.*, 92 (10), (2002).

103. J. F. Federici, B. I. Greene, D. R. Dykaar, F. Sharifi, and R. C. Dynes, "Direct picosecond measurement of photoinduced cooper pair breaking in lead," *Phys. Rev. B,* 46, p. 11153, (1992).